



AFRL-AFOSR-UK-TR-2019-0050

Corrosion Resistance of High-Temperature SMAs Under Extreme Environments

Nikolaos Michailidis
ARISTOTLE UNIVERSITY OF THESSALONIKI
UNIVERSITY CAMPUS, ADMINISTRATION BUILDING
THESSALONIKI, 54124
GR

09/12/2019
Final Report

DISTRIBUTION A: Distribution approved for public release.

Air Force Research Laboratory
Air Force Office of Scientific Research
European Office of Aerospace Research and Development
Unit 4515 Box 14, APO AE 09421

REPORT DOCUMENTATION PAGE				<i>Form Approved OMB No. 0704-0188</i>	
<p>The public reporting burden for this collection of information is estimated to average 1 hour per response, including the time for reviewing instructions, searching existing data sources, gathering and maintaining the data needed, and completing and reviewing the collection of information. Send comments regarding this burden estimate or any other aspect of this collection of information, including suggestions for reducing the burden, to Department of Defense, Executive Services, Directorate (0704-0188). Respondents should be aware that notwithstanding any other provision of law, no person shall be subject to any penalty for failing to comply with a collection of information if it does not display a currently valid OMB control number.</p> <p>PLEASE DO NOT RETURN YOUR FORM TO THE ABOVE ORGANIZATION.</p>					
1. REPORT DATE (DD-MM-YYYY) 12-09-2019		2. REPORT TYPE Final		3. DATES COVERED (From - To) 01 Jan 2017 to 31 Dec 2018	
4. TITLE AND SUBTITLE Corrosion Resistance of High-Temperature SMAs Under Extreme Environments				5a. CONTRACT NUMBER	
				5b. GRANT NUMBER FA9550-17-1-0059	
				5c. PROGRAM ELEMENT NUMBER 61102F	
6. AUTHOR(S) Nikolaos Michailidis				5d. PROJECT NUMBER	
				5e. TASK NUMBER	
				5f. WORK UNIT NUMBER	
7. PERFORMING ORGANIZATION NAME(S) AND ADDRESS(ES) ARISTOTLE UNIVERSITY OF THESSALONIKI UNIVERSITY CAMPUS, ADMINISTRATION BUILDING THESSALONIKI, 54124 GR				8. PERFORMING ORGANIZATION REPORT NUMBER	
9. SPONSORING/MONITORING AGENCY NAME(S) AND ADDRESS(ES) EOARD Unit 4515 APO AE 09421-4515				10. SPONSOR/MONITOR'S ACRONYM(S) AFRL/AFOSR IOE	
				11. SPONSOR/MONITOR'S REPORT NUMBER(S) AFRL-AFOSR-UK-TR-2019-0050	
12. DISTRIBUTION/AVAILABILITY STATEMENT A DISTRIBUTION UNLIMITED: PB Public Release					
13. SUPPLEMENTARY NOTES					
14. ABSTRACT The study of shape memory alloys has yield to the fabrication of a new generation of more functional, simple, costeffective and reliable actuators. Every alloy has different properties, such as transformation temperatures, hysteresis characteristics etc., and as most of the alloys, properties can be significantly changed with heat treatment leading to hardening through precipitation of nanoparticles and change in transformation temperatures. To consolidate the use of new materials in an application it is necessary to certify their life span in the working environment and mechanical conditions. Assuming that the most common cause of a component failure during operation is fatigue, the main goal of this research program was to draw valuable conclusions for the resistance to fatigue by combined thermomechanical cyclic loading in a neutral environment of Ni-rich NiTi(Hf) High Temperature Shape Memory Alloys (HTSMAs), as well as for the assessment of the effect of electrochemical degradation on the structural and functional properties due to combined mechanical cyclic loading and corrosion. The specimens were first heat treated by heating at 550C for 3 hours in order to increase their hardness and maintain high values of the phase transformation temperatures and stability.					
15. SUBJECT TERMS EOARD, Materials, High Temperature SMA, Corrosion Resistance					
16. SECURITY CLASSIFICATION OF:			17. LIMITATION OF ABSTRACT SAR	18. NUMBER OF PAGES	19a. NAME OF RESPONSIBLE PERSON GARNER, DAVID
a. REPORT Unclassified	b. ABSTRACT Unclassified	c. THIS PAGE Unclassified			19b. TELEPHONE NUMBER (Include area code) 011-44-1895-616021



**Physical Metallurgy Laboratory
School of Mechanical Engineering
Faculty of Engineering, Building D', 9th floor
Aristotle University of Thessaloniki (PO Box: 490)
GR 54124 Thessaloniki, Greece
Tel. +30 2310 995891, Fax. +30 2310 996069
Director: Prof. Dr.-Eng. Nikolaos Michailidis**



Final Report

Corrosion resistance of High-Temperature Shape Memory Alloys (HTSMAs) under extreme environments

(Award No. FA9550-17-1-0059)

Main research team:

Apostolos Arvanitidis, MSc

Alexios Paschou, Dipl.-Eng.

Prof. Nikolaos Michailidis

March 2019, Thessaloniki, Greece

Table of contents

1. Introduction.....	4
2. Development of The experimental set-up	4
3. RESULTS & Discussion	9
3.1 Analytical stress and modulus of elasticity calculations	9
3.2 C-ring compression experiments for the extraction of Stress vs. Displacement and Modulus of elasticity vs. Displacement diagrams	10
3.3 Changing of the modulus of elasticity by thermomechanical fatigue.....	16
4. Transformation temperatures.....	18
4.1 Transformation temperatures with constant displacement.....	18
4.2 Transformation temperatures with isobaric tension tests	26
4.3 Transformation temperatures obtained by differential scanning calorimetry (DSC)	28
5. Microstructural characterization	29
5.1 Scanning electron microscopy (SEM)	29
6. Fatigue experiments.....	31
6.1 Fractographic analysis (for specimen with fatigue at martensitic phase)	32
6.1.1 Stereo microscopy.....	32
6.1.2 Scanning electron microscopy.....	35
6.1.3 Optical microscopy	36
6.2 Fractographic analysis (specimen with fatigue at austenitic phase).....	36
6.2.1 Stereo microscopy.....	36
6.2.2 Scanning electron microscopy.....	40
6.2.3 Optical microscopy	41
6.3 Failure mechanism	41
7. Combined corrosion and fatigue experiments.....	42
7.1 1 st combined corrosion and fatigue experiment without electrochemical measurements	42
7.2 Fractographic analysis on the sample of the 1 st combined corrosion and fatigue experiment.....	43
7.3 Study of the corrosion mechanism of an electrochemically cleaned specimen.	46
7.3.1 In-situ detection of open circuit potential, Potentiodynamic polarization, Electrochemical impedance spectroscopy.....	46
7.4 2 nd experiment of combined corrosion and fatigue test of the electrochemically cleaned specimen	50
7.5 Study of the corrosion mechanism on the electrochemically uncleaned specimen.....	52
7.6 3 rd experiment of combined corrosion and fatigue test without electrochemical cleaning.....	56

7.7	Fractographic analysis on 2 nd combined corrosion and fatigue experiment	56
7.8	Fractographic analysis on 3 rd combined corrosion and fatigue experiment on uncleaned specimen 61	
8.	SUMMARY	65
9.	REFERENCES	67
10.	Publicity activities.....	68
10.1	Journal publications	68
10.2	Presentations in International Conferences.....	68
11.	List of figures & diagrams.....	70

1. INTRODUCTION

The study of shape memory alloys has yielded to the fabrication of a new generation of more functional, simple, cost-effective and reliable actuators. Every alloy depending on its composition has different properties, such as transformation temperatures, hysteresis characteristics etc., and as most of the alloys, properties can be significantly changed with heat treatment leading to hardening through precipitation of nanoparticles and change in transformation temperatures [1][6][10]. To consolidate the use of new materials in an application it is necessary to certify their life span in the working environment and mechanical conditions [2]. Assuming that the most common cause of a component failure during operation is fatigue, the main goal of this research program was to draw valuable conclusions for the resistance to fatigue by *combined thermomechanical cyclic loading* in a neutral environment of Ni-rich NiTi(Hf) High Temperature Shape Memory Alloys (HTSMAs), as well as *for the assessment of the effect of electrochemical degradation on the structural and functional properties due to combined mechanical cyclic loading and corrosion*. The specimens were first heat-treated by heating at 550 °C for 3 hours in order to increase their hardness and maintain high values of the phase transformation temperatures and stability [6][10].

2. DEVELOPMENT OF THE EXPERIMENTAL SET-UP

The initial experimental set-up developed for testing the corrosion-fatigue performance of materials is presented in the 3D sketch of Figure 1 [3].

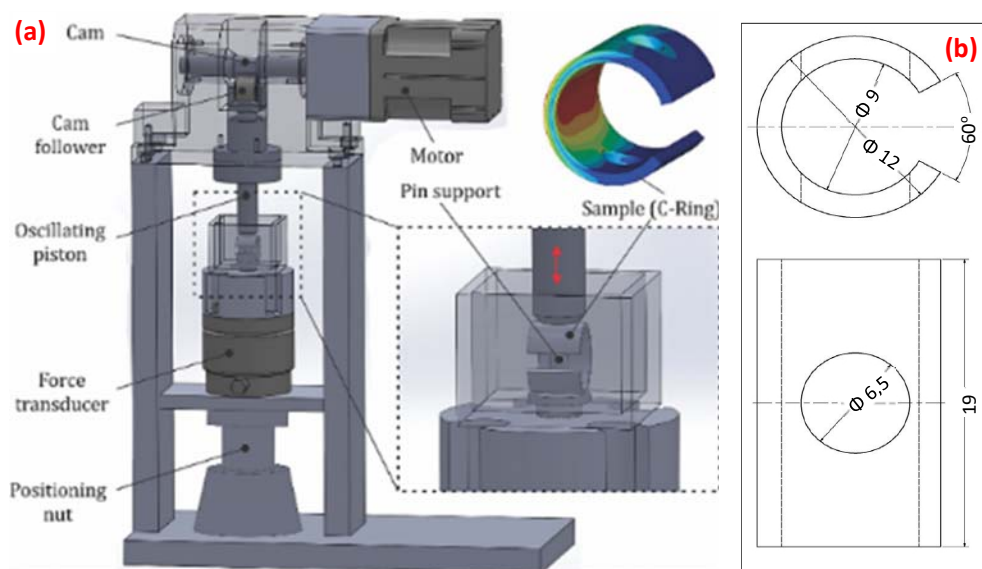


Figure 1: (a) Experimental set-up for testing corrosion-fatigue, employing C-ring samples [3], (b) sample dimensions.

Figures 2 and 4 present the new version of the experimental set-up developed for the needs of the project. It consists of a stiff frame, a force transducer, a cam-driven piston, a cam machined on a shaft and a servomotor attached at the upper part of the device, rotating the shaft through a gear unit. The servomotor rotating speed is controlled by a control unit software package. The oscillation frequency was regulated at 40Hz for all the tested samples. A custom-made software has been developed to control and monitor the temperature and the applied force signal (see Figure 3), assisting to track the exact time of the specimen's failure.

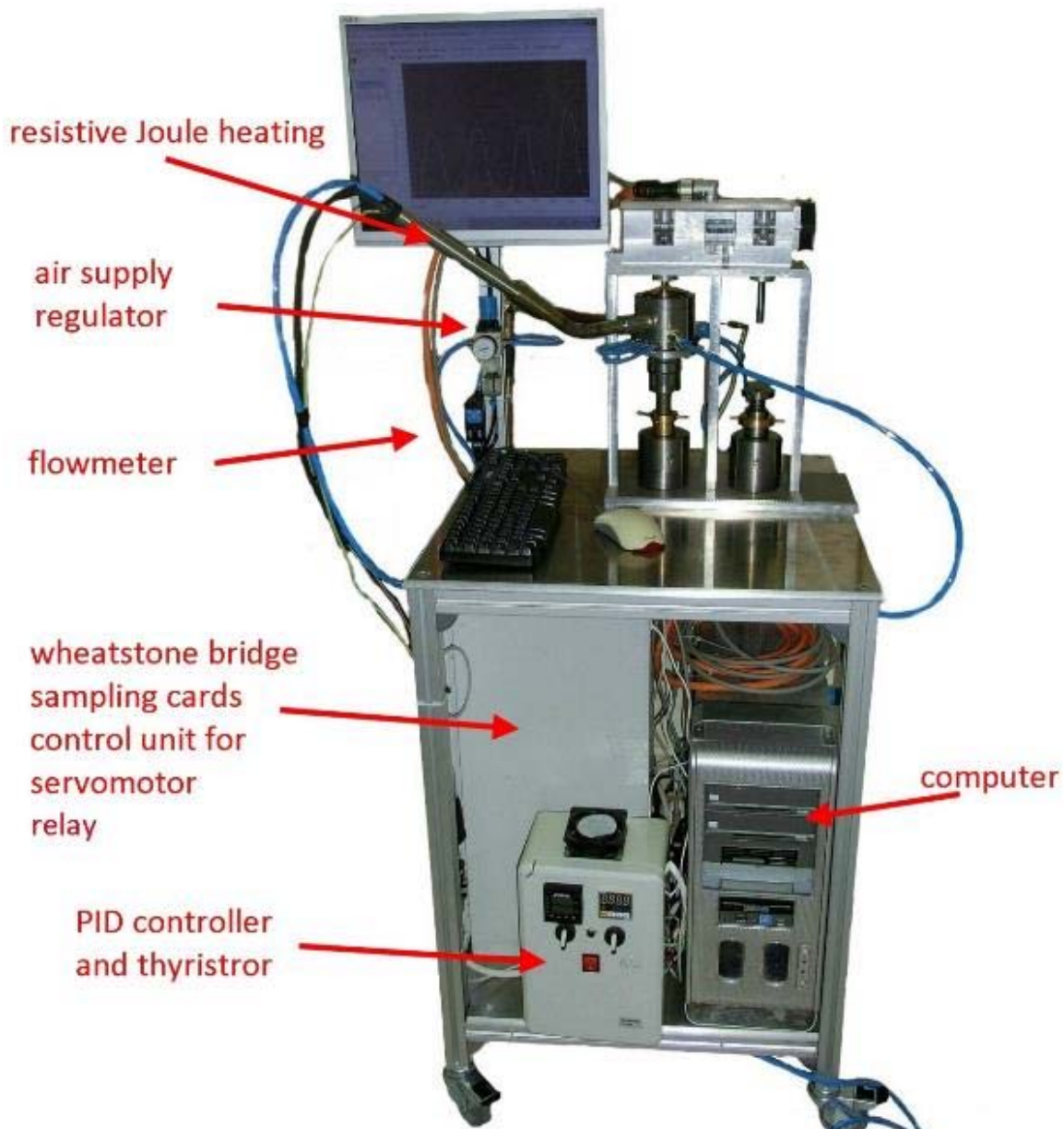


Figure 2: Experimental set-up developed for thermomechanical corrosion fatigue testing, employing C-ring samples.

The signal from the force transducer is reinforced by a Wheatstone bridge and then guided to a sampling card for reading and storing it, employing the application running on the computer. The signal from the temperature sensor is driven to a separate sampling card that reads the temperature and then processing and storing are handled by the same application on the computer.

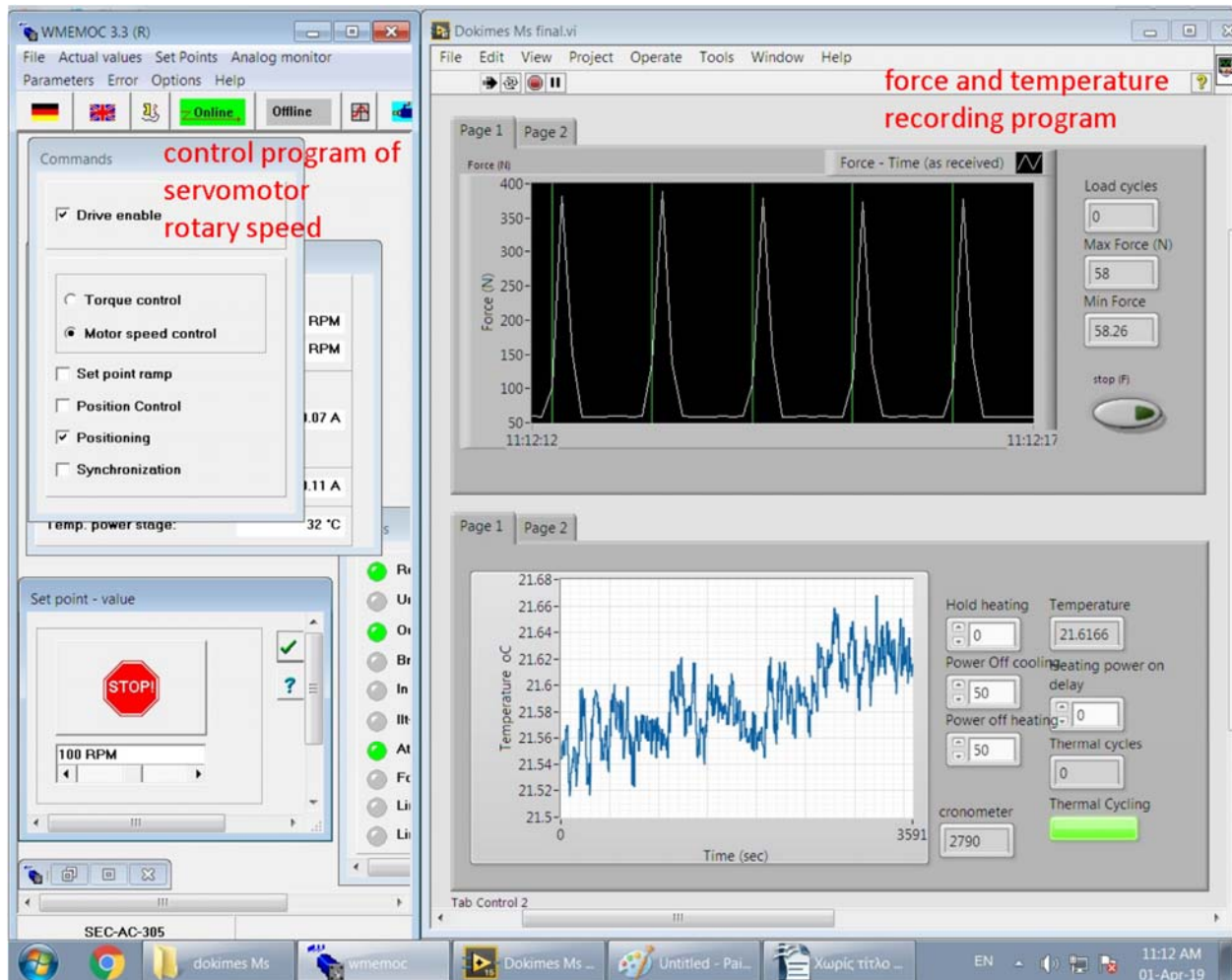


Figure 3: Software packages for guiding the experimental set-up.

The cooling system consists of water and air flow pipes. The tested C-ring specimen is placed into a stainless steel container which is necessary for heating it by using hot air and cooling it using water or cold air. At the base of the container flow channels have been formed for the flow of water that protects the force transducer from overheating, to avoid any influence on the measured forces. The heating rate and the temperature limit values of heating and cooling inside the container are controllable through the software developed and the corresponding hardware (solenoid, a relay and the outputs of the sampling card). The temperature was set through a heating module that was incorporated by using resistive Joule heating of air (or other gas). Exact temperature control is



achieved by using a PID controller and a thyristor. The flow of the heating air is continuously measured with a flowmeter. In order to control the applied loading force in the specimens, two different methods have been developed that offer different loading modes. The first method uses a robust base in which a drive bolt is mounted which can be driven to the desired position with a positioning nut designed to raise the container and compress the sample between the force sensor and the piston. Once the desired test force is attained, the bolt is locked by a retainer. This option offers a displacement-constrained loading of the sample (see Figures 2 and 5). The second method employs a pneumatic piston at the base of the frame to raise the container and the force is controlled by adjusting the air pressure within a 50-liter inert vessel (see Figures 4 and 5). This method is suitable for performing isobaric thermal (actuation) fatigue tests at a constant force.



Figure 4: Experimental set-up for thermal fatigue tests at constant force through a pneumatic piston.

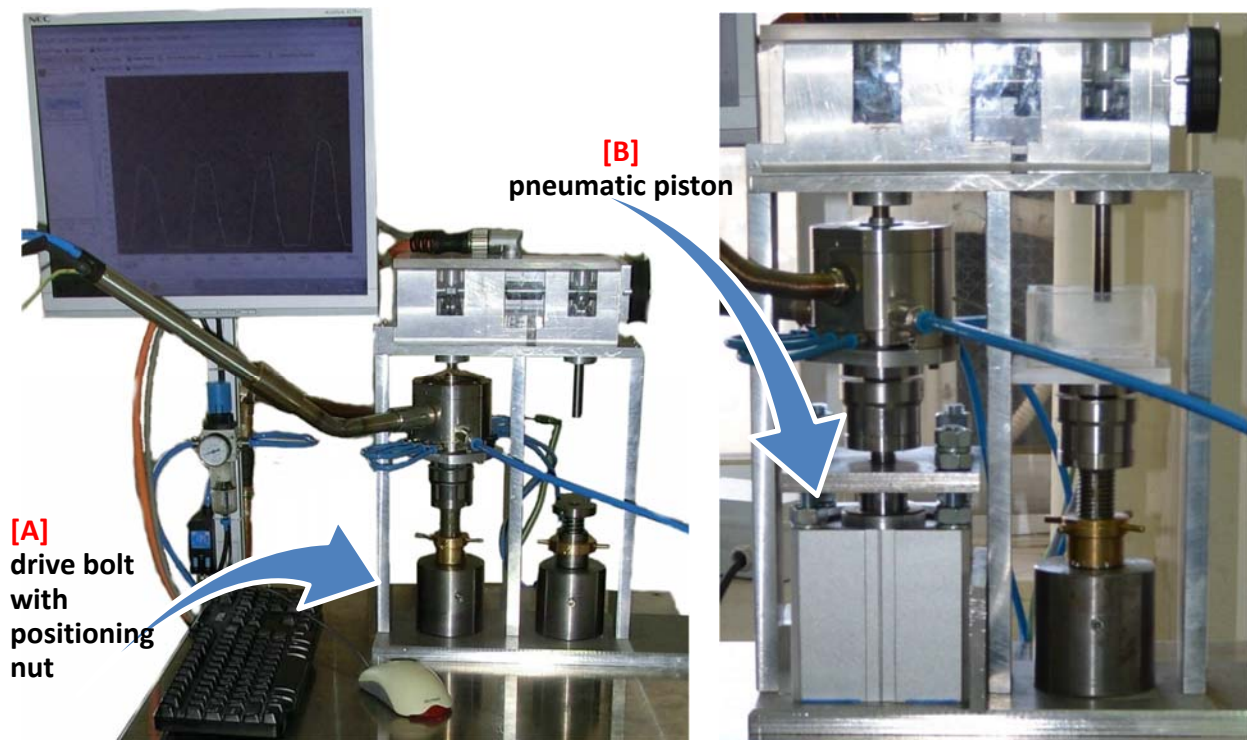


Figure 5: Different control methods of the applied force. The first method in picture [A] uses a drive bolt with a positioning nut. The second method in picture [b] uses a pneumatic piston.

The overall specifications of the developed experimental set-up can be summarized as follows:

- **Mechanical system**
 - **Load range: 0 – 2 kN**
 - **Frequency: 0 – 600 Hz**
- **Heating system**
 - **Temperature range: 25 – 600°C**
 - **Frequency: 0.01 – 0.2 Hz**

The C-ring specimens were manufactured to the C-ring shape according to the ASTM G38-01 standard by wire-electrical discharge machining (W-EDM). This shape of samples has been selected due to their simplicity, relatively low cost, ability to simulate various numbers of variables and to determine useful fatigue data of the alloy which can be then extrapolated to real structures. Another characteristic in the C-ring is the presence of biaxial stresses; that is, transverse as well as circumferential stresses are developed on the critical test section. The stress of principal interest in the C-ring specimen is the circumferential stress. There is a gradient through the thickness, varying from a maximum tension on one surface to a maximum compression on the opposite surface. The

transverse stress varies from a maximum at the mid-width to zero at the edges. In this way there is potential to investigate combined tension and compression stresses developing in the sample, allowing for further assessing the effect of the stress nature on the passive film breakage. The dimensions of the samples as shown in the Figure 1b are: $D_{\text{internal}}=9\text{ mm}$, $D_{\text{external}}=12\text{ mm}$ and $\text{Width}=19\text{ mm}$. Before carrying out each experiment the samples were subjected to heat treatment at 550°C for 3 hours, to attain the desired nano-precipitation for stabilizing the mechanical response of the SMA and tailoring the transformation temperatures.

3. RESULTS & DISCUSSION

Prior to corrosion fatigue testing, a full characterization of the HTSMAs was performed to establish crucial properties and estimate critical stress and strain limits.

For the calculation of the developed stresses by the applied loading, an analytical calculation was performed for the given geometry of the sample. The knowledge of the stress vs. displacement and the geometric constants, a detailed calculation of the modulus of elasticity was also rendered possible.

3.1 Analytical stress and modulus of elasticity calculations

When the force (P) is exerted on the c-ring perpendicular to its axis of symmetry and parallel to the axis of the support bore, there will be a radial (σ_{rp}), a tangential ($\sigma_{\theta p}$) and a shear ($\tau_{r\theta p}$) stress developing (see Figure 6) [4].

The radial, tangential and transitive stresses result from the equations:

$$\sigma_{rp} = -\frac{P}{t \cdot N} * \left(r + \frac{r_i^2 * r_o^2}{r^3} - \frac{r_i^2 + r_o^2}{r} \right) * \sin\theta$$

$$\sigma_{\theta p} = -\frac{P}{t \cdot N} * \left(3r - \frac{r_i^2 * r_o^2}{r^3} - \frac{r_i^2 + r_o^2}{r} \right) * \sin\theta$$

$$\tau_{r\theta p} = \frac{P}{t \cdot N} * \left(r + \frac{r_i^2 * r_o^2}{r^3} - \frac{r_i^2 + r_o^2}{r} \right) * \cos\theta$$

Where:

P: the applied force

t: the width of the c-ring

r_i : the inner radius of the c-ring

r_o : the outer radius of the c-ring

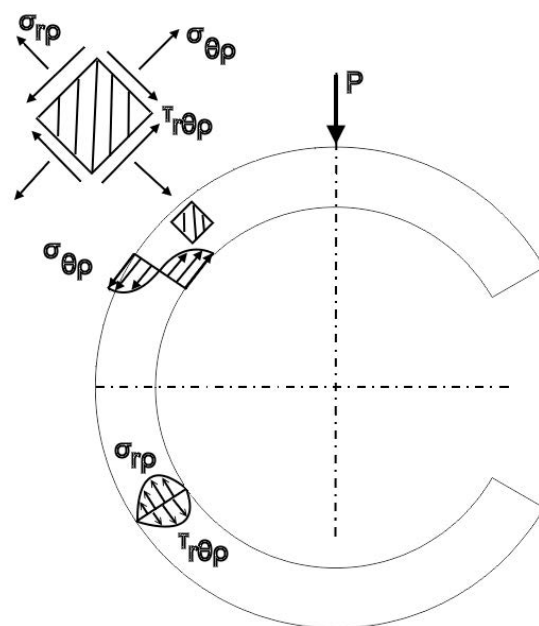


Figure 6 Stress analysis on the c-ring.



r : the radius under consideration

The modulus of elasticity was calculated based on the equation

$$u_c = \frac{\left\{ -(1 + \mu) * \frac{C_1}{r} \right\} + \{ C_2 * ((1 - \mu) * \ln r - 1) * r \} + (1 + \mu) * C_3 * r}{E}$$

Where u_c is the half of the measured displacement at the point of application of the force and its direction and r_{nP} the radius of the neutral axis.

$$C_1 = \frac{4 * P * r_{np} * \sin \theta * r_i^2 * r_o^2 * \ln \frac{r_o}{r_i}}{t * D_o} \quad C_2 = \frac{4 * P * r_{np} * \sin \theta * (r_o^2 - r_i^2)}{t * D_o}$$

$$C_3 = \frac{4 * P * r_{np} * \sin \theta * (r_i^2 \ln r_i - r_o^2 \ln r_o)}{t * D_o}$$

$$D_o = 4 * r_i^2 * r_o^2 * \left(\ln \frac{r_o}{r_i} \right)^2 - (r_o^2 - r_i^2)^2$$

$$r_{nP} = \left\{ \left\{ (r_i^2 + r_o^2) + ((r_i^2 + r_o^2)^2 + 12 r_i^2 * r_o^2)^{0.5} \right\} / 6 \right\}^{0.5}$$

The calculation of the modulus of elasticity (E) can be simplified by applying the equation: **stress = $4 E \tau Z \Delta / \pi D^2$** , according to ASTM G38-01 [5].

Where:

τ : the wall thickness of the c-ring

$$\Delta = 2u_c ,$$

D : the average diameter ($2 r_o - \tau$),

Z : correction factor proportional to D/τ

The deviation of the outcome of the two methods is in the range of 0.3%.

3.2 C-ring compression experiments for the extraction of Stress vs. Displacement and Modulus of elasticity vs. Displacement diagrams

To determine fatigue conditions and to facilitate the analysis of the behavior of the c-ring type specimen, initially compression experiments of the C-ring samples were performed in martensitic phase at 25°C, by successively increasing the force from 150 to 600 N. The loading and unloading curves were extracted in relation to the displacement of the compression piston. The c-ring was



mounted on a stainless steel base (sampler) with a guide pin inserted through its holes to maintain a constant position of the samples throughout the experiment. Figure 7 shows the experimental setup employing an Instron tension-compression device. An overview of the experimental testing performed is shown in Diagrams 1, 2 and 3 in the form of load-displacement.



Figure 7: Setup for testing the compression behavior of the c-rings.

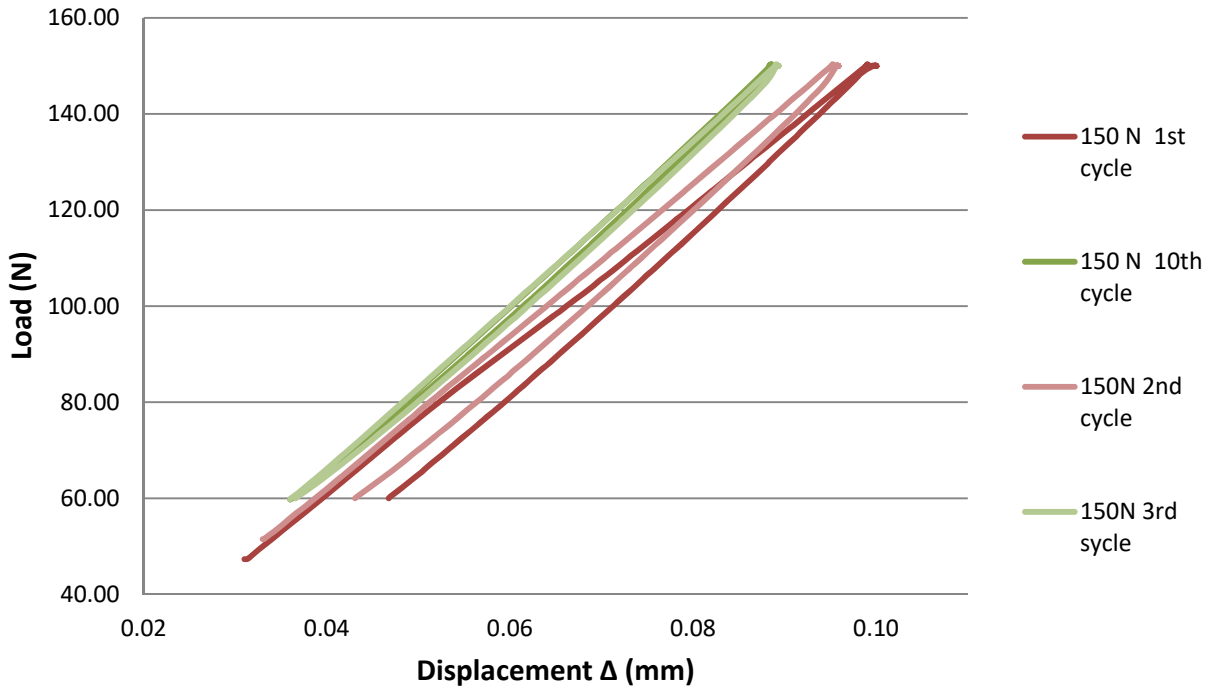


Diagram 1: Load - displacement curves in compression of sma c-ring at 150 N.

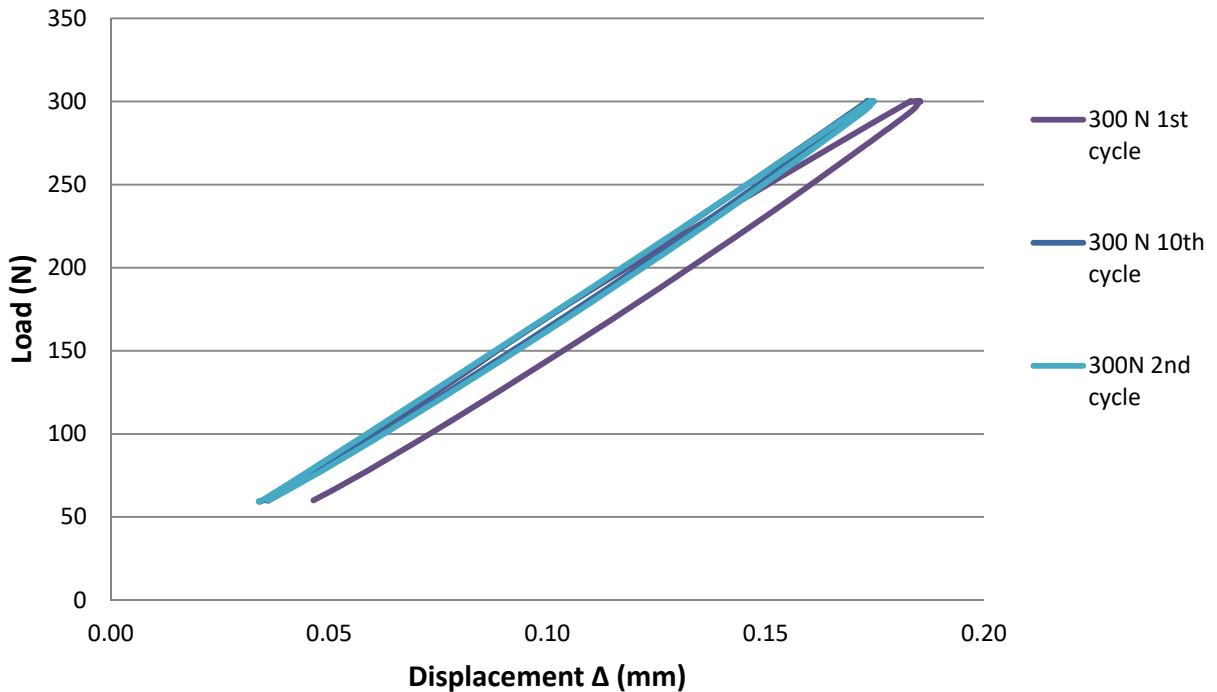


Diagram 2: Load - displacement curves in compression of sma c-ring at 300 N.

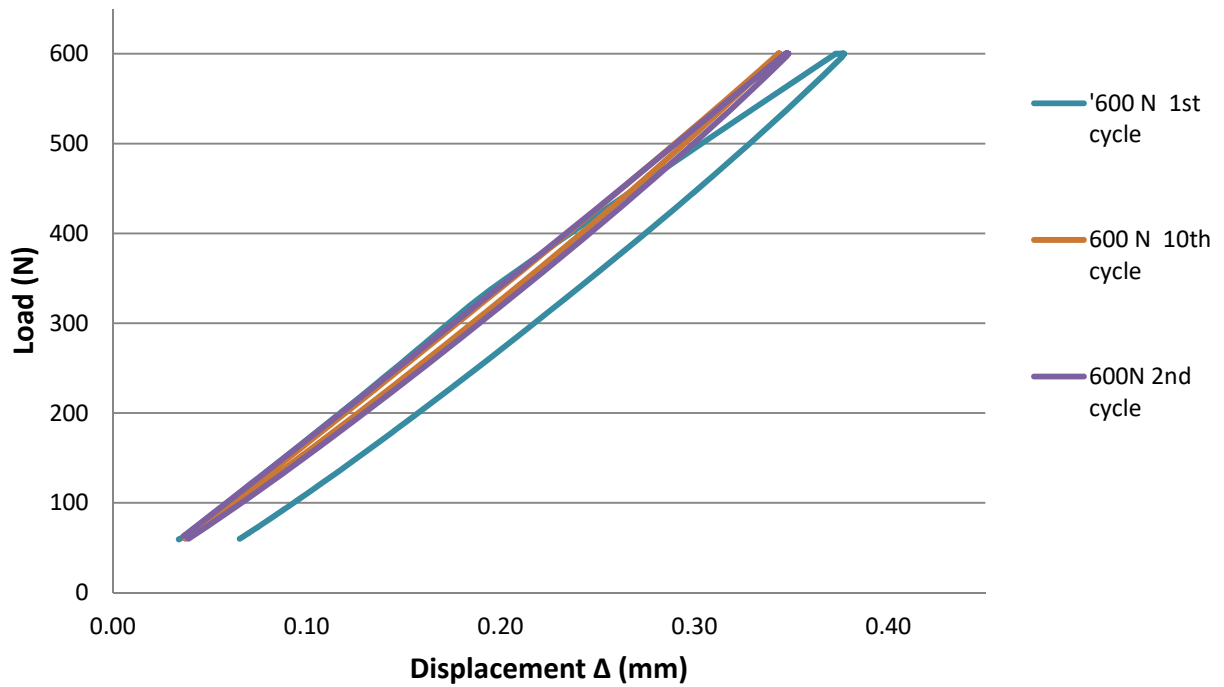


Diagram 3: Load - displacement curves in compression of sma c-ring at 600 newtons.

The loading rate in all experiments was 10 N/sec. Stress - displacement diagram and the modulus of elasticity of the material of the first and tenth loading cycle were derived from load – displacement curves (Diagrams 1, 2 and 3). For these calculations the analytical method of [4] was used, tailored to the c-ring geometry.

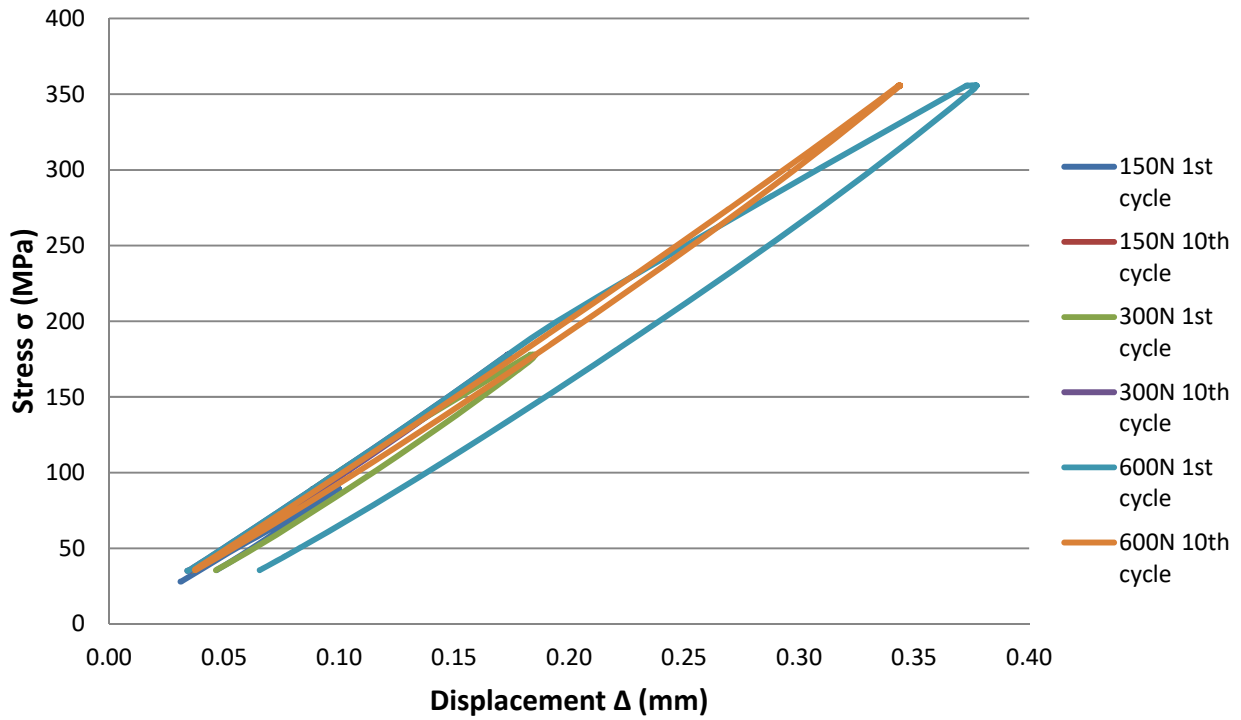


Diagram 4: Stress - displacement curves of first and tenth cycle in various stresses at the martensitic phase in twinned and detwinned specimen.

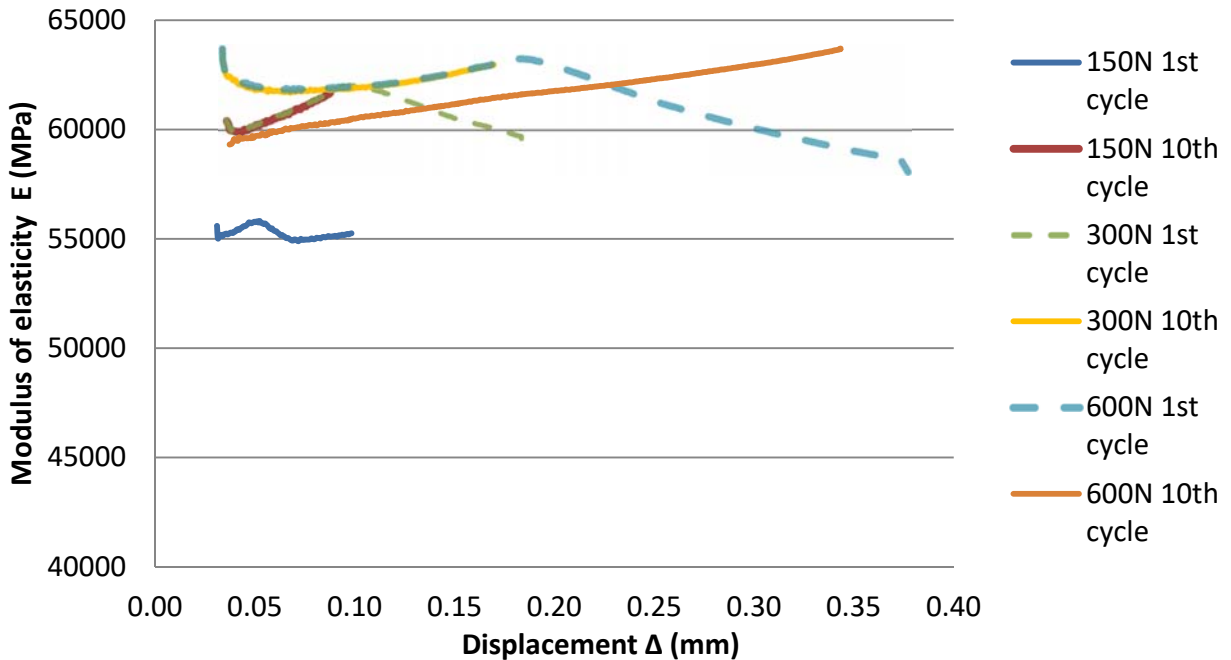


Diagram 5: Modulus of elasticity - displacement of first and tenth cycle in various stresses at the martensitic phase in twinned and detwinned specimen.



The observation of the diagrams shows the presence of hysteresis at unloading, when the specimen was compressed for the first time at 150, 300 and 600N. This is attributed to the stress-dependent detwinning caused to the material when it is in the martensitic phase. At 300 and 600N, after the first loading, the specimen appears completely detwinned each of these loads. It is worth noting that at the lower load of 150N, one cycle is not enough to complete detwinning and therefore an additional one is required. The modulus of elasticity during this 1st cycle (twinned material) at 150N was measured at 55 GPa (see Diagram 5). The stress distribution in the c-ring specimen volume, as illustrated in Figure 8, depends on the geometrical characteristics and the magnitude of the load. Thus, when the specimen shows the behavior of detwinned material, for a given load, this behavior is inverted if the load is increased and a detwinning stress develops in a new area of the specimen. This case can be observed in Diagram 5 between successive experiments from the 10th compression at 150N to the 1st compression at 300N and then from the 10th compression at 300N to the 1st compression at 600N, where the slope of the elasticity modulus changes rapidly downwards. For example, Figure 8 shows the stress distribution for a 600N load on the outer surface of the specimen, as we move angularly from the load direction to the maximum tensile area which is at 0°. If the load value is enough for the development of a stress higher than that of the yield point, the specimen shows first on 0° plastic deformation that grows angularly on the surface and to the inside of the specimen.

By applying a load of 600 N and once detwinning has been completed, the specimen presents a fully elastic behavior up to 600 N, without any further deformation between the loading cycles. This allows the selection of this load as the maximum applied in the fatigue investigations. After the first loading of the specimen, the device is adjusted to a new position, as the load changes due to the deformation caused by the detwinning. Adjustments are also made as the experiment progresses. The accumulation of imperfections mainly in the area of maximum stress lead to hardening of the area and changing of the stress field, thus forcing new areas to detwin.

The elastic behavior of the material allows to calculate its elastic modulus. Although the sample contains both detwinned and twinned areas, some of the twinned areas are not subject to stresses higher than the detwin limit. From the calculations and as shown in Diagram 5, the modulus of elasticity of the detwinned material reaches the value of 63 GPa.

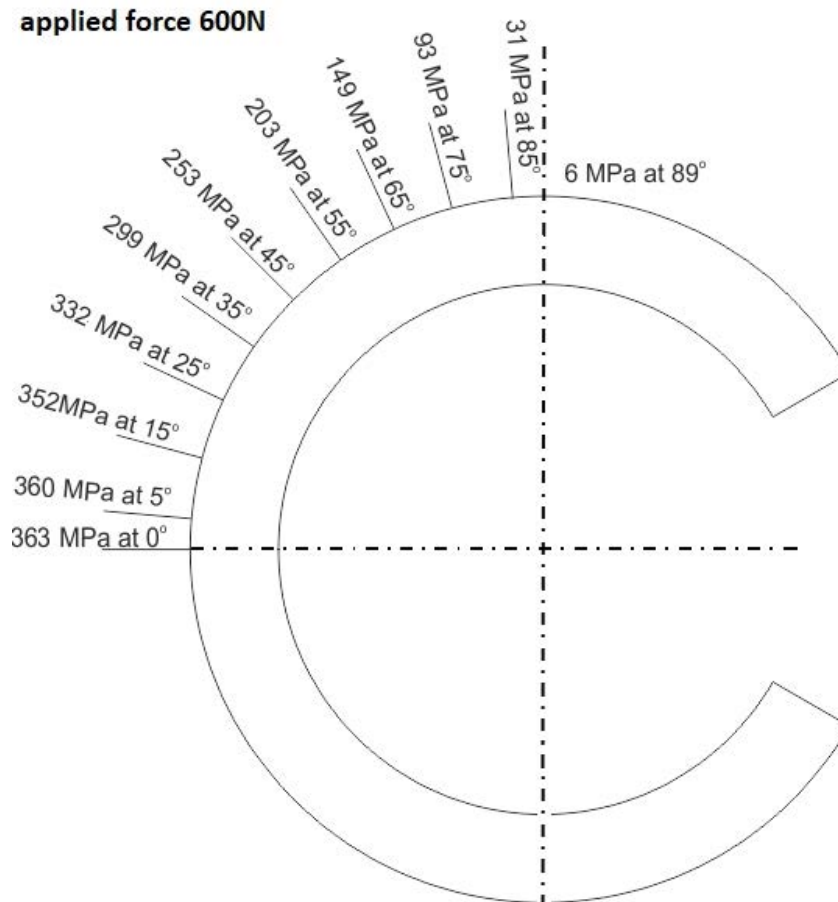


Figure 8: Stress distribution on the c-ring surface.

3.3 Changing of the modulus of elasticity by thermomechanical fatigue

The sample after forty cycles of phase transformation under constant deformation, between 70°C and 260°C and with various heating rates between 5 °C/min and 130 °C/min, was again subjected to compressive stress. Based on the force - displacement data, the stress - displacement and modulus of elasticity - displacement curves were extracted.

The experiment as shown in the Diagrams 6 and 7 showed a modulus of elasticity of 62 GPa, which is very close to the one defined in Diagram 5 for the sample with no thermal cycling.

After three mechanical cycles the specimen still presents a small hysteresis. This is attributed to the detwinning of the material during its cooling with simultaneous stress application, but also to the accumulation of imperfections, like dislocations, micro-cracks and other defects [6] that prevent the movement of the martensitic variants boundaries and as a result the residual deformation decreases per cycle, but is maintained for a larger number of cycles [11].

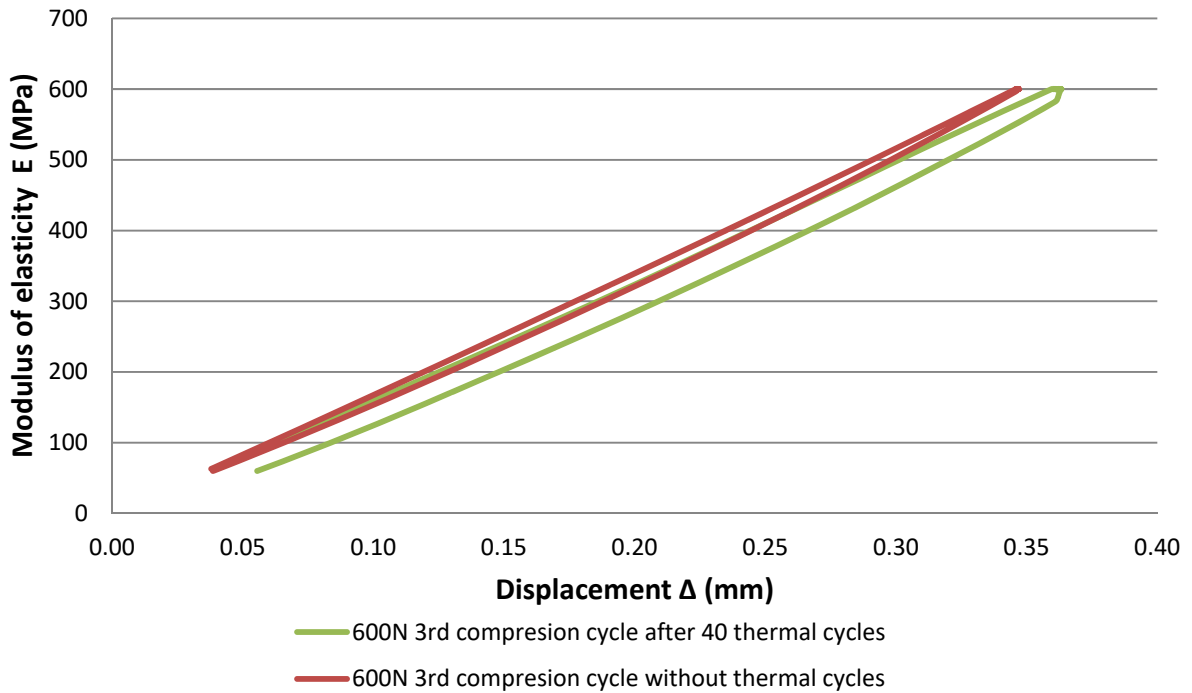


Diagram 6: Stress - displacement curve for NiTiHf c-ring after 40 thermal cycles compared with that of no thermal cycling.

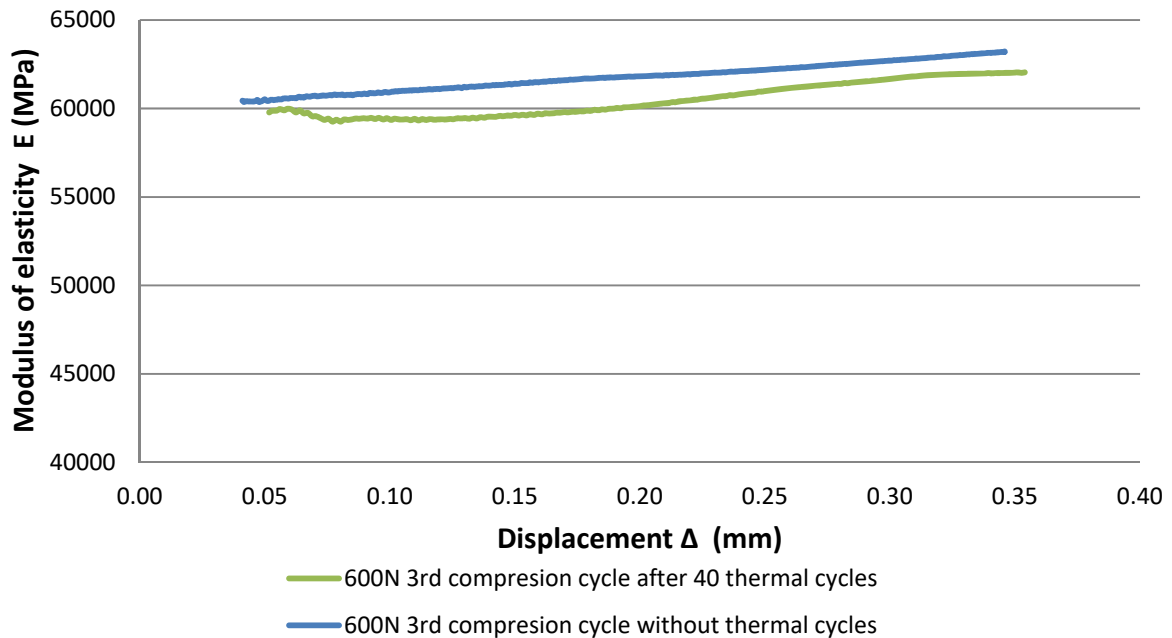


Diagram 7: Modulus of elasticity - displacement curve for NiTiHf c-ring after 40 thermal cycles compared with that of no thermal cycling.

4. TRANSFORMATION TEMPERATURES

4.1 Transformation temperatures with constant displacement.

To extract the transformation temperatures, the deformation of the c-ring was kept constant and the changes of the force were recorded as the material changes phases between martensite and austenite by heating and cooling during the thermal cycle.

To measure the experimental temperatures, two thermocouples were initially placed inside the container, one being in contact with the c-ring sample while thermally insulated on its free surfaces, and the second served for recording the air temperature (see Figures 9 and 10).

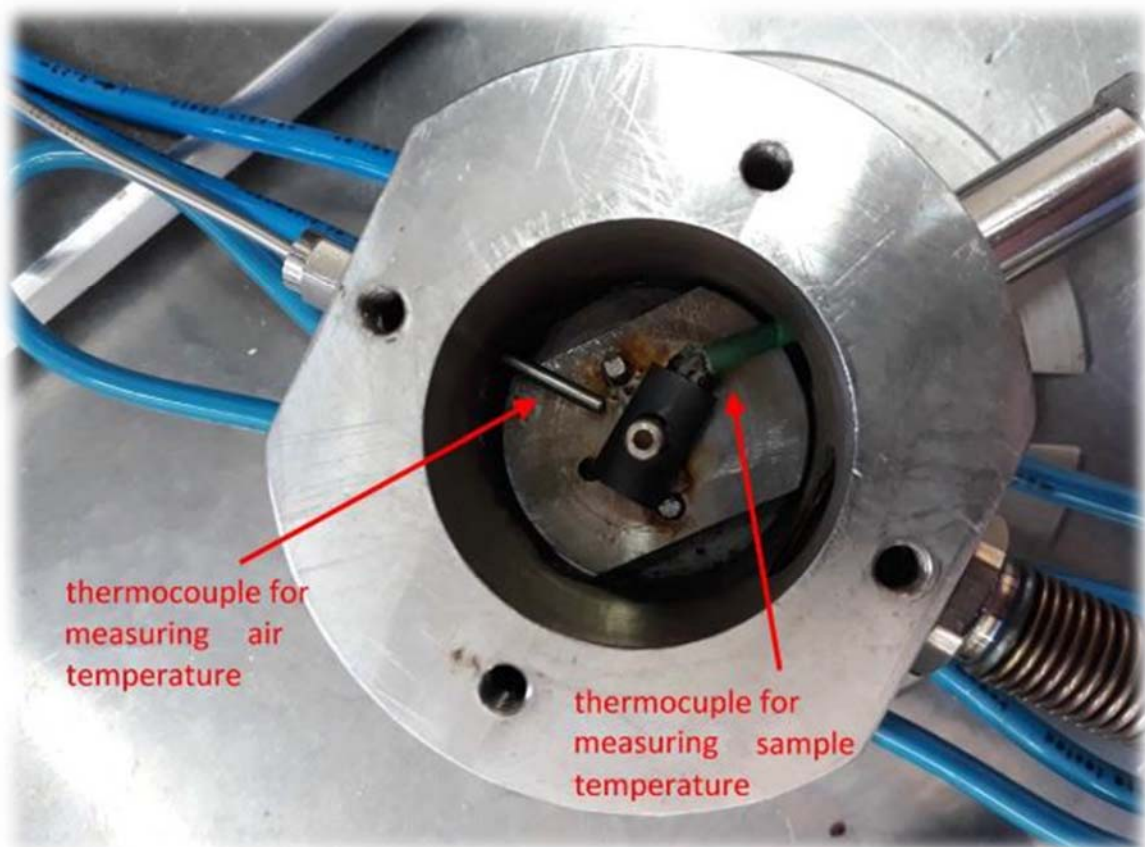


Figure 9: Container with two thermocouples for measure the temperature of the c-ring.

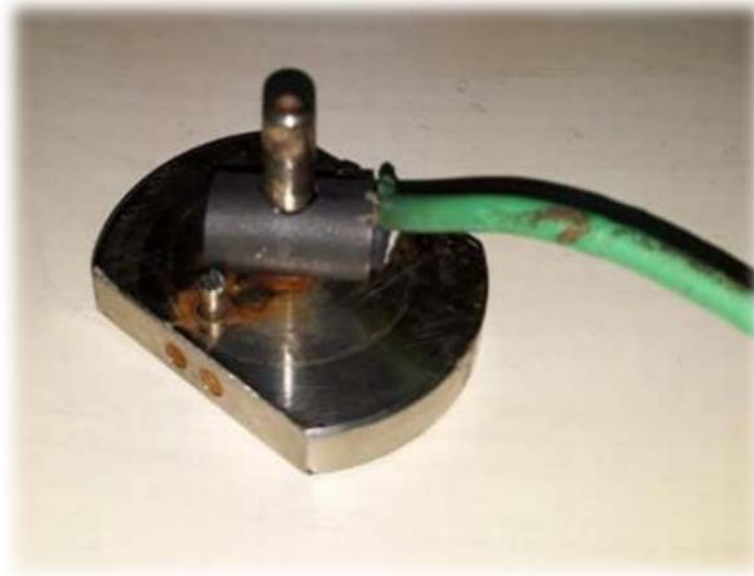


Figure 10: Installation of a thermocouple to measure the temperature of the specimen.

The heating and cooling rates of the air in the vessel, in the temperature range of interest between 150°C and 300°C, were kept constant at 5°C/min in all experiments conducted. By capturing the difference between the temperatures measured at the air and at the sample during heating and cooling, two trendlines were derived with corresponding equations, one for heating and one for cooling (see Diagram 8). The reason for obtaining such a relationship of the temperature difference measured at the air and at the sample during heating and cooling was to have contactless estimation of the sample temperature by just measuring the air temperature throughout the temperature range of interest. In this way, the distortion of stress distribution and the creation of galvanic conditions during corrosion can be avoided.

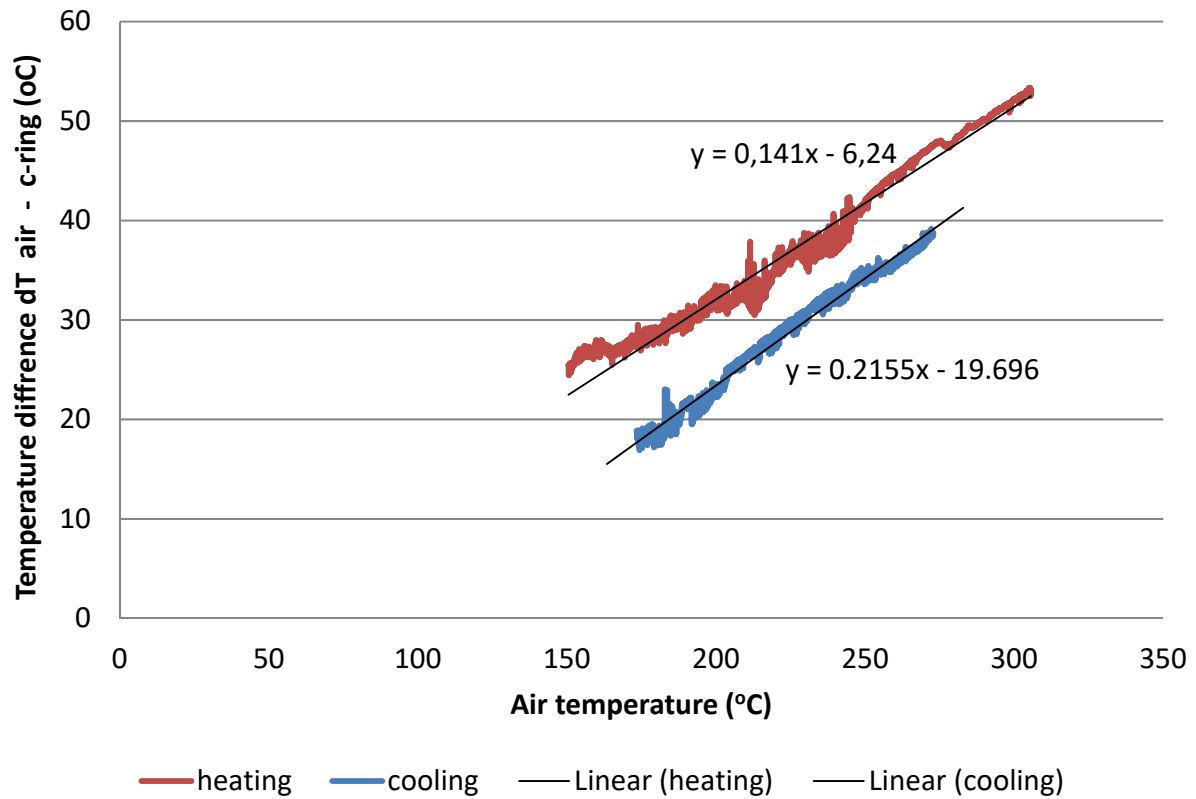


Diagram 8: Temperature difference between the c-ring and the air during heating and cooling.

The following Diagrams (9, 10, 11, 12) show the force-temperature curves for different starting force values. When a change in the slope of the curve is experienced, a phase transformation from martensite to austenite is initiated or completed during heating, and vice versa during cooling.

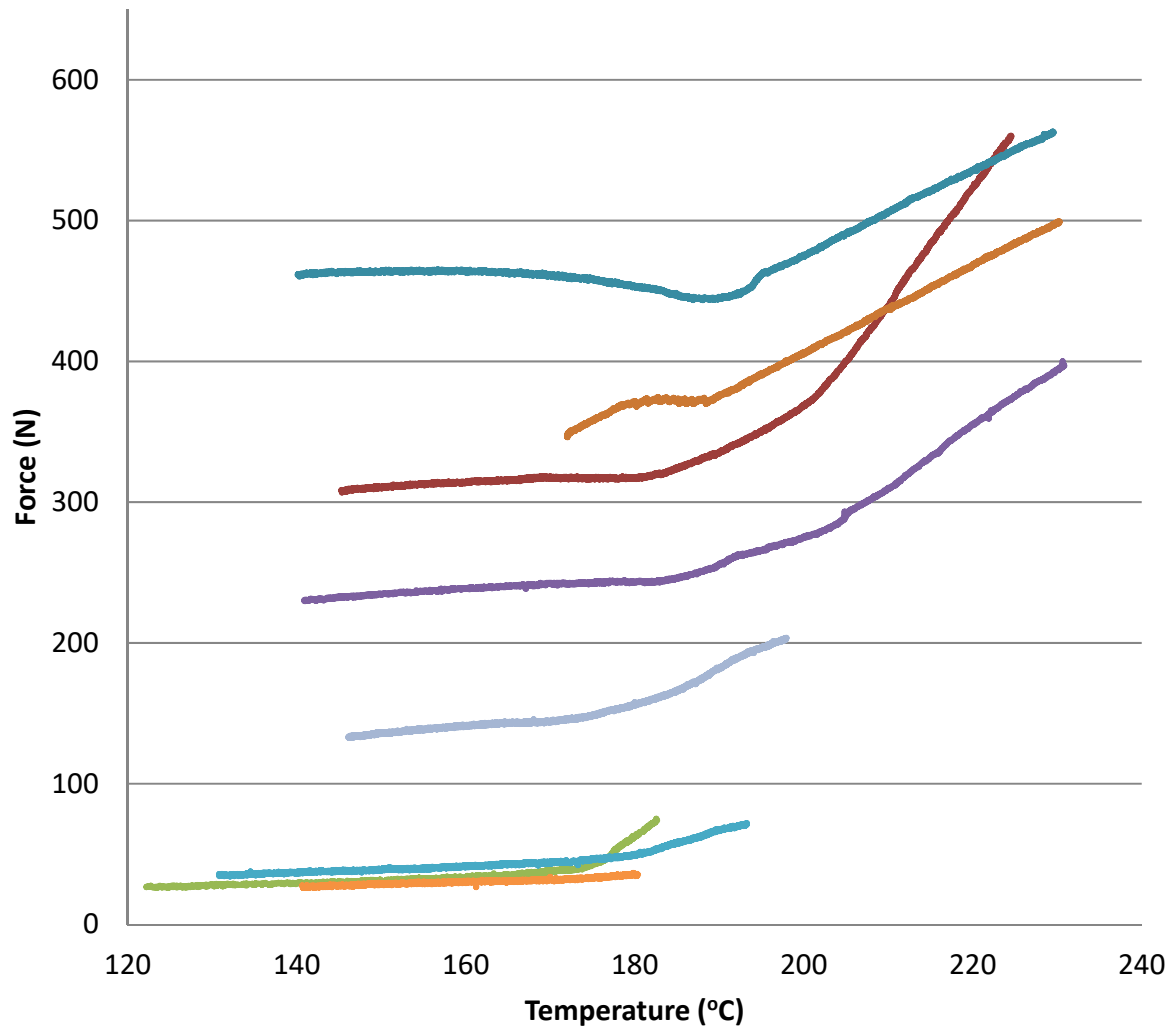


Diagram 9: Temperatures of austenitic transformation start (As) during heating, at various force values.

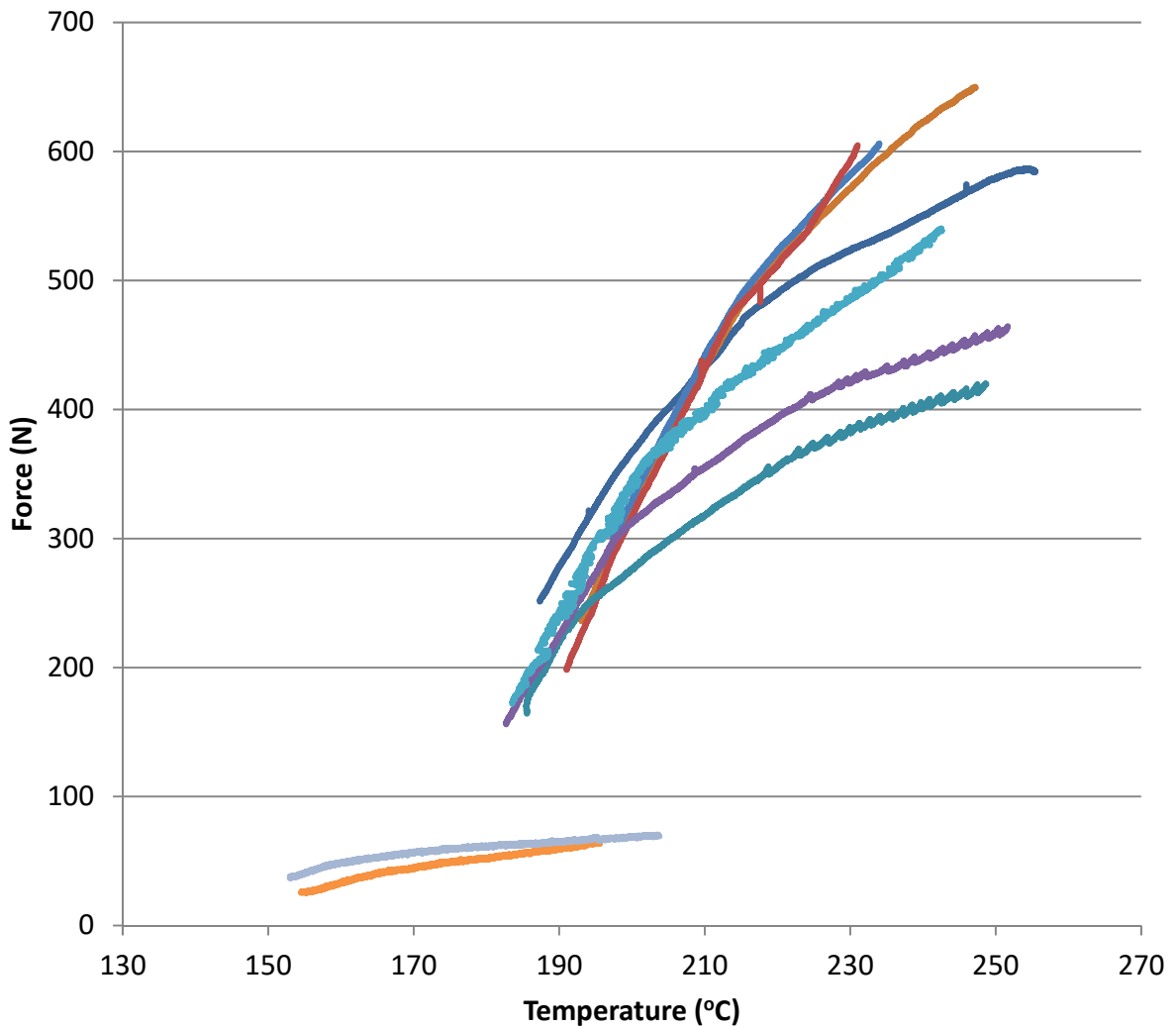


Diagram 10: Temperatures of martensitic transformation start (Ms) during cooling, at various load levels.

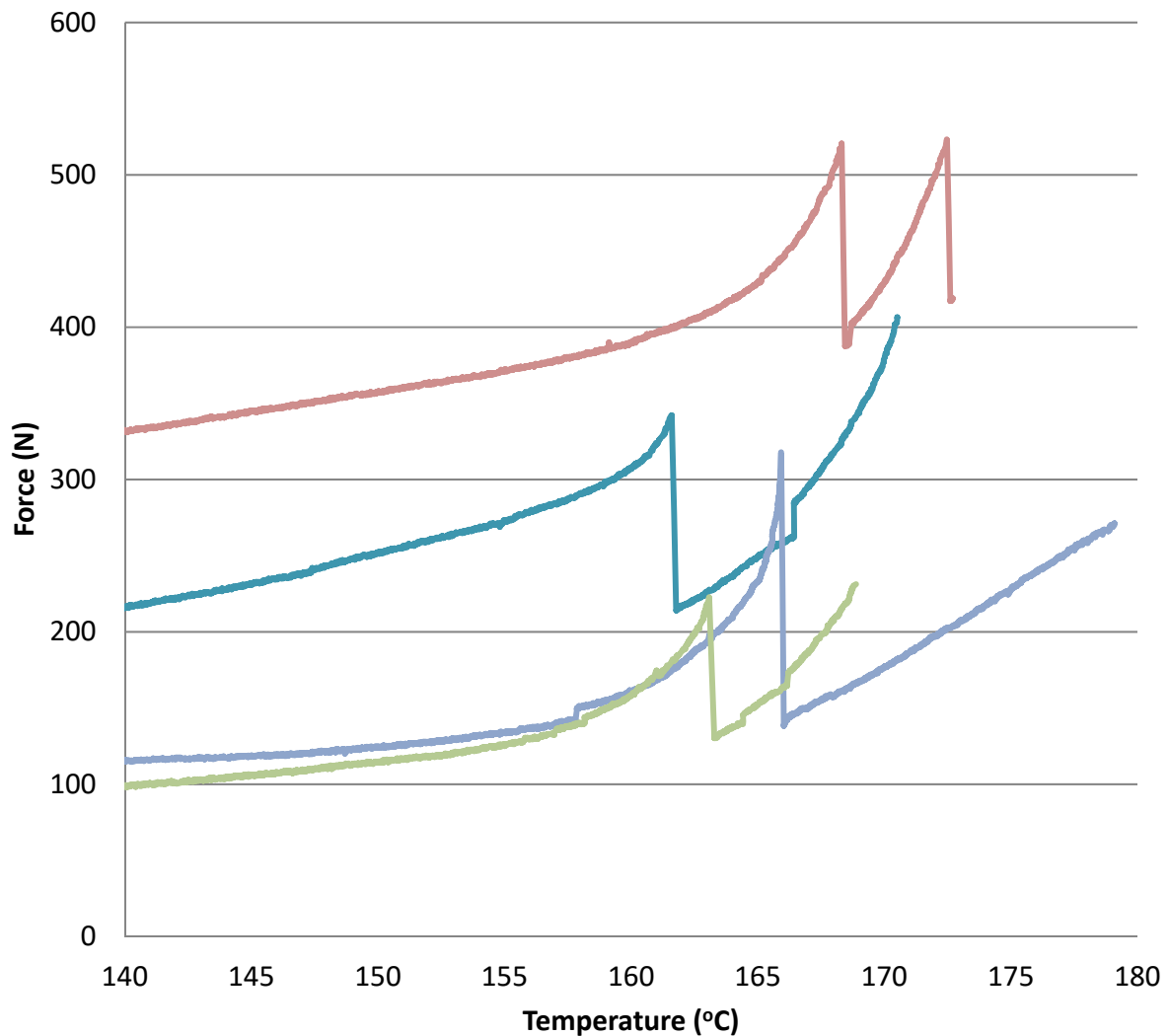


Diagram 11: Temperatures of martensitic transformation finish (Mf) during cooling, at various load levels.

From the phase transformation diagrams, the critical transformation start and finish temperatures at various load levels were extracted and plotted, as summarized in Diagrams 13 and 14. With the help of trendlines, the force - transformation temperature equations are obtained.

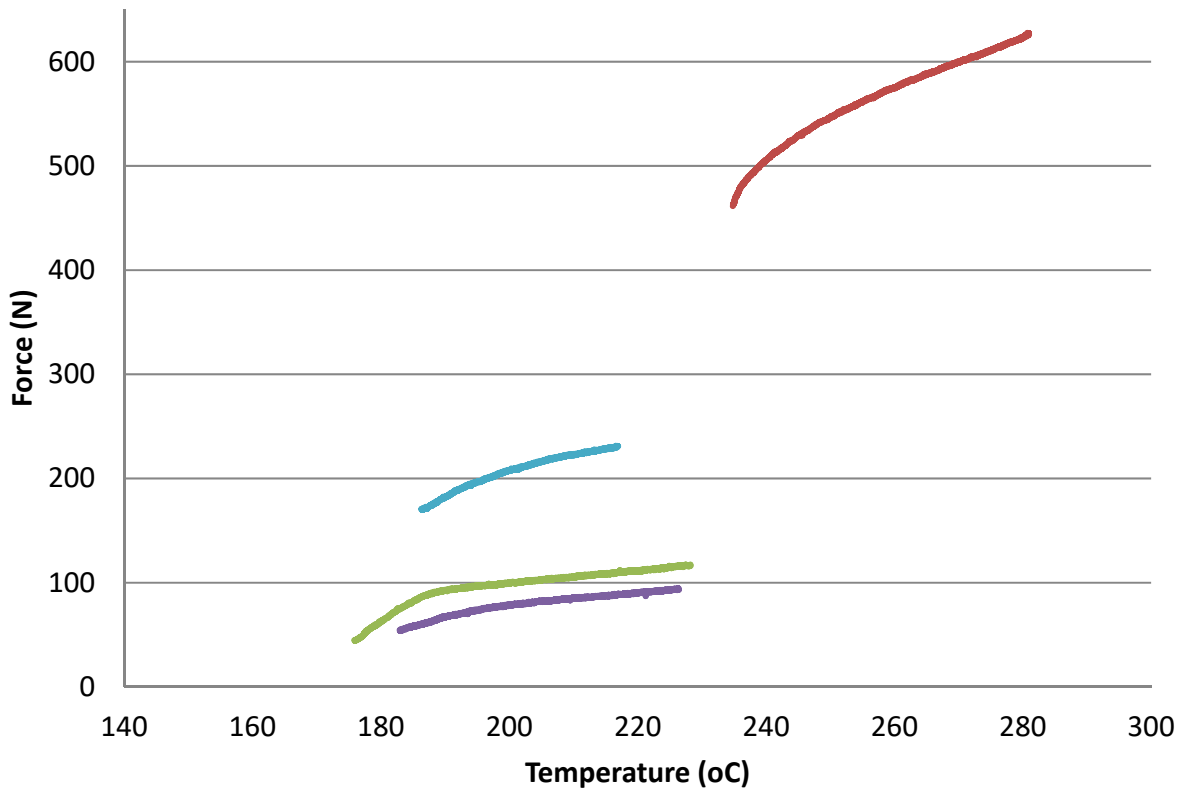


Diagram 12: Temperatures of austenitic transformation finish (Af) during heating, at various load levels.

From the trendline equations of Diagram 14, the estimated transformation temperature for each value of applied stress can be calculated as follows:

$$M_f = 0.088 * \text{stress} + 151$$

$$M_s = 0.168 * \text{stress} + 163$$

$$A_s = 0.068 * \text{stress} + 172$$

$$A_f = 0.186 * \text{stress} + 180$$

In the uncharged state, the values resulting from these equations are:

$$M_f: 151 \text{ }^\circ\text{C}, M_s: 163 \text{ }^\circ\text{C}, A_s: 172 \text{ }^\circ\text{C}, A_f: 180 \text{ }^\circ\text{C}$$

By applying a load of 600N, the values resulting from these equations are:

$$M_f: 185 \text{ }^\circ\text{C}, M_s: 229 \text{ }^\circ\text{C}, A_s: 199 \text{ }^\circ\text{C}, A_f: 253 \text{ }^\circ\text{C}$$

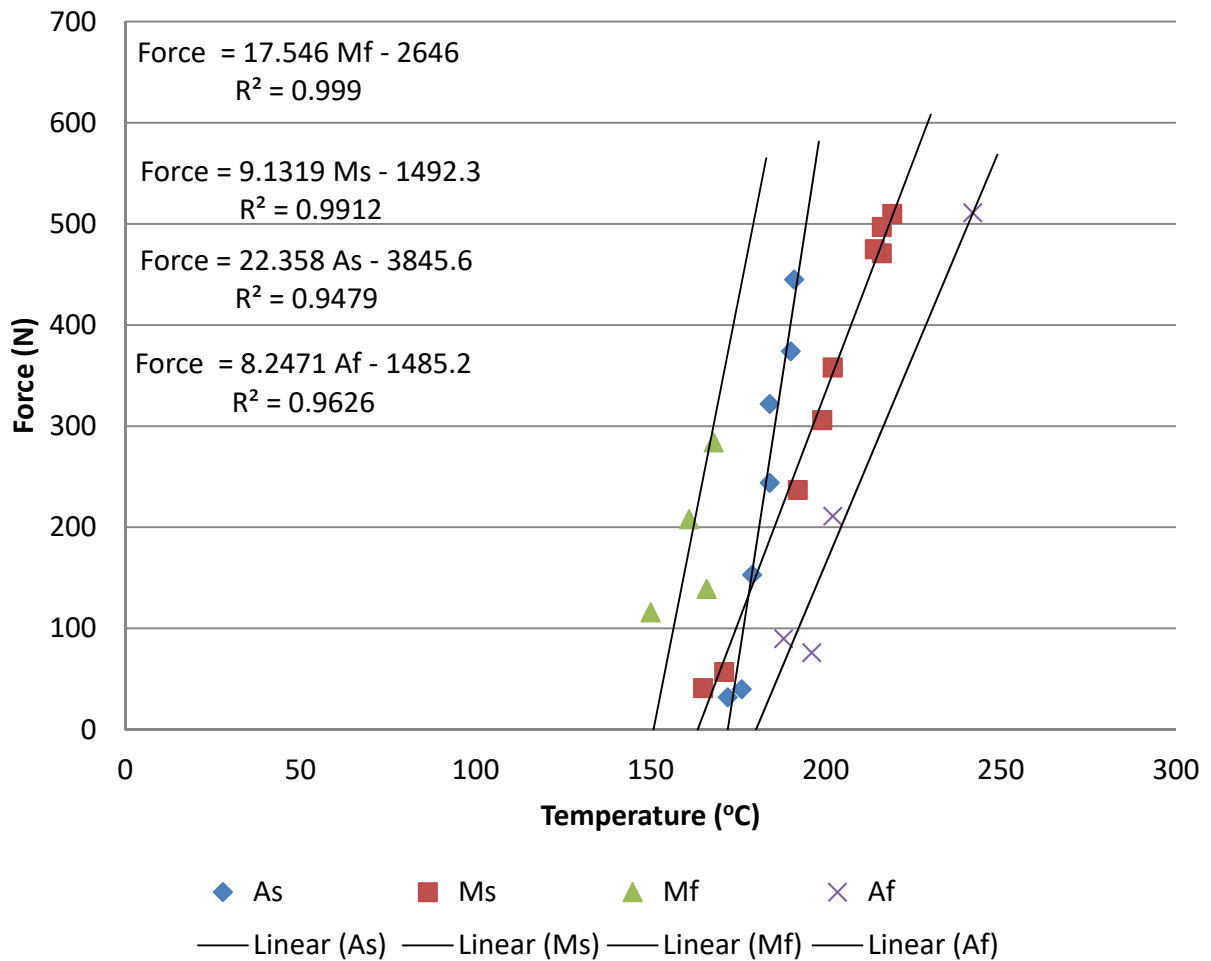


Diagram 13: Force vs. transformation temperature diagram.

The previous diagram can be transformed into a stress- transformation temperature diagram, by which the corresponding trendline equations may result.

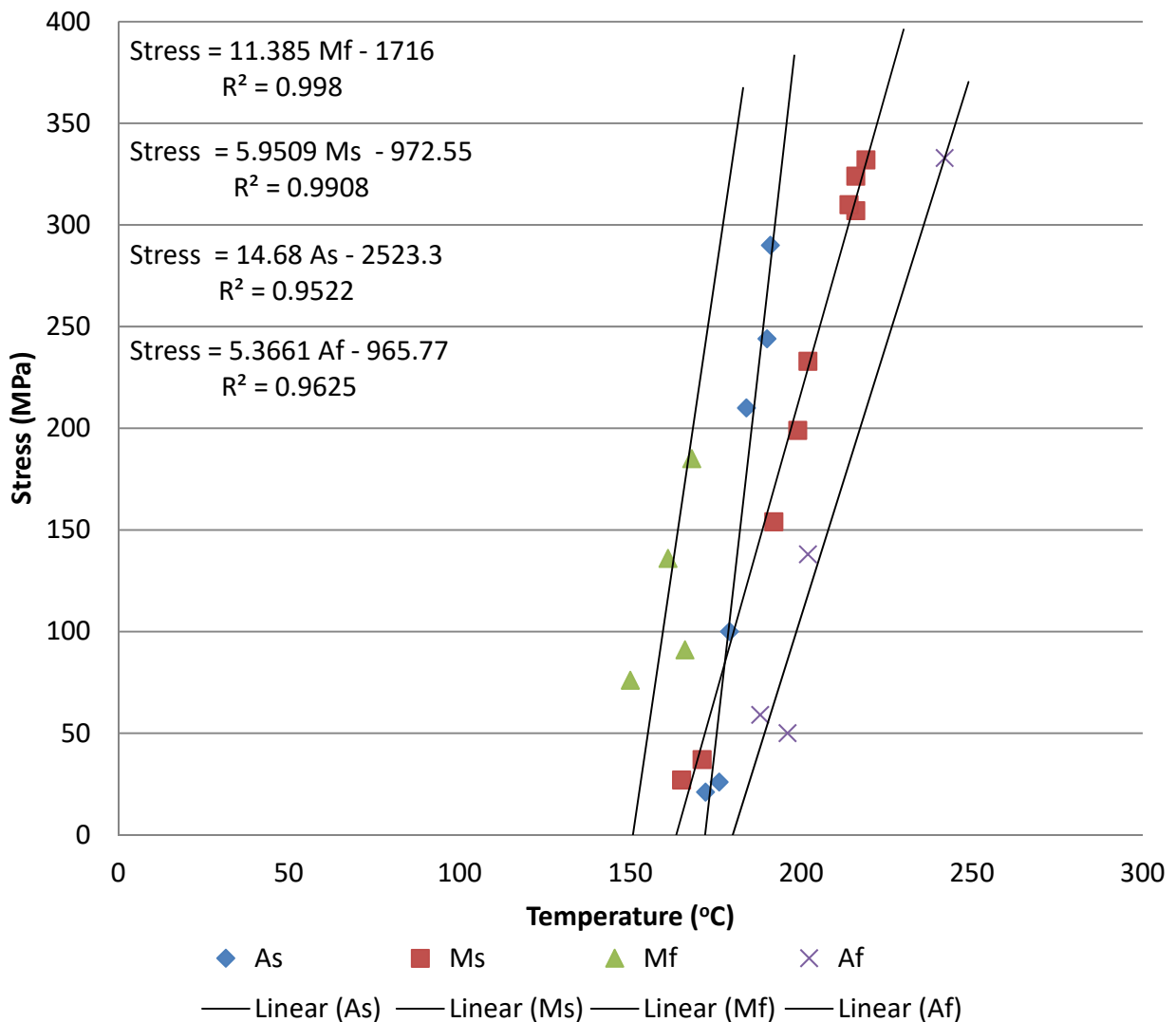


Diagram 14: Stress vs. transformation temperature diagram.

4.2 Transformation temperatures with isobaric tension tests

To validate the phase transformation results of the previous experimentation employing the developed set-up, a comparison with data obtained from isobaric tension tests at different stress values and temperatures was conducted. These data are presented in the Diagram 15. From the equations of the trendlines, the transformation temperature for each of the applied stress values can be calculated.

$$Mf = 0.052 * stress + 177$$

$$Ms = 0.132 * stress + 180$$



$$A_s = 0.076 \cdot \text{stress} + 190$$

$$A_f = 0.146 \cdot \text{stress} + 198$$

In the uncharged state the values resulting from these equations are:

Mf: 177 °C, Ms: 180 °C, As: 190 °C, Af: 198 °C

By applying a load of 600 N, the values resulting from these equations are:

Mf: 197 °C, Ms: 232 °C, As: 220 °C, Af: 255 °C

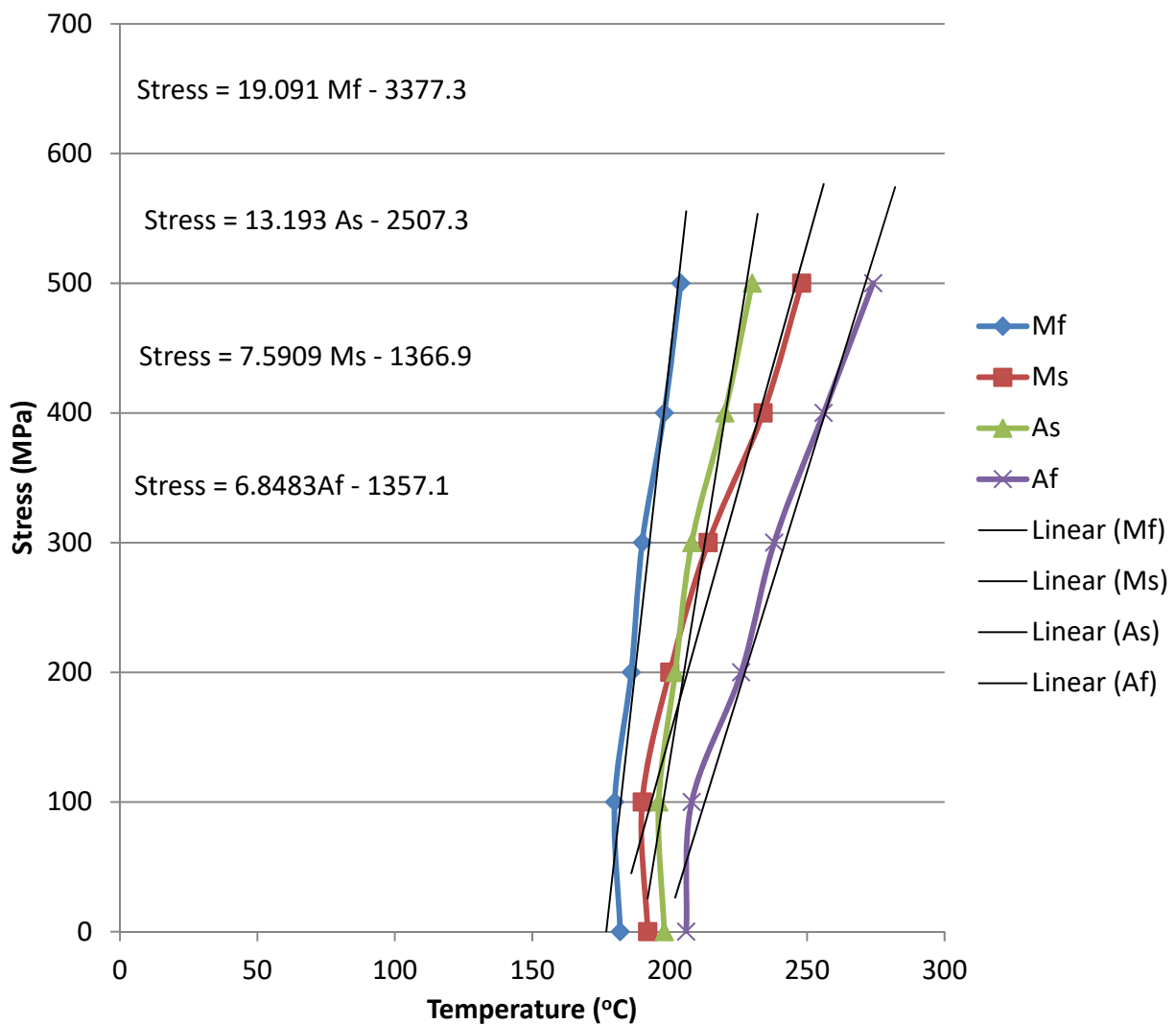


Diagram 15: Phase transformation values from isobaric tension tests at different stress values and temperatures. The calculation equations are exported using the trendlines.



4.3 Transformation temperatures obtained by differential scanning calorimetry (DSC)

The transformation temperatures obtained by differential scanning calorimetry of the “heat-treated” specimen are presented in Diagram 16 for ten repetitive thermal cycles. The transformation temperatures for the 1st and the 9th thermal cycle are given below:

- 1st cycle: Mf: 138 °C, Ms: 161 °C, As: 181 °C, Af: 203 °C
- 9th cycle: Mf: 128 °C, Ms: 154 °C, As: 156 °C, Af: 186 °C

There is a clear tendency of the material to stabilize, as most of the measurements are accumulated when the number of cycles is increasing. At the 9th thermal cycle, the transformation temperatures are slightly smaller compared to the 1st.

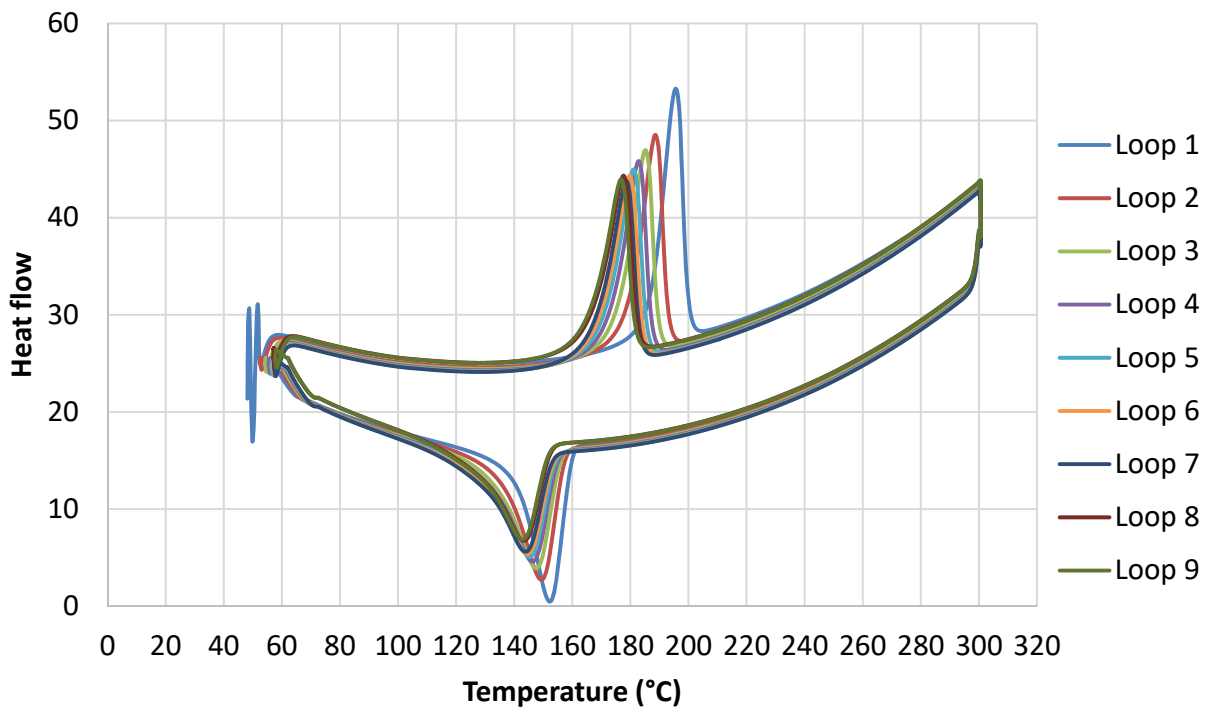


Diagram 16: DSC of the “heat-treated” material.

The corresponding transformation temperature values from the differential scanning calorimetry of the “as-received” specimen can be viewed by Diagram 17. The transformation temperatures for the 1st and the 9th thermal cycle are given below:

- 1st cycle: Mf: 134 °C, Ms: 162 °C, As: 185 °C, Af: 208 °C
- 9th cycle: Mf: 127 °C, Ms: 151 °C, As: 154 °C, Af: 180 °C



As it can be observed again, the corresponding values of the 9th thermal cycle are smaller compared to the 1st and tend to stabilize.

Comparing the two charts (Diagrams 16 and 17) for the “heat-treated” specimen and the “as received” samples, one can easily yield that the transformation temperatures did not change significantly by the heat treatment.

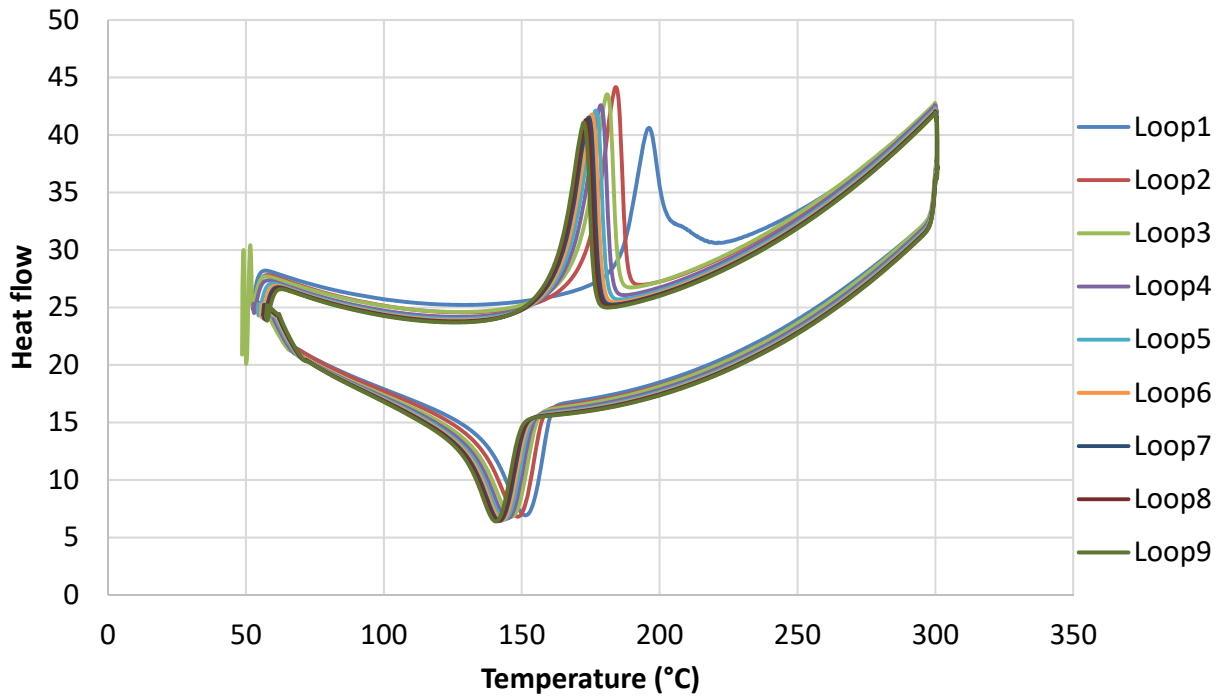


Diagram 17: DSC of the “as received” material,

5. MICROSTRUCTURAL CHARACTERIZATION

5.1 Scanning electron microscopy (SEM)

The samples were examined for their microstructure at room temperature employing by a Jeol JSM – 6390LV scanning electron microscope (SEM) see Figure 11. For this purpose, two sections 1.5 mm thick were cut from two different c-ring samples, one “as received” and one subjected to heat treatment at 550 °C for 3 hours. Figures 12 and 13 present the corresponding SEM images, where in both Martensitic structures can be observed at different orientations (variants) [7].



Figure 11: Scanning electron microscope (Jeol JSM – 6390LV) employed in the microstructure investigation.

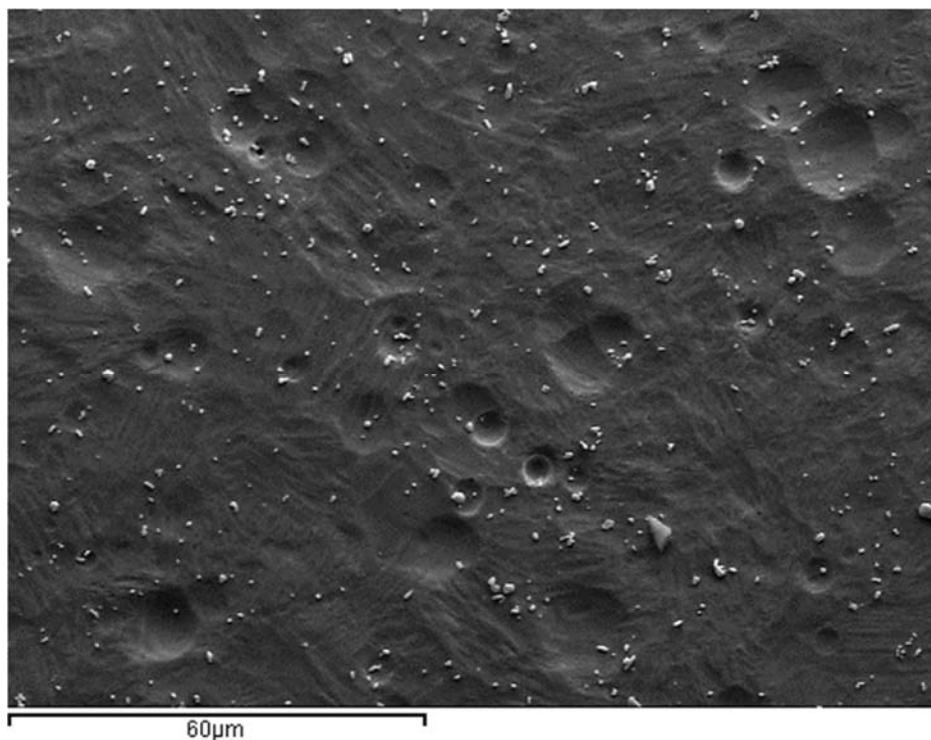


Figure 12: SEM image of the “as received” specimen, where the Martensitic structures can be observed in different orientations (variants).

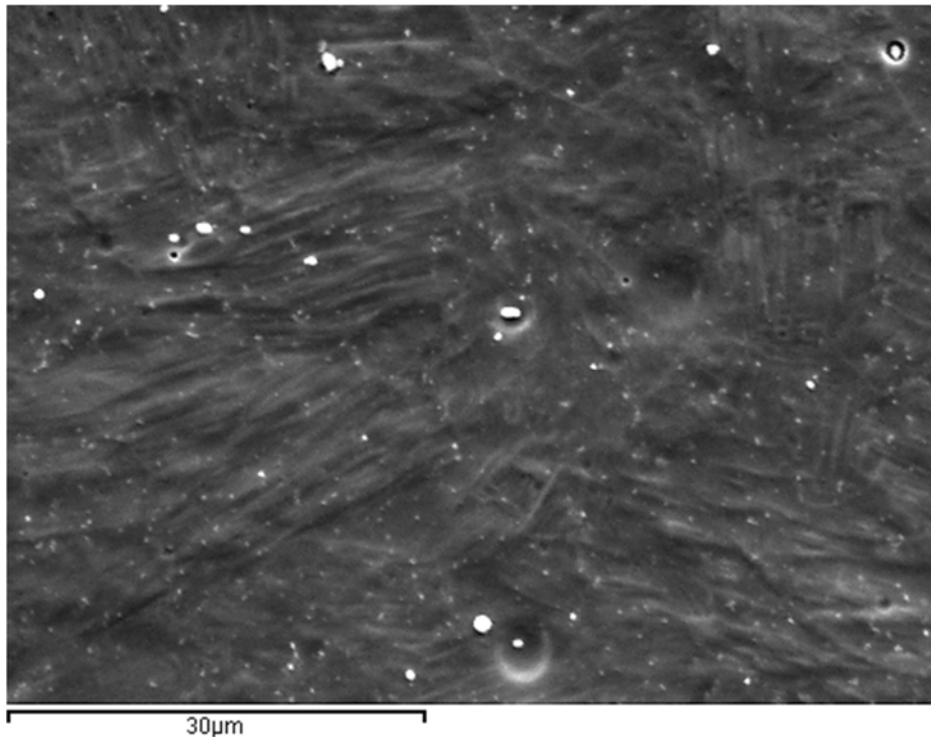


Figure 13: SEM image of the “heat-treated” specimen where the Martensitic structures can be observed in different orientations (variants).

6. FATIGUE EXPERIMENTS

Fatigue experiments were carried out with the sample in the martensitic phase at room temperature and in the austenitic phase at a temperature of 260°C. Furthermore, in the martensitic phase, three combined corrosion and fatigue experiments were performed in a 3.5 wt % NaCl aqueous solution. In the second combined corrosion and fatigue experiment, the sample was first subjected to electrochemical cleaning to remove the external oxides and measure the open circuit potential. In all experiments the applied force exerted on the c-ring cyclically varied between $F_{\min} = 0 \text{ N}$ και $F_{\max} = 600 \text{ N}$ ($R=0$) at a frequency of 40Hz. Based on the analytical calculation of the stress for the force of 600 N the maximum stress developed on the surface of the sample raises to 363 MPa. All samples were heat treated at 550 °C for 3 hours prior to testing. Below is a bar chart (Diagram 18) with the results of the experiments, as well as the number of load cycles.

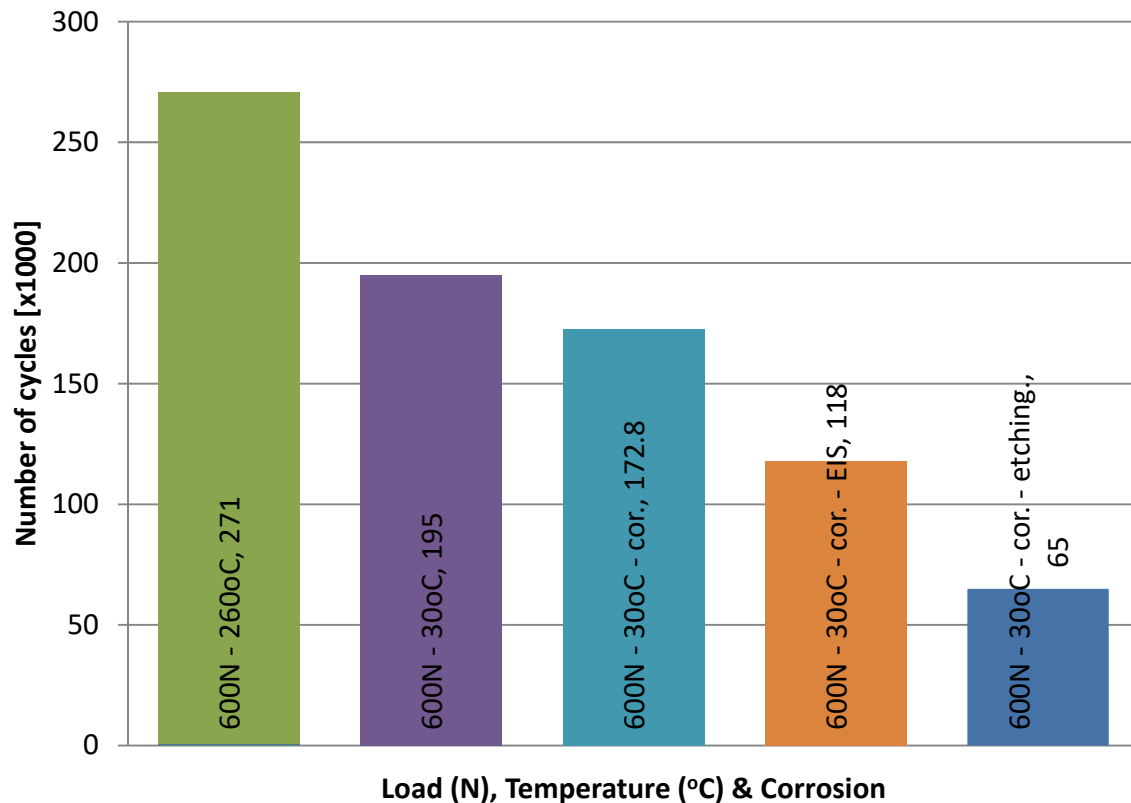


Diagram 18: Fatigue results of NiTiHf in martensitic and austenitic phase, as well as in various corrosion conditions. Loading frequency: 40Hz, loading amplitude: 0 N - 600N (R=0).

From the fatigue experiments it was observed that the specimen in the austenite phase exhibits longer life span than in the martensite phase (271.000 cycles versus 195.000 cycles). The specimens subjected to fatigue in a corrosive environment showed a shorter life span with variations depending on the corrosion technique used and the sample pre-etching. These results will be further discussed in Chapter 7.

6.1 Fractographic analysis (for specimen with fatigue at martensitic phase)

6.1.1 Stereo microscopy

The different surface-initiated fracture modes of the samples during pure fatigue and corrosion-fatigue can be visualized from the selection of characteristic fractographs taken by stereo microscope (Leica MS5 equipped with Leica DFC490 digital camera). The images of Figures 14, 15 and 16 illustrate the fractured surface of the specimen, resulting from corrosion-free fatigue at ambient temperature (martensitic phase).

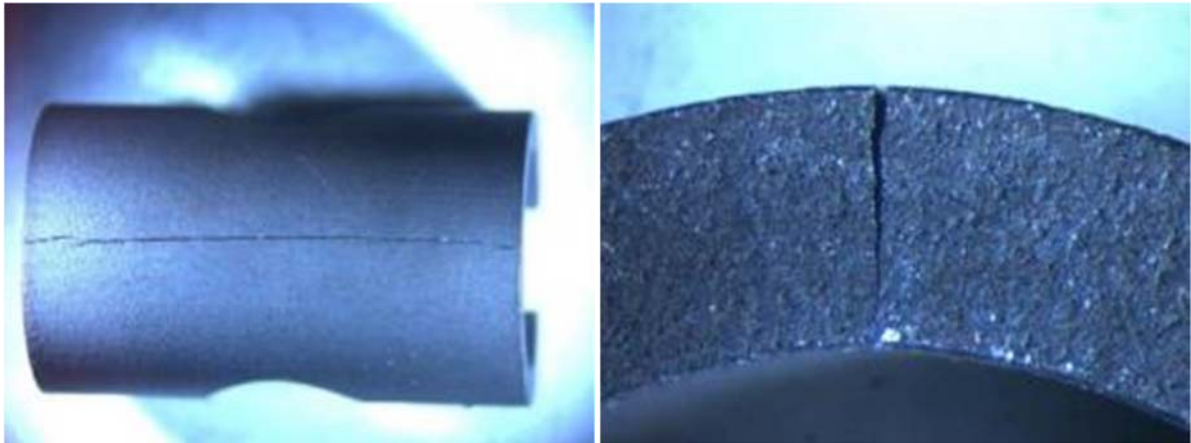


Figure 14: Sample with fatigue crack in martensitic phase after 195.000 cycles. The crack starts at the right-hand side of the specimen at the outer surface where the maximum tensile stress develops.

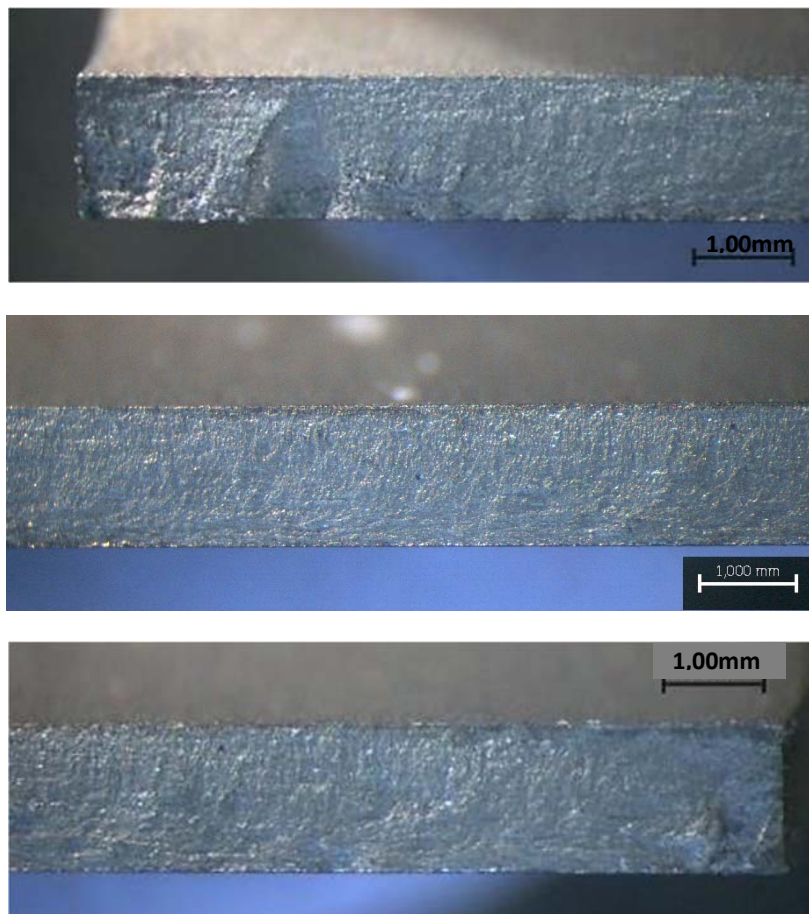


Figure 15: Fractography (16x) of the specimen with fatigue at martensitic phase. The top image shows the end of the crack, the second image shows the middle and the bottom image the crack initiation site.

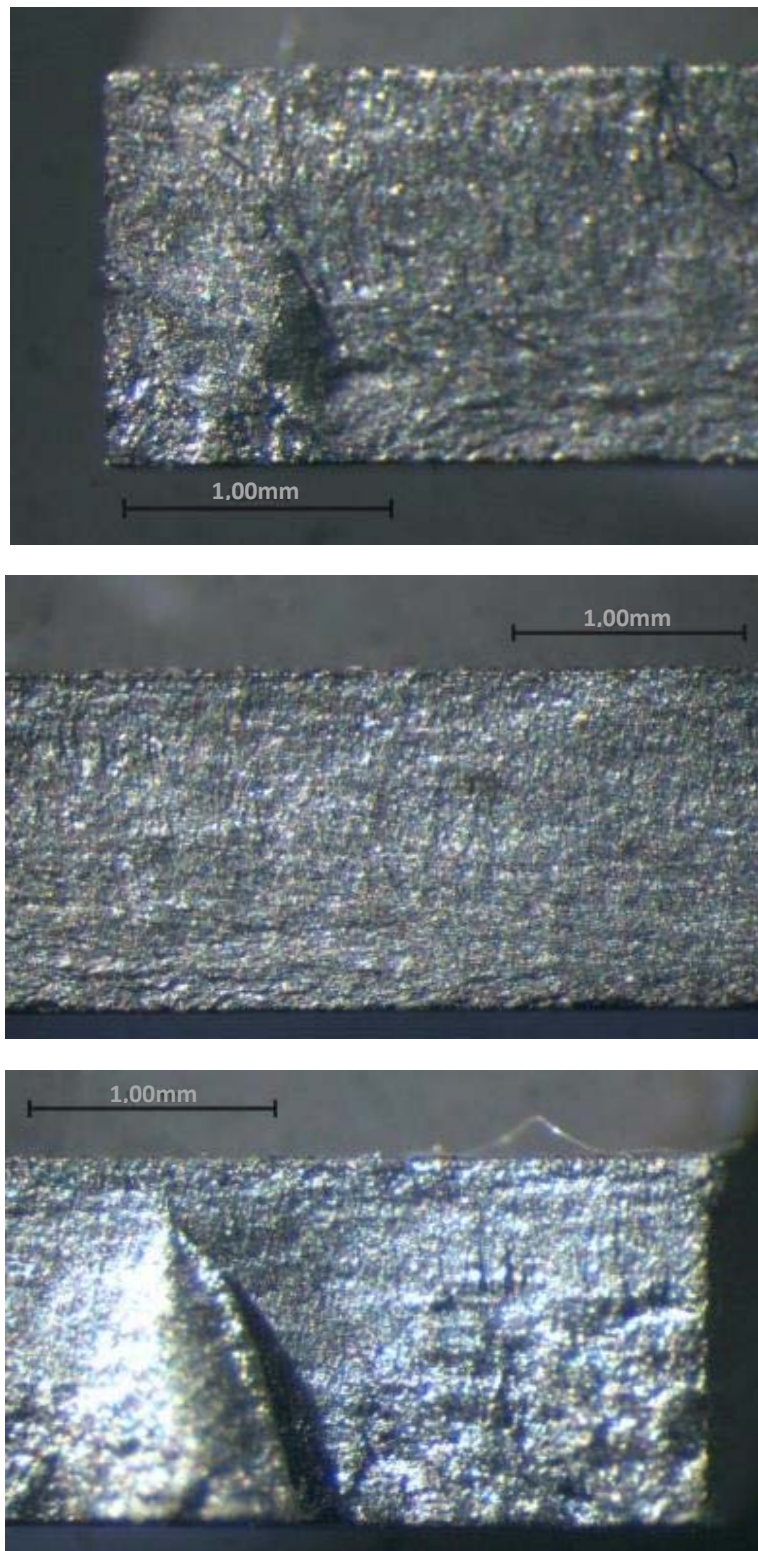


Figure 16: Fractography (40x) of the fractured surface of the other c-ring segment, where the top image shows the end of the crack the second image the middle and the bottom image the crack initiation site.

6.1.2 Scanning electron microscopy

The images of Figure 17 were taken by scanning electron microscopy and illustrate the fractured surface of the specimen, resulting from a fatigue experiment at ambient temperature (martensitic phase) after 195,000 cycles.

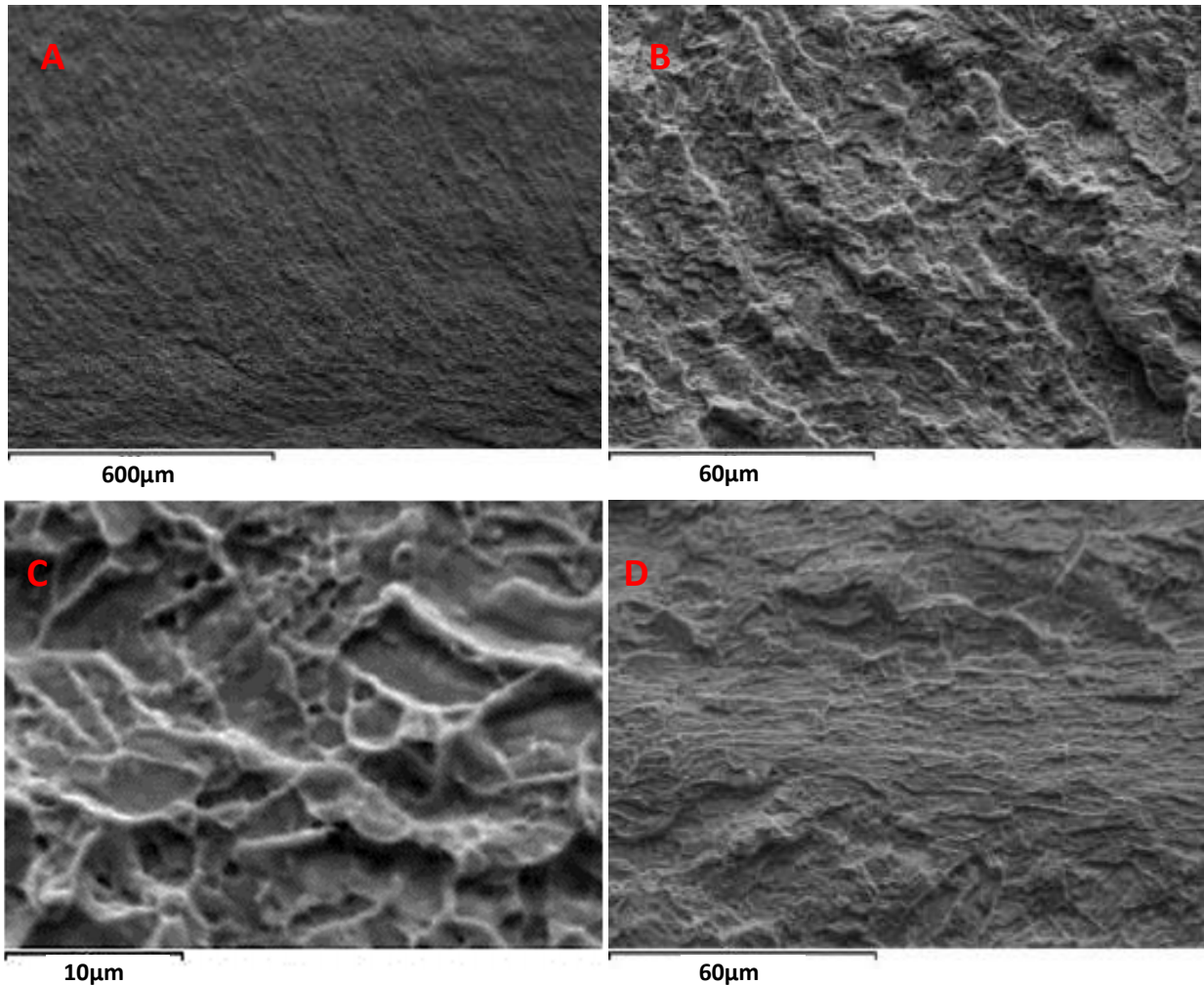


Figure 17: Scanning electron microscopy images of the NiTiHf SMA c-ring fractured surface in the martensitic phase.

In the images (a) and (b) the macroscopic waveform striations of fatigue in the radial direction of the c-ring are visible. In image (c), a morphology matching transgranular cracking appears, while in image (d) the waveform striations change orientation due to the transition from the compressive stresses at the inner surface to the tensile stresses at the outer surface.



6.1.3 Optical microscopy

The image Figure 18 was taken through a Leica DM4000M optical microscope, illustrating the granular microstructure of the sample in the fractured region. The surface texturing does not allow the capturing of a focused image all over the picture.

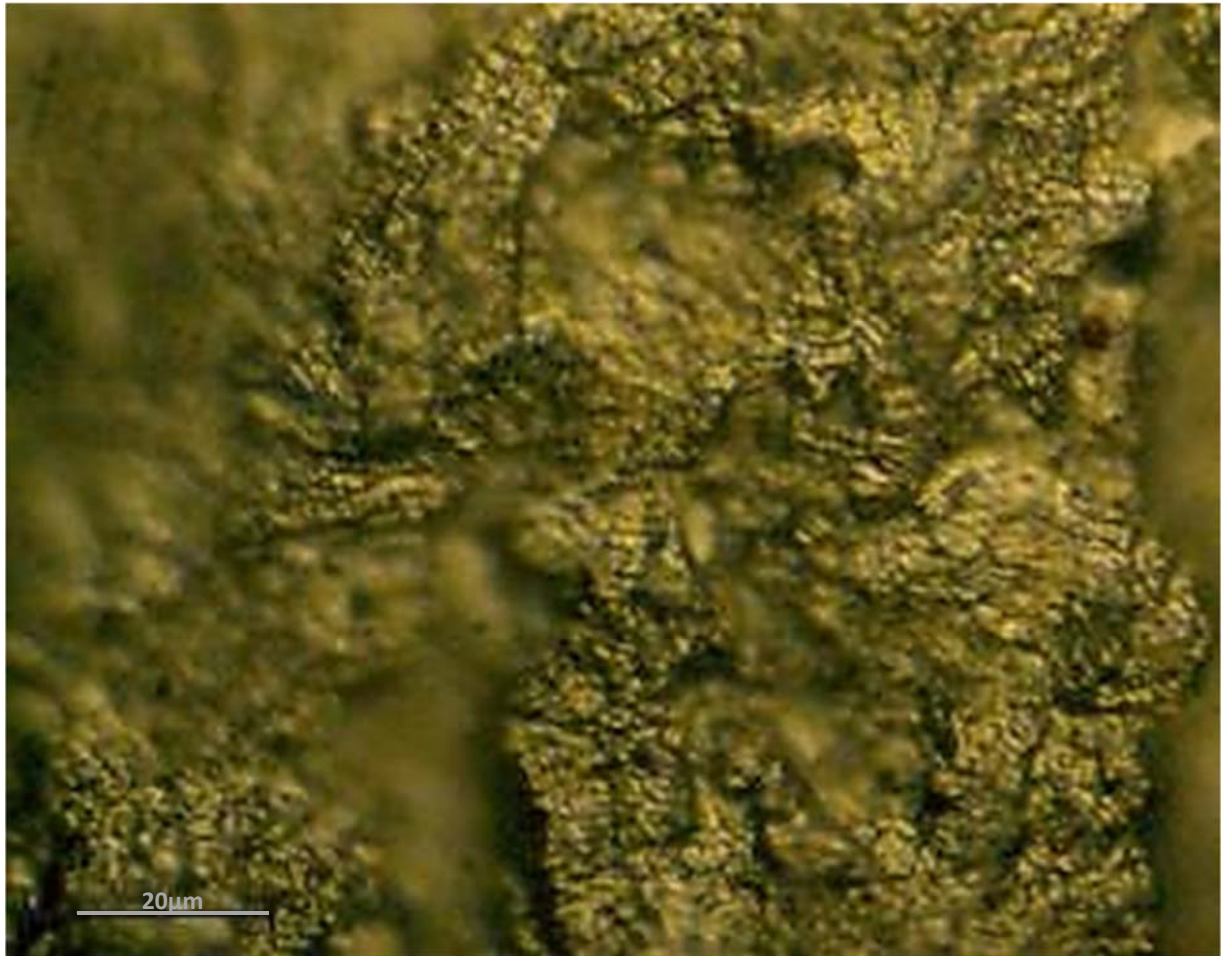


Figure 18: Granular microstructure of the sample in the fractured region.

6.2 Fractographic analysis (specimen with fatigue at austenitic phase)

6.2.1 Stereo microscopy

The images of Figures 19, 20 and 21 illustrate the fractured surface of the NiTiHf sma c-ring specimen, resulting from a fatigue experiment at 260°C (austenitic phase) after 271.000 cycles.



Figure 19: Sample with fatigue crack in austenitic phase after 271.000 cycles. The crack starts at the left-hand side of the specimen at the outer surface where the maximum tensile stress develops.

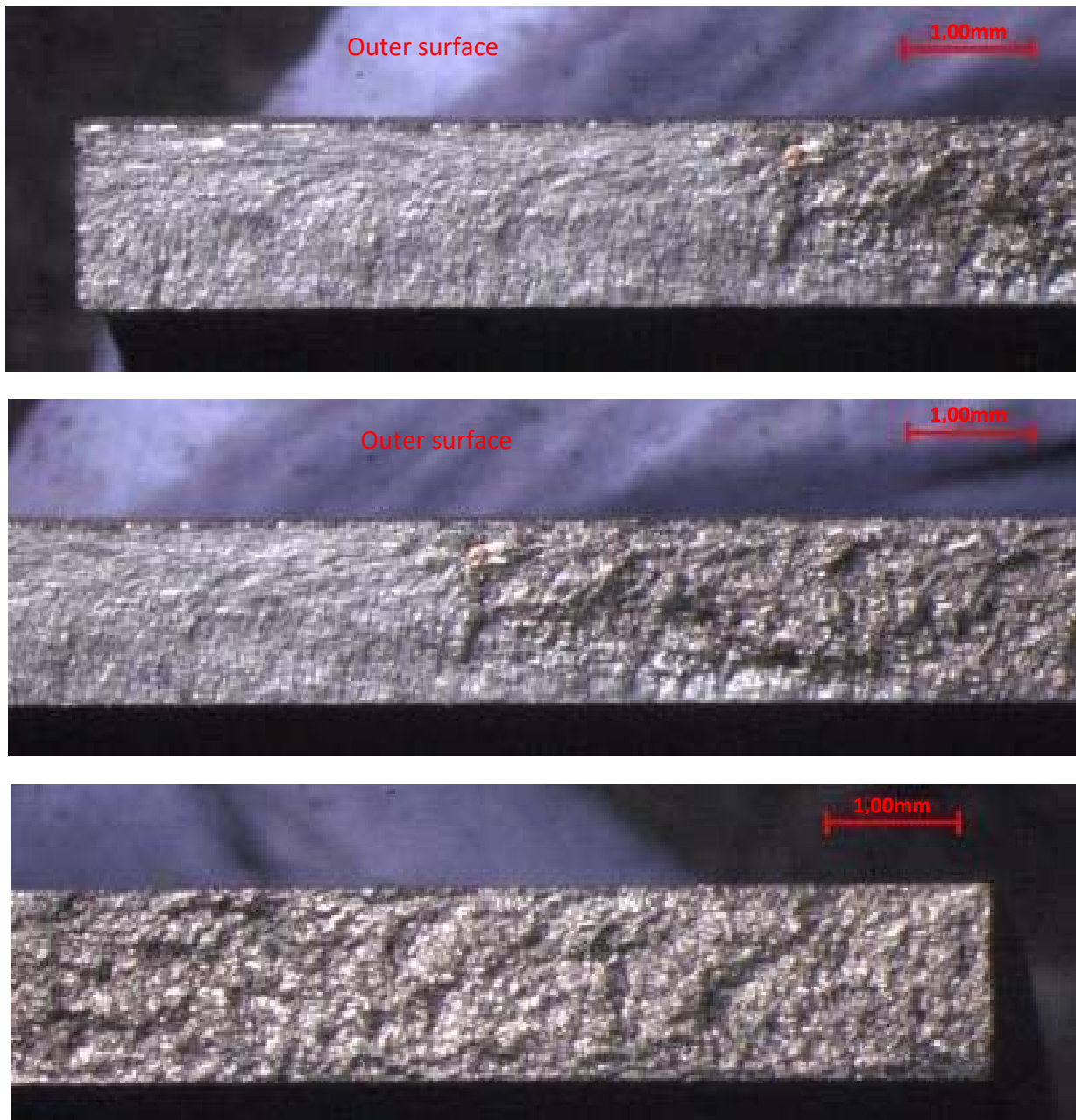


Figure 20: Fractured area of the specimen with fatigue at austenitic phase. The top image focuses on the area of the fatigue crack propagation. In the middle and bottom images, the change in morphology is observed due to brittle fracture.

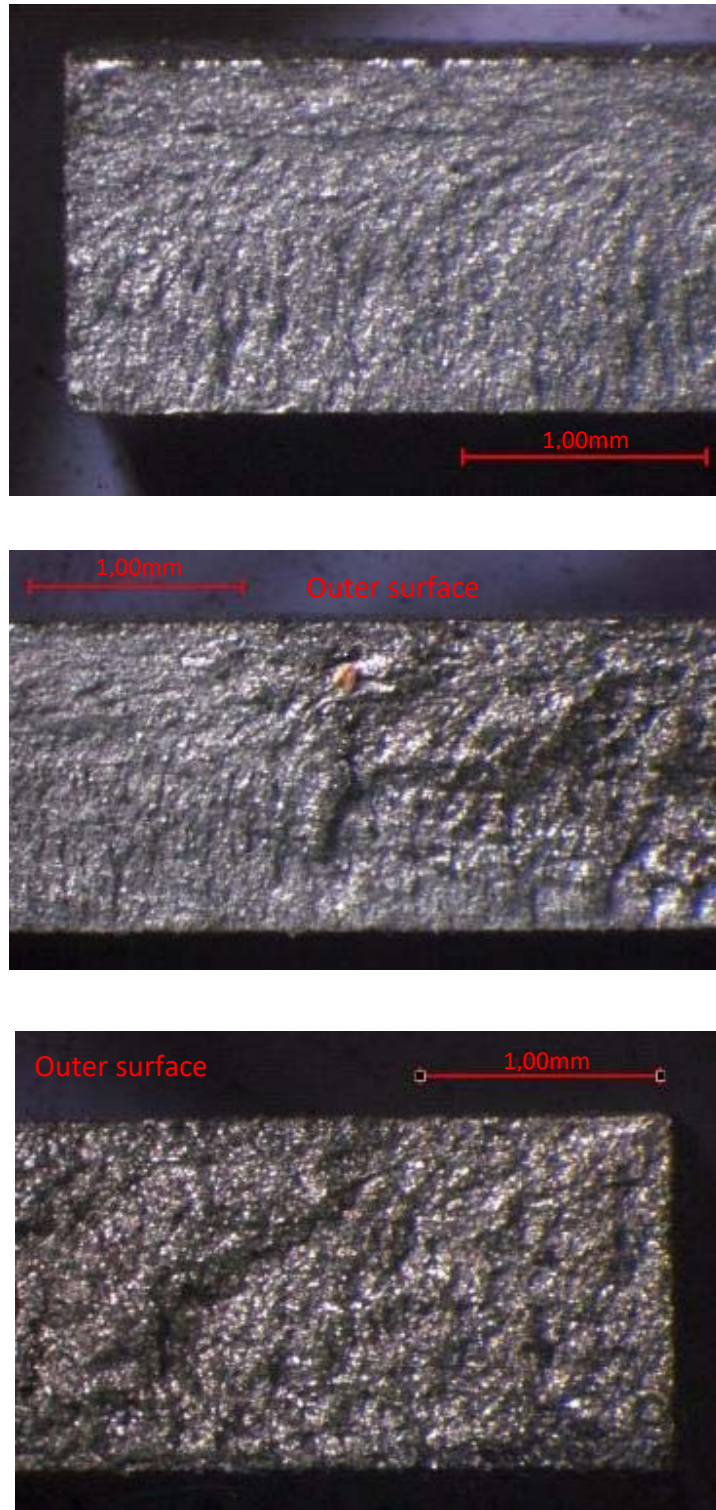


Figure 21: Fractured area of the specimen with fatigue at austenitic phase. Higher magnification images focusing on areas of interest.

6.2.2 Scanning electron microscopy

The images of Figure 22 were taken through Scanning electron microscopy and illustrate the fractured surface of the sample, resulting from a fatigue experiment at 260 °C (austenitic phase) after 271.000 cycles.

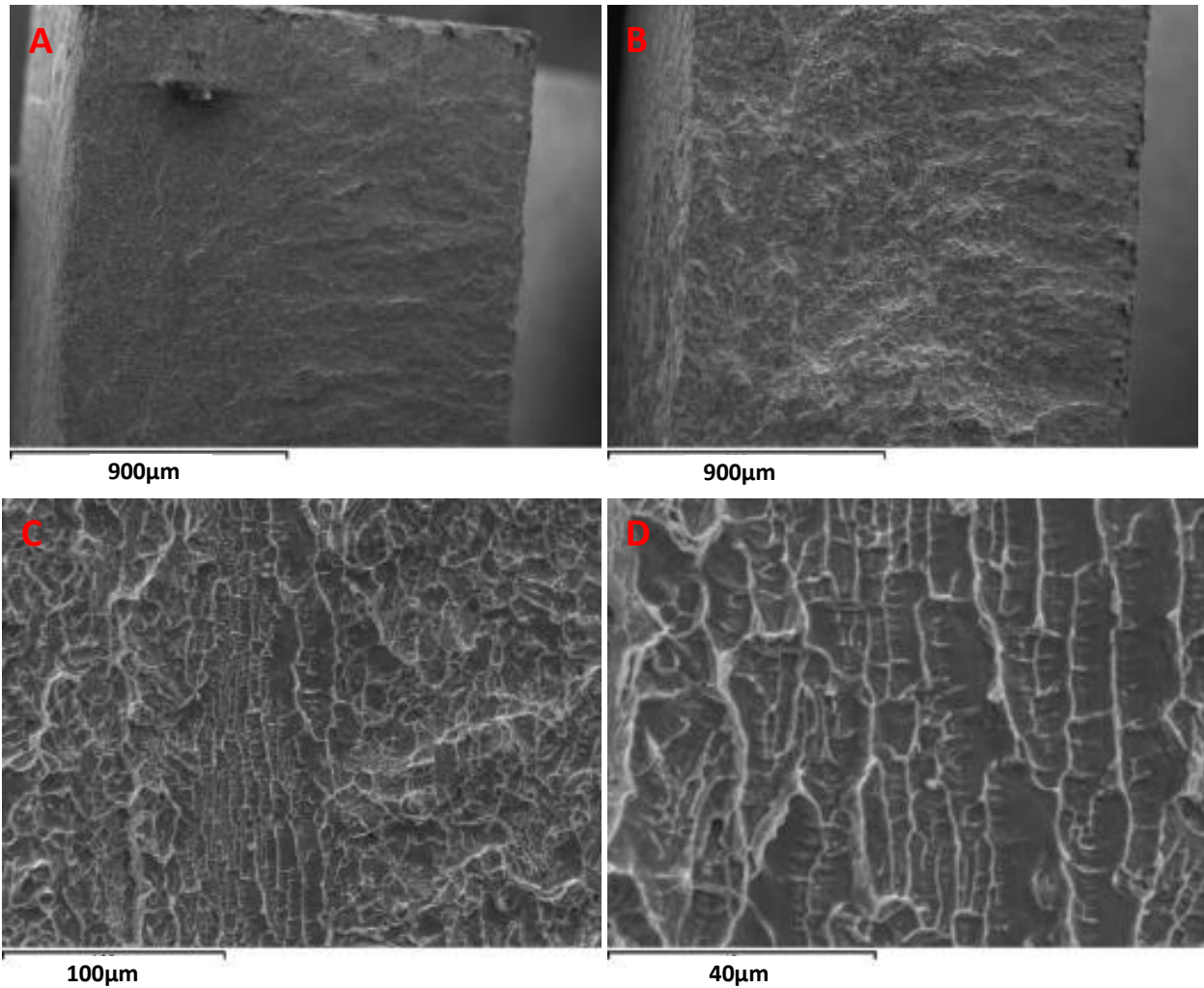


Figure 22: Scanning electron images of the NiTiHf c-ring fractured surface in the austenite phase.

In the image (B) the macroscopic waveform striations of fatigue can be observed. In the image (A), the other side of the fractured surface can be observed in which signs of brittle fracture appear. In the fractographs (C) and (D), evidence of transgranular cracking appear.

6.2.3 Optical microscopy

The images of Figure 23 were taken through optical microscopy and illustrate the granular microstructure of the sample on the fractured surface.

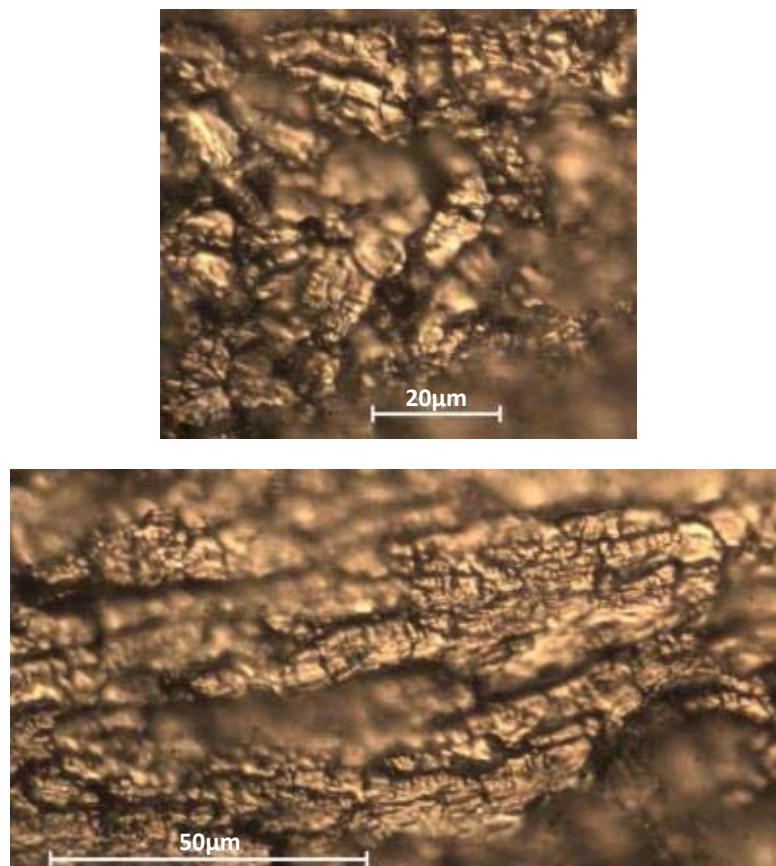


Figure 23: Microstructure of the material on the fractured surface.

6.3 Failure mechanism

The failure mechanism of the samples both in the martensitic (at ambient temperature) and in the austenitic (at 260°C) state under the applied stress of 363 MPa seems to be of mixed mode, with the presence of transgranular cracks occupying most of the fractured surface but with several areas suffering from intergranular failure. Macroscopic brittle waveform striations (river patterns and cleavage steps) are evident in both cases [6], [9].

The waveform striations change orientation due to the transition from the region of the compressive stress (inner surface) to the tensile stress (outer), and from radial become axial. In both cases the fracture gives a brittle morphology and crack often propagates by cleavage – breaking of atomic bonds along specific crystallographic planes (cleavage planes) [8].

7. COMBINED CORROSION AND FATIGUE EXPERIMENTS

In this section the combined corrosion and fatigue performance of the NiTiHf is investigated with respect to the passive layer formed on its surface. This passivation offers high corrosion stability, but it is influenced by the surface interactions with the environment during corrosion exposure and thus indirectly from phase transitions (austenite to martensite and vice-versa). As reported in the literature, during the phase transformation the macroscopic deformation breaks the integrity of the surface oxide, resulting in a change in the corrosive resistance of the transformed and non-transformed regions [12].

In the experiments that follow, the effect of corrosion on the fatigue performance was examined. For this purpose, three experiments were performed. In its basic form the experiment repeats the fatigue test with 600N applied force (at 363 MPa) at ambient temperature and a frequency of 40Hz, with the only difference that the sample is placed in 3.5 wt % NaCl aqueous solution. The adjustment made in the experimental setup to facilitate this kind of test is shown in Figure 24.

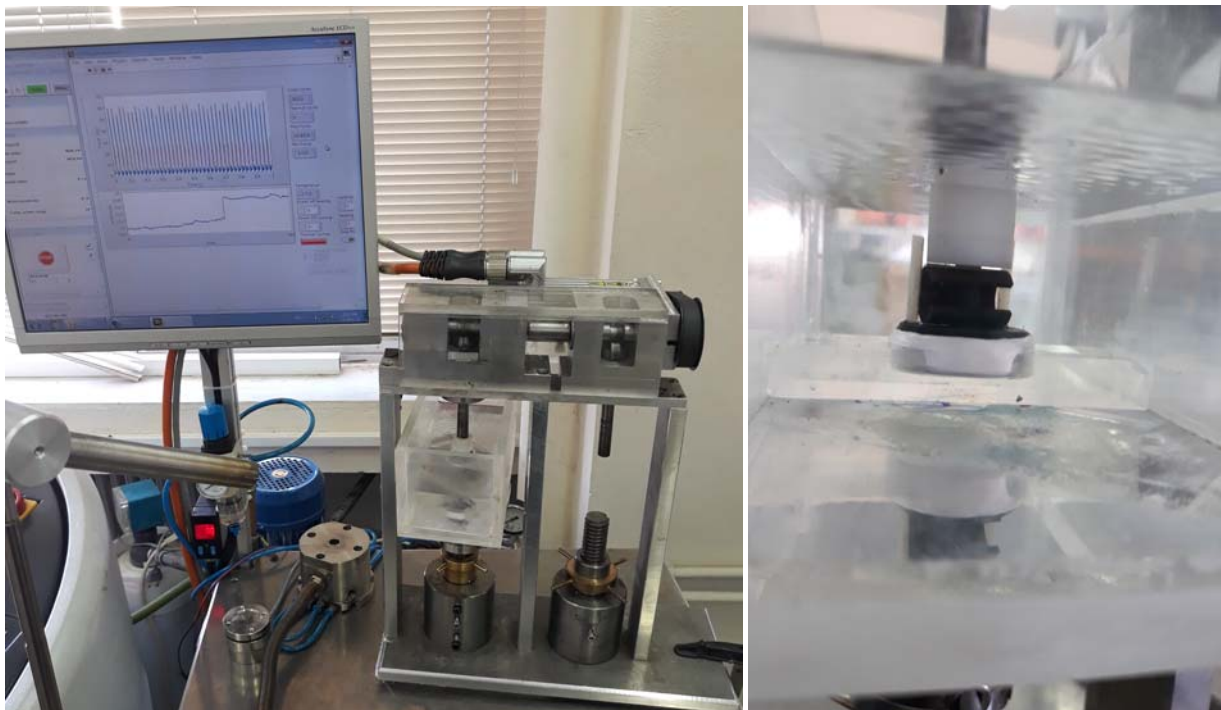


Figure 24: Corrosion – fatigue experiment in 3.5 wt % NaCl aqueous solution.

7.1 1st combined corrosion and fatigue experiment without electrochemical measurements

This experiment was conducted only for the study of resistance to fatigue in a corrosive environment.



Before the start of the first experiment, the weight of the sample was measured at 6,0155 gr and the pH of the 3.5 wt % NaCl aqueous solution was equal to 6,05.

The fatigue life of the sample was 172.800 cycles. as can be read from the following force - time Diagram 19.

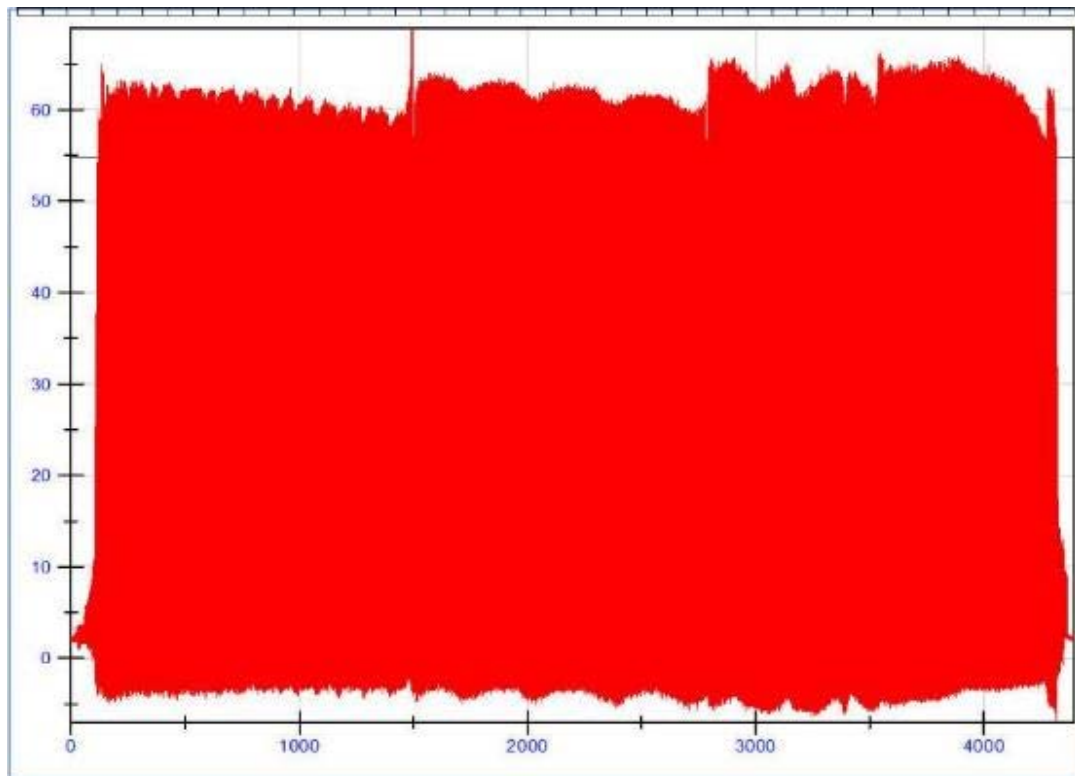


Diagram 19: Observation of individual loading cycles of combined corrosion and fatigue experiment.

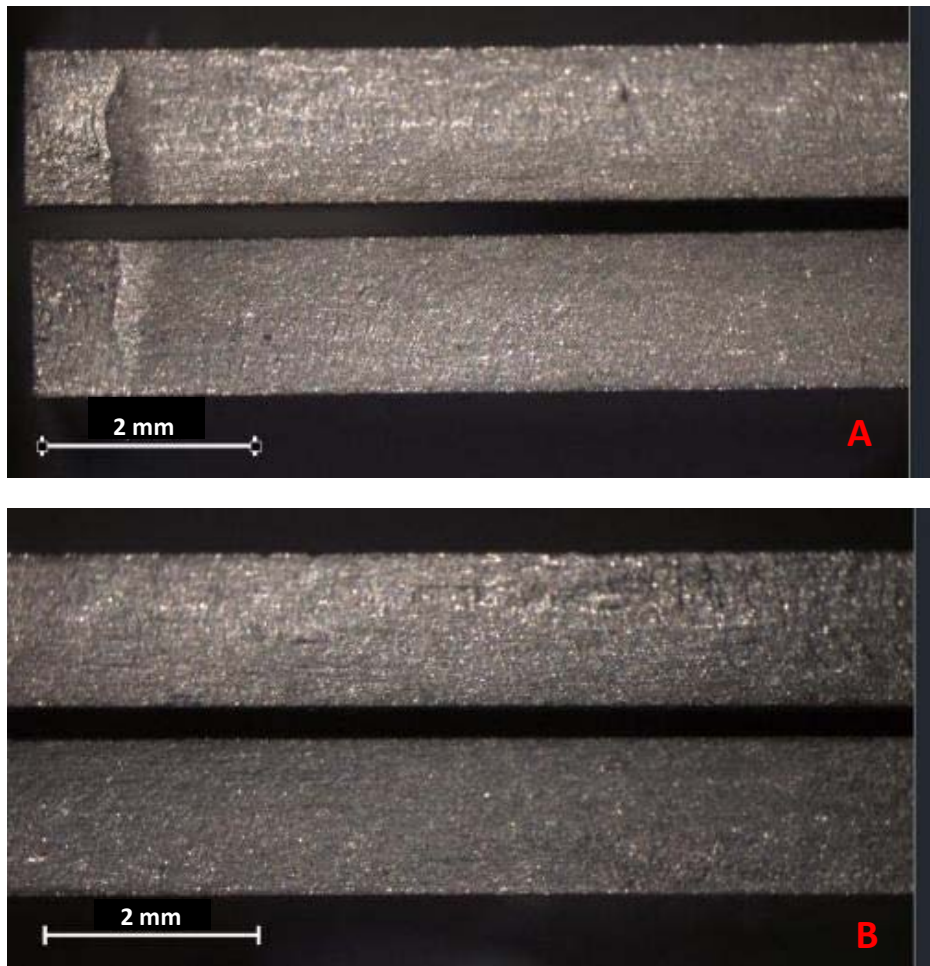
After the experiment was completed the weight of the sample was again measured and found to be 6.0167 gr, while the pH of the solution 7,18. This change is an indication of corrosion due to the interaction of the metal with the solution.

7.2 Fractographic analysis on the sample of the 1st combined corrosion and fatigue experiment

The fractured surfaces are illustrated in Figures 25 and 26.



Figure 25: Fractured surface of the specimen of the 1st combined corrosion and fatigue experiment. Right image: beginning of the crack. Left image: end of the crack.



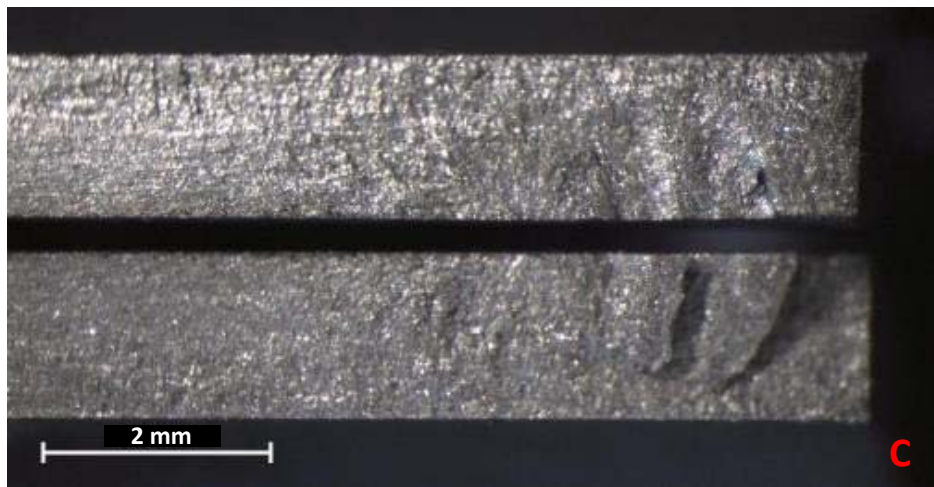
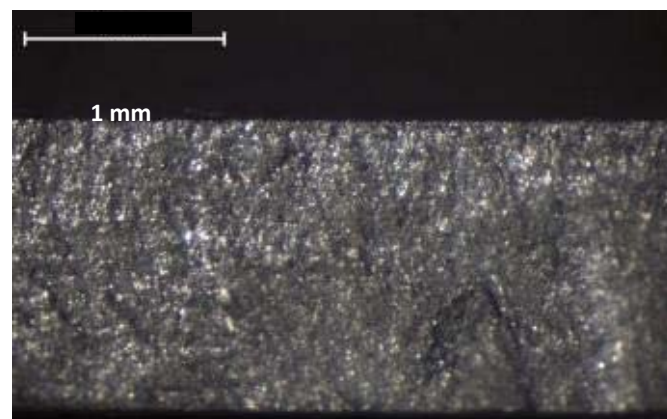
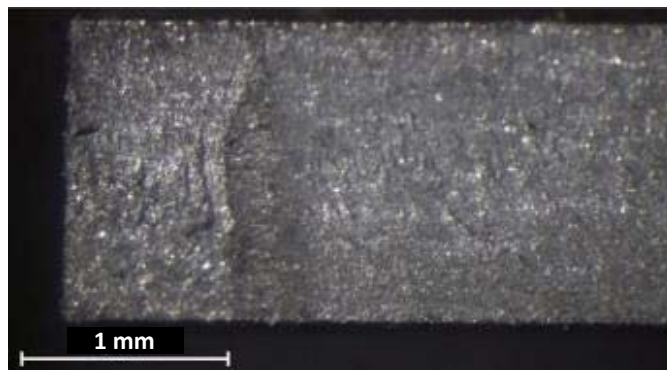


Figure 26: Fracture surface of the specimen of the 1st combined corrosion and fatigue experiment.

Image (A) of Figure 26 shows the beginning of the crack in the two segments resulting from the fracture of the sample. The waveform striations of fatigue are also visible. Image (B) shows the crack propagation, while image (C) shows the final brittle fracture. Figure 27 shows higher magnification images focusing on areas of interest.



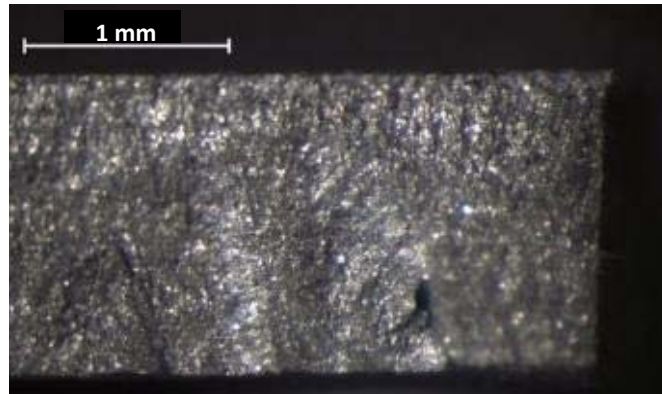


Figure 27: Fractured area of the specimen at higher magnification.

7.3 Study of the corrosion mechanism of an electrochemically cleaned specimen.

7.3.1 *In-situ detection of open circuit potential, Potentiodynamic polarization, Electrochemical impedance spectroscopy*

To detect the open-circuit potential (OCP) of the parent material itself, the oxide layer formed on the surface and contributes to the material passivation, had to be removed. Especially after the heat treatment, the oxide layer became thicker and more stable, as can be assumed by the change of the color (darker), as Figure 28 shows.

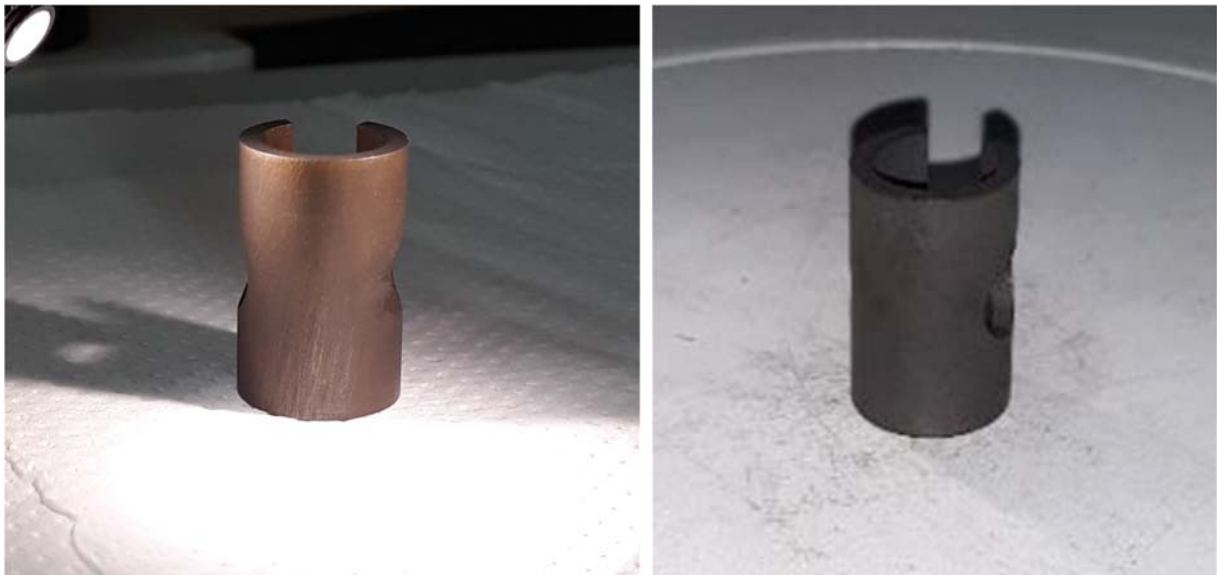


Figure 28: Change of the sample color after heat treatment (right) attributed to surface oxidation.

The removal of the outer oxide layer was performed by electrochemical cleaning to avoid the introduction of mechanical stresses which could lead to the formation of residual stresses,

microcracks and phase transformation. The electrochemical cleaning, as shown in Figure 29, was performed at a voltage of 10 V for 30 minutes with solution 80 v/v % acetic acid and 20 v/v % perchloric acid.



Figure 29: Electrochemical cleaning of NiTiHf specimen.

Upon completion of the electrochemical cleaning the parent alloy was revealed, having a bright metallic color as shown in Figure 30.



Figure 30: The specimen parent alloy which was revealed from electrochemical cleaning.

However, based on the reduced fatigue life of this specimen, there is a high possibility that the electrochemical cleaning may cause aggressive corrosion that degrades the mechanical strength. This assumption is confirmed by the fractographies that follow.



Proceeding to measure the OCP, the specimen was immersed (without yet applying any force on it) to 3.5% w/w NaCl aqueous solution and appropriate connections with the electrochemical corrosion device was made. Special attention was given to avoid short circuits and galvanization during the experiments. The container with the specimen as shown in the figure 28 was placed in the fatigue device so that in the next experiment the electrochemical parameters can be combined with the fatigue data.

To investigate potentiodynamic behavior in the particular corrosive environment the range of potential set, started at -1000 mV and reached up to 1000 mV, with a scan rate 2mV/sec, adjusting as a time interval between successive measurements the value of 0.0525 sec and having a step amplitude of 0.125 mV.

The measurement showed that OCP in unloaded and cleaned specimen starts at -530mV and shows to stabilize approximately at -426mV, as can be read from the Diagram 21.

The potentiodynamic curve in the unloaded state is given in the Diagram 20 below. By the non-stable current response to the imposition of the potential in the material, it can be concluded that multiple stoichiometric changes have been caused by the cleaning procedure of the specimen that led to continuous collapse and regeneration of the oxide layer.

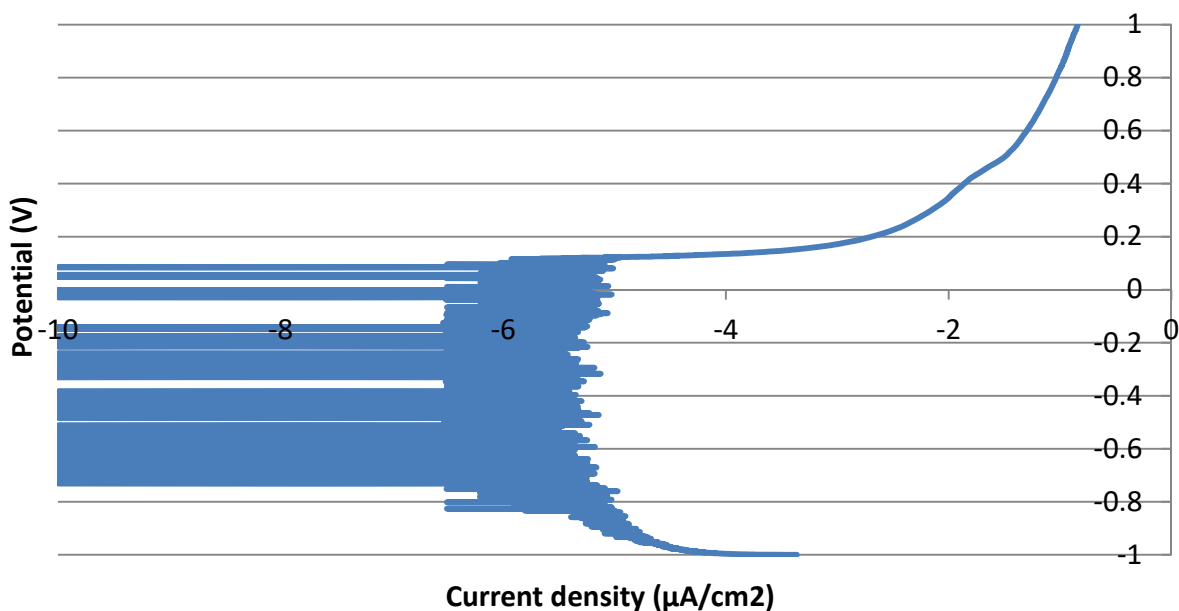


Diagram 20: Potentiodynamic curve in the unloaded state for the cleaned specimen.

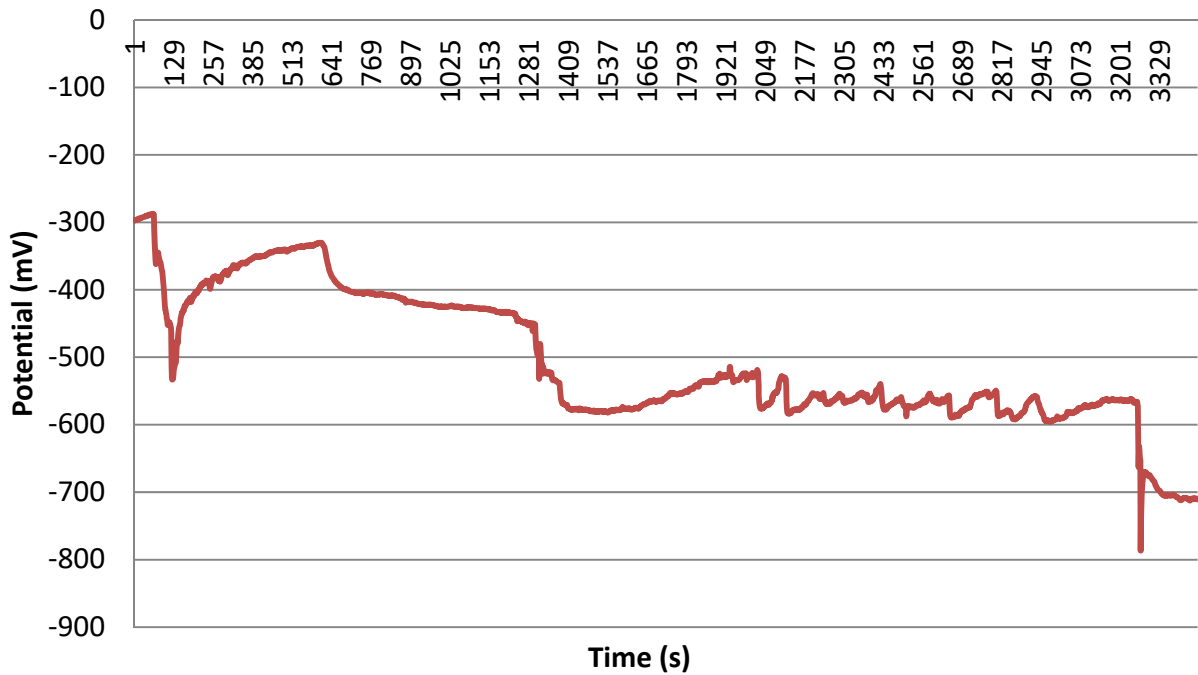


Diagram 21: Detection of open circuit potential and combined corrosion and fatigue test of the cleaned specimen.

In the first part of the waveform the OCP diagram was measured without applying any mechanical load on the specimen. This potential after about 20 minutes stabilizes at -426 mV. By applying the cyclic load, the potential changes to -571mV and is maintained with some fluctuations at this level until fracture. As mechanical stress is applied on the specimen, its potential is increased (to the minus), which can be attributed to the change of the thickness of the surface oxide layer or even the formation of micro-cracks until it is stabilized at a potential value of about -530mV. At the time of fracture, the potential drops to -786 mV due to the sudden revelation of a large surface of parent material.



7.4 2nd experiment of combined corrosion and fatigue test of the electrochemically cleaned specimen

The combination of fatigue and corrosion devices for the next experiment is shown in the Figure 31.

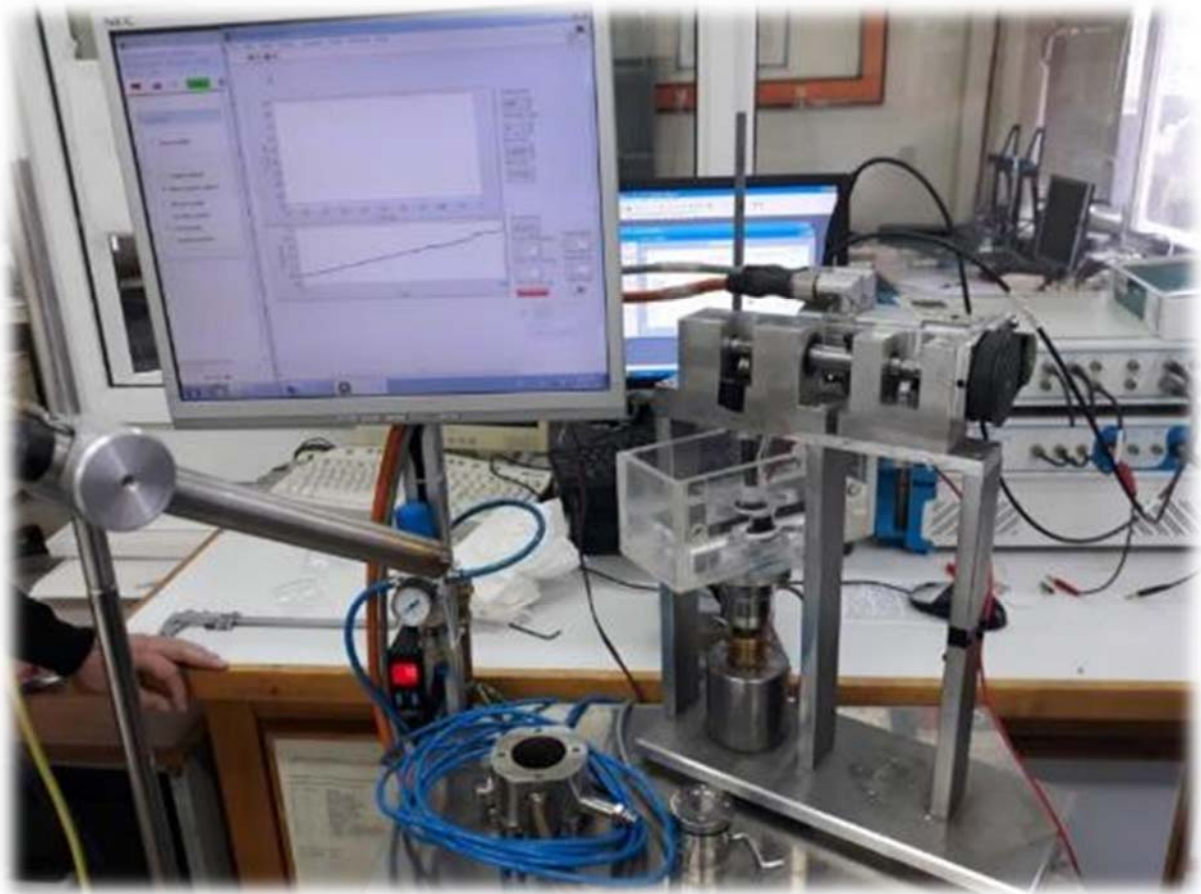


Figure 31: Experimental setup for the investigation of the corrosion-fatigue.

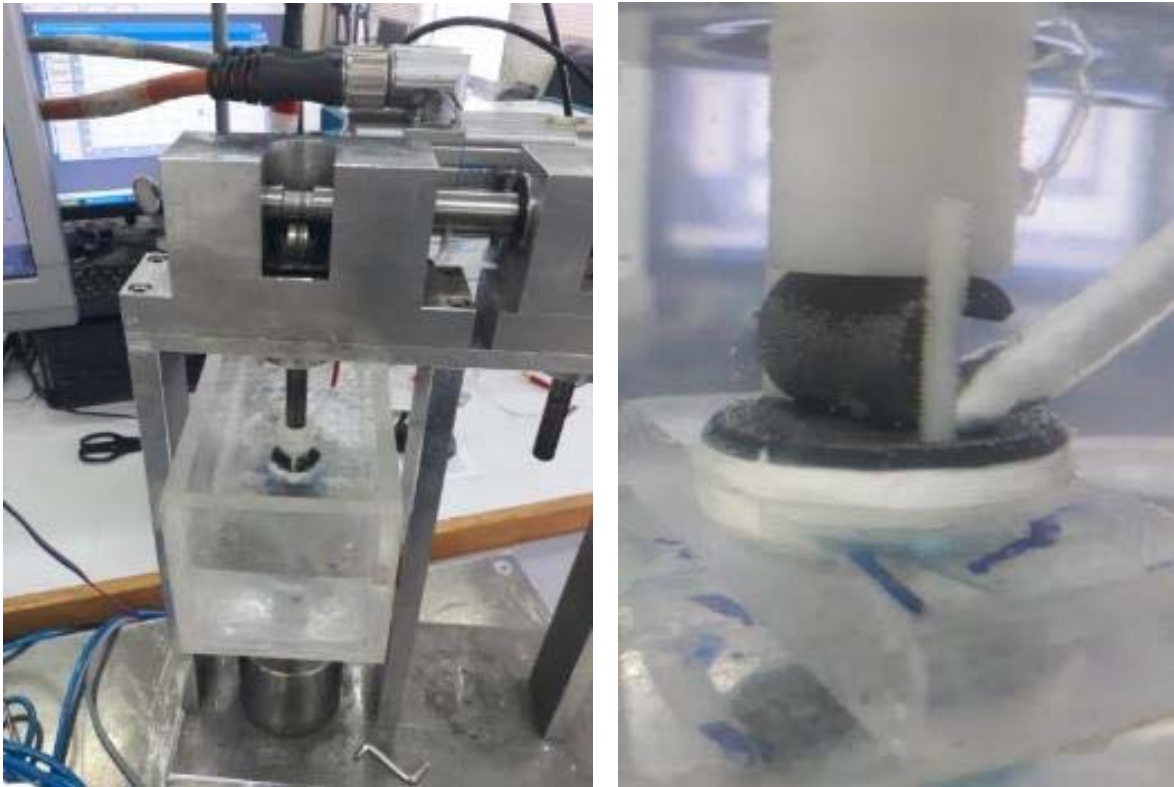


Figure 32: Electrical connection of the specimen and its holder in the fatigue device.

The piston exerted an alternating force between 0 and 600N at a frequency of 40 Hz.

Below is given the time force Diagram 22 recorded during the experiment.

Life span at fatigue was measured at 65.000 cycles.

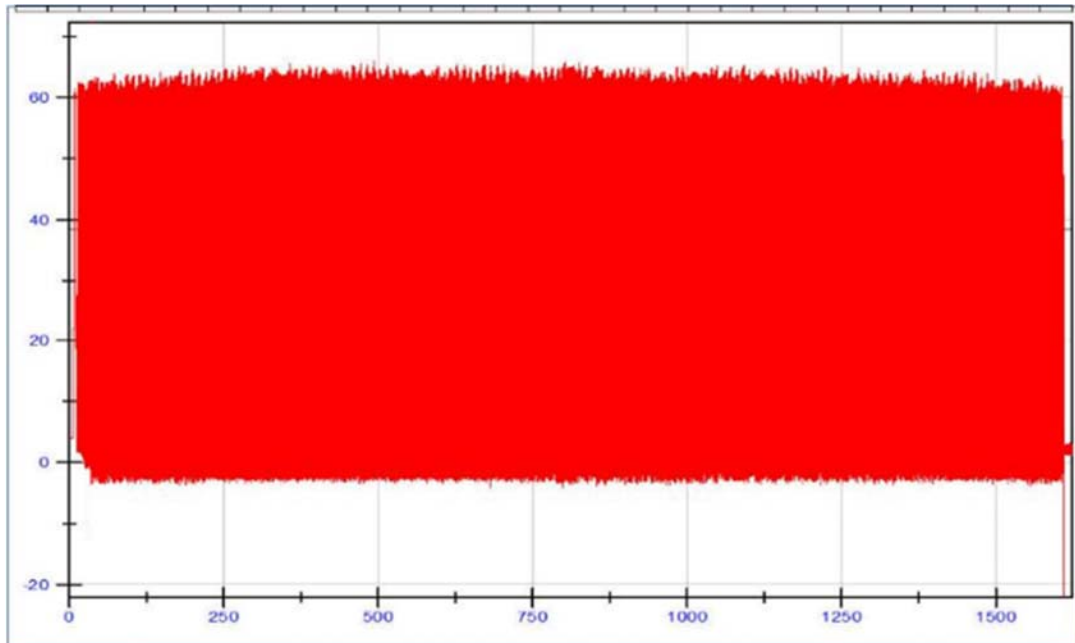


Diagram 22: Waveform of loading cycles for the cleaned specimen until fracture.

7.5 Study of the corrosion mechanism on the electrochemically uncleaned specimen

A corresponding experiment was carried out on a sample which was not subjected to electrochemical cleaning and was examined directly after the heat treatment. To investigate potentiodynamic behavior in the particular corrosive environment the range of potential set, started at -1000 mV and reached up to 1000 mV, with a scan rate 2mV/sec, adjusting as a time interval between successive measurements the value of 0.0525 sec and having a step amplitude of 0.125 mV.

The measurement showed that OCP in an unloaded specimen is approximately -200mV as can be observed in Diagram 24. The potentiodynamic curve in the unloaded state is given in the Diagram 23. From this curve, due to the fact that it was carried out after the fracture of the specimen, a passivation is observed at -456mV.

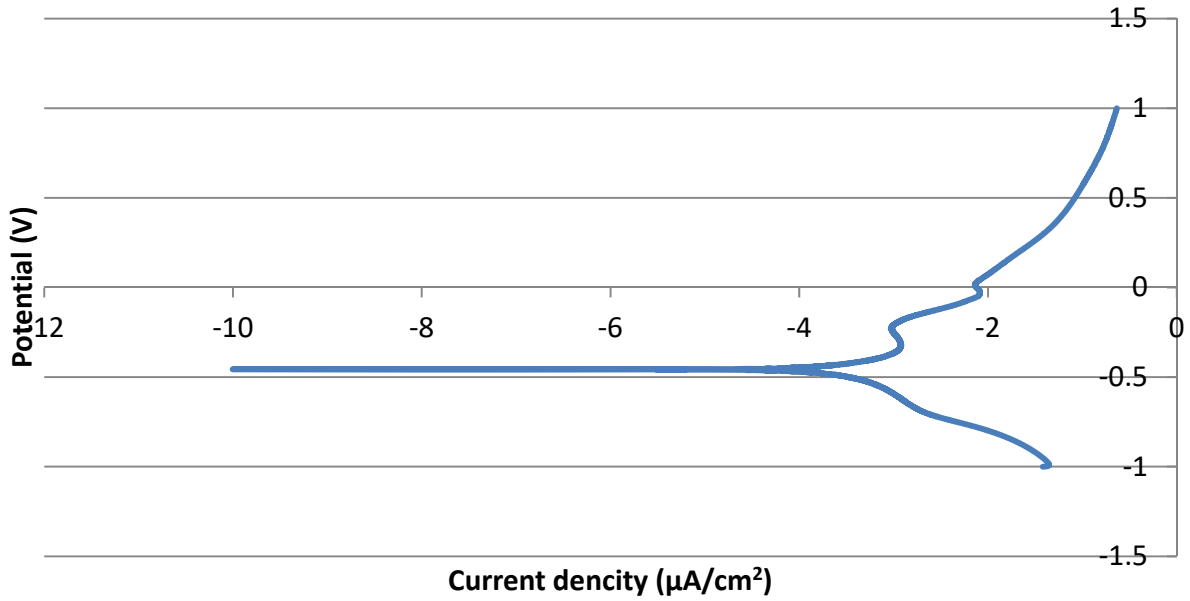


Diagram 23: Potentiodynamic curve in the unloaded state for the uncleaned specimen.

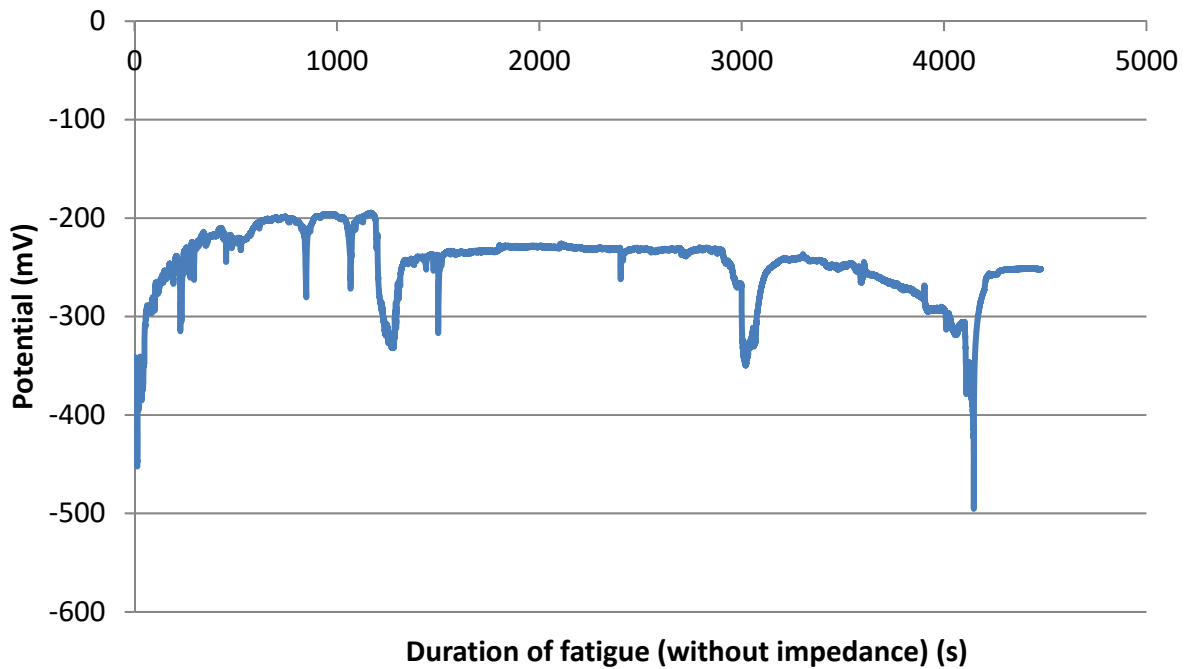


Diagram 24: Detection of open circuit potential and combined corrosion and fatigue test of uncleaned specimen.



Electrochemical impedance spectroscopy (EIS)

The OCP during fatigue is shown in the Diagram 25.

The measurements of impedance after the first 20 minutes were repeated every 5 minutes (as well as fatigue in the meantime). The overall picture of the impedance measurements is shown in the Diagram 25.

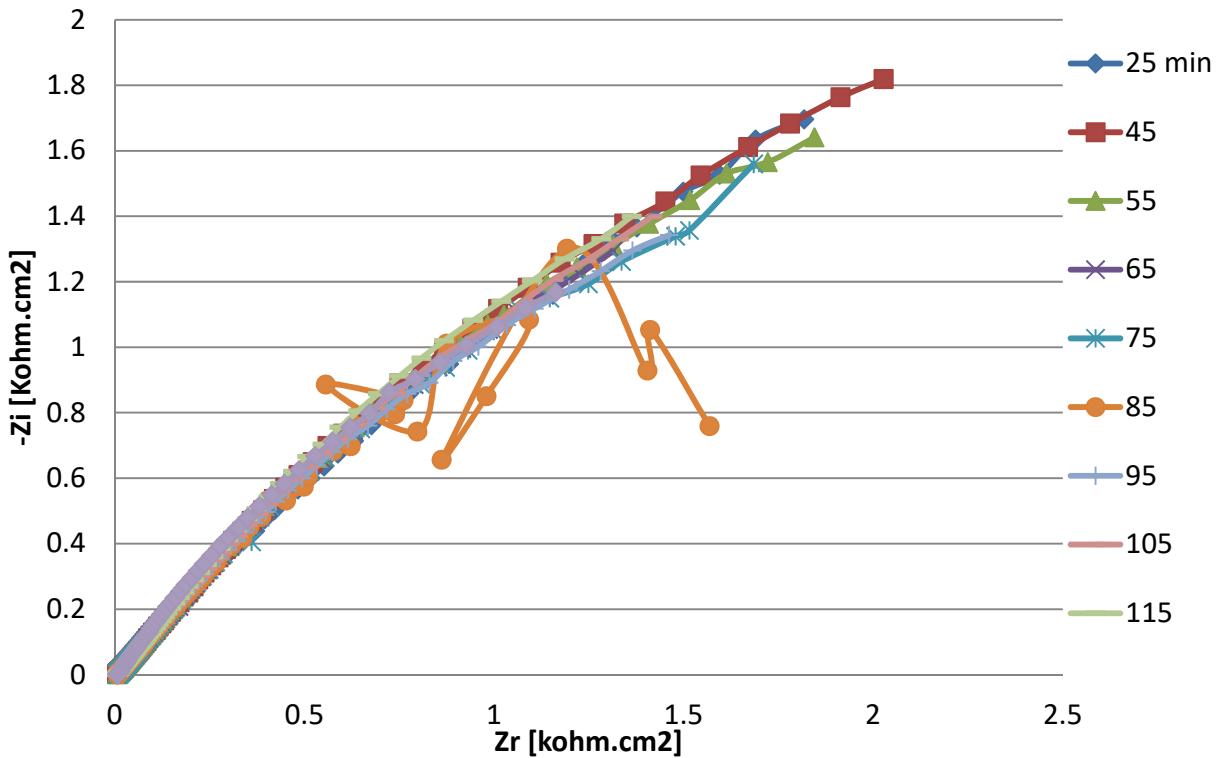


Diagram 25: Electrochemical impedance spectroscopy for the uncleaned specimen in unload state during fatigue experiment.

The impedance after the fracture of the specimens is given in Diagram 26.

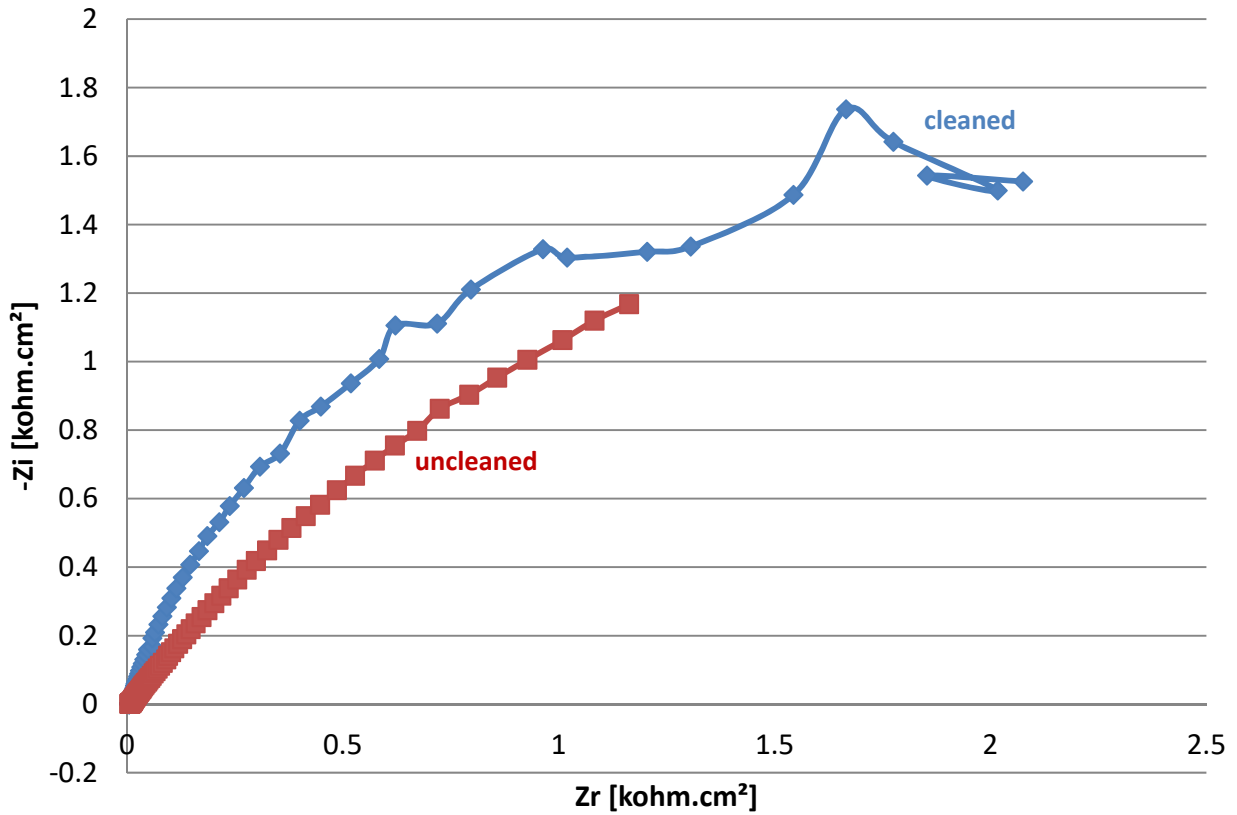


Diagram 26: Impedance comparison of the specimens after fracture.

The sequence of measurements for the corrosion data is given in the table1.

	Duration (min)	Force / frequency (Kgr/Hz)	Electrochemical measurements
1	20	0	OCP
2	5	0	EIS
3	5	60/40	OCP
4	5	0	EIS
5	5	60/40	OCP
6	5	0	EIS
7	5	60/40	OCP
8	5	0	EIS
9	5	60/40	OCP
10	5	0	EIS
11	5	60/40	OCP
12	5	0	EIS
13	5	60/40	OCP
14	5	0	EIS



15	5	60/40	OCP
16	5	0	EIS
17	5	60/40	OCP
18	5	0	EIS
19	5	60/40	OCP
20	5	0	EIS
21	5	60/40	OCP
22	5	0	EIS

Table 1: Sequence of measurements for the corrosion data.

7.6 3rd experiment of combined corrosion and fatigue test without electrochemical cleaning

In the combined corrosion and fatigue test the piston exerted an alternating force between 0 and 600N at a frequency of 40 Hz. The life span was measured to 116.000 cycles.

7.7 Fractographic analysis on 2nd combined corrosion and fatigue experiment

The specimen subjected to electrochemical cleaning and combined corrosion-fatigue, is shown in Figure 33 to visualize its surface condition before and after testing (failed). The specimen failed from the outer surface where the maximum tensile stresses are developing. The two segments of the fractured specimen do not share the same picture, due to the potentiodynamic polarization that one of them suffered after fracture.



Figure 33: Outer surface of the cleaned specimen before and after the corrosion-fatigue experiment.

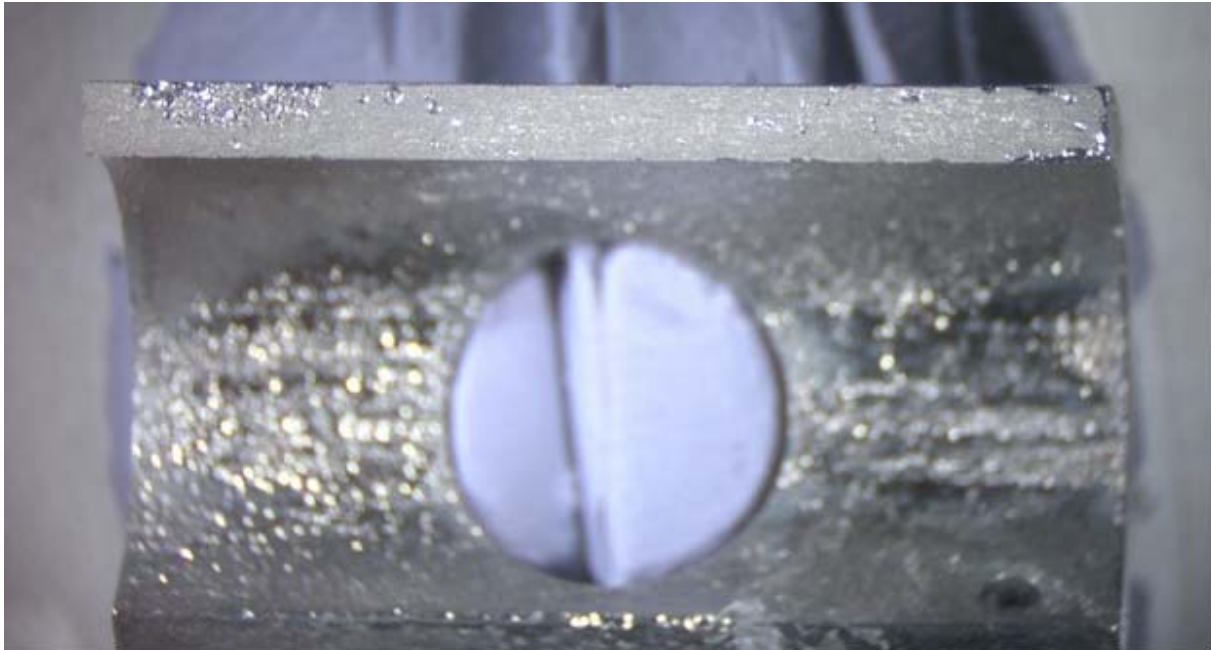


Figure 34: Fractured surface of the electrochemically cleaned specimen after the combined corrosion-fatigue and potentiodynamic polarization test.

The revelation of the parent material after chemical cleaning has caused a strongly anodic behavior on the specimen immediately upon immersion into the NaCl solution. This behavior can be validated by the observation of the fractographic images and the OCP diagram, where the specimen before being subjected to fatigue showed combined surface and pitting corrosion (Figure 35, points B and C) which tended to stabilize by giving an OCP of -426mV after 20 min covering the entire outer surface of the specimen. During the propagation of the fatigue crack there were fluctuations in OCP due to the three parallel phenomena: (i) the increase in stress, (ii) the revelation of new matrix material (new cracks) and (iii) corrosion in the NaCl solution. In areas where microcracks cause increase in stress, corrosion becomes more intense, two such indicative points can be observed in the pitting corrosion developed at points A in the Figures 35 and 36. By specimen fracture and revelation a large surface of parent material, corrosion was activated on the new surfaces raising the OCP to -786mV . Corrosion at the fracture surface was therefore more intense than the corrosion of the surface of the specimen upon immersion, this resulted in pitting corrosion on the surface during the time the specimen remained in the NaCl solution to execute the potentiodynamic polarization experiment.

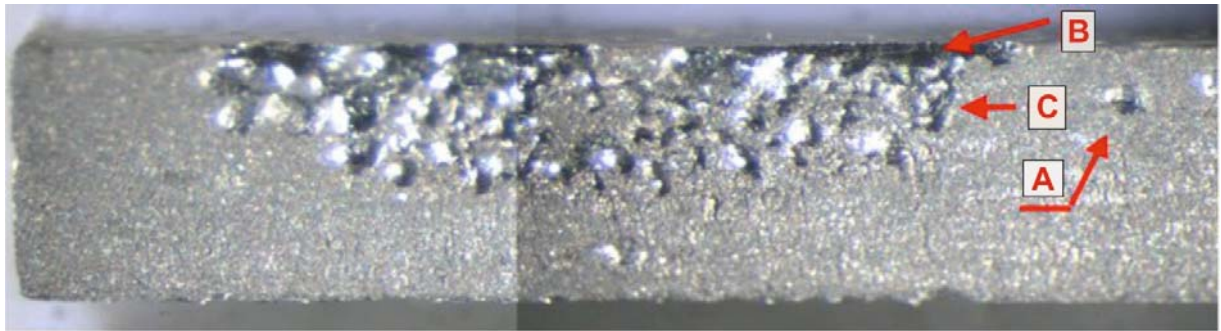


Figure 35: Crack start area where intense pitting corrosion can be observed in two directions.

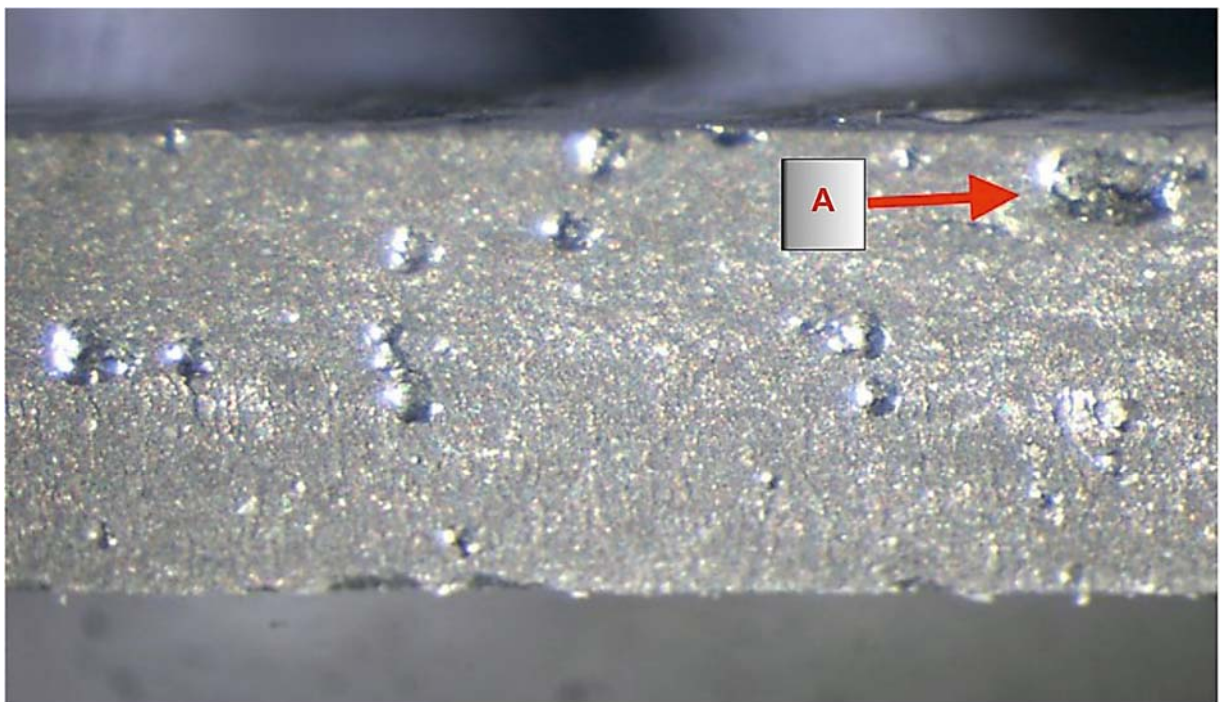


Figure 36: Surface of brittle fracture of electrochemically cleaned specimen, where pitting corrosion is evident.

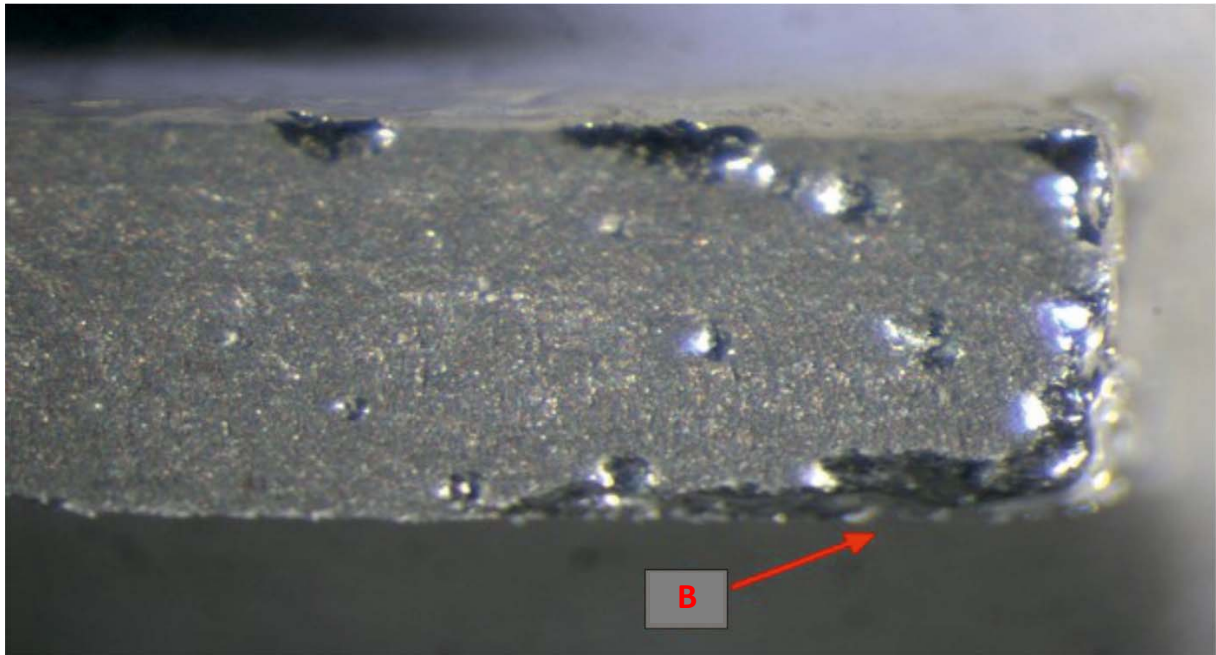


Figure 37: Area of extended surface corrosion of the electrochemically cleaned specimen.

From the second part of the sample that was not subjected to a post potentiodynamic polarization, a more representative picture of the rupture process can be derived as it did not show intense aggressive corrosion on the surface (Figure 38). On the fractured surface shown in Figure 39, the crack initiation site can be observed.

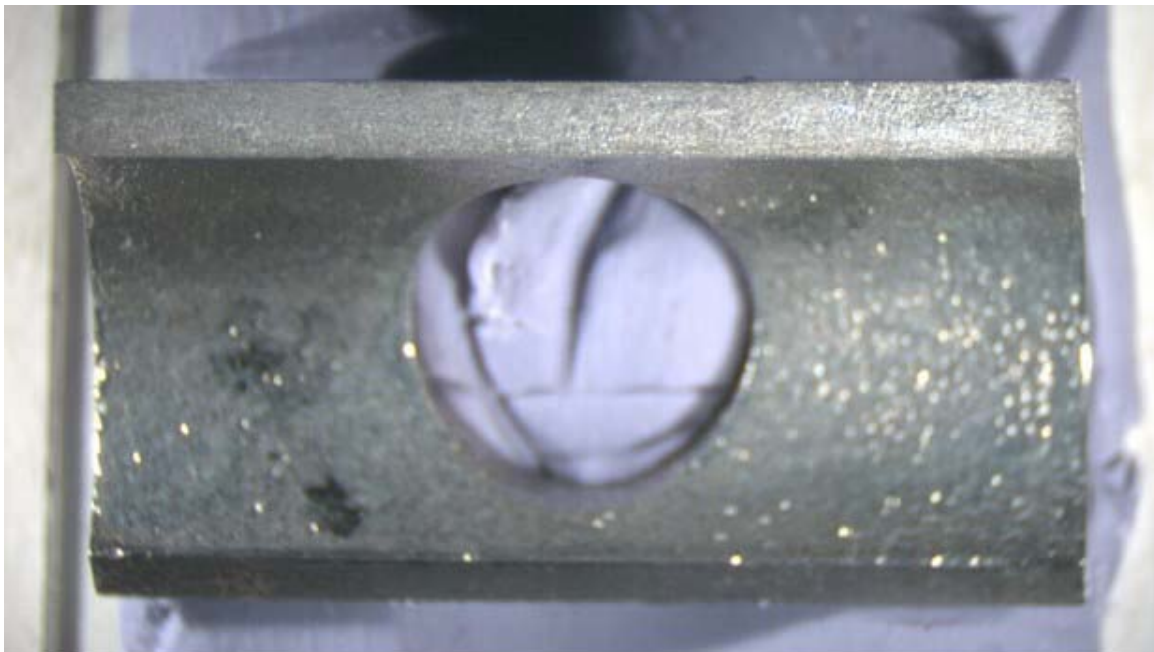


Figure 38: Fracture surface of electrochemically cleaned specimen after fatigue.

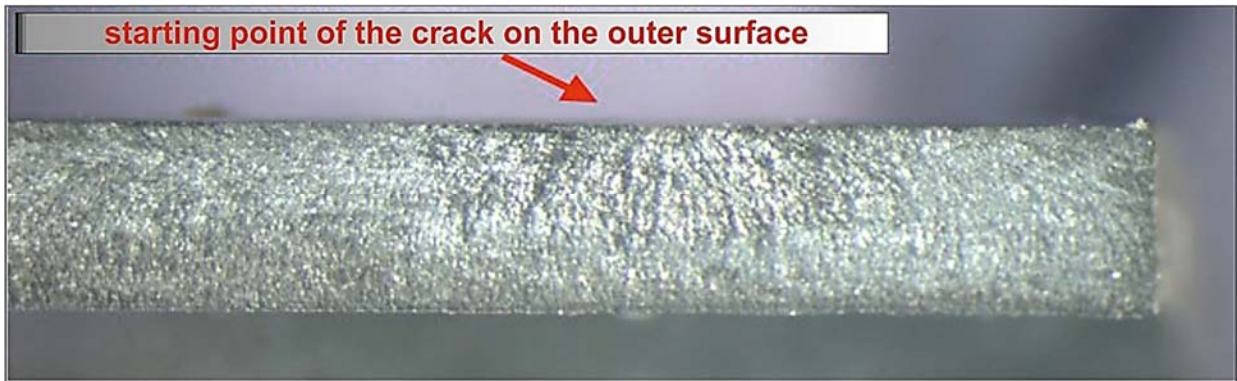
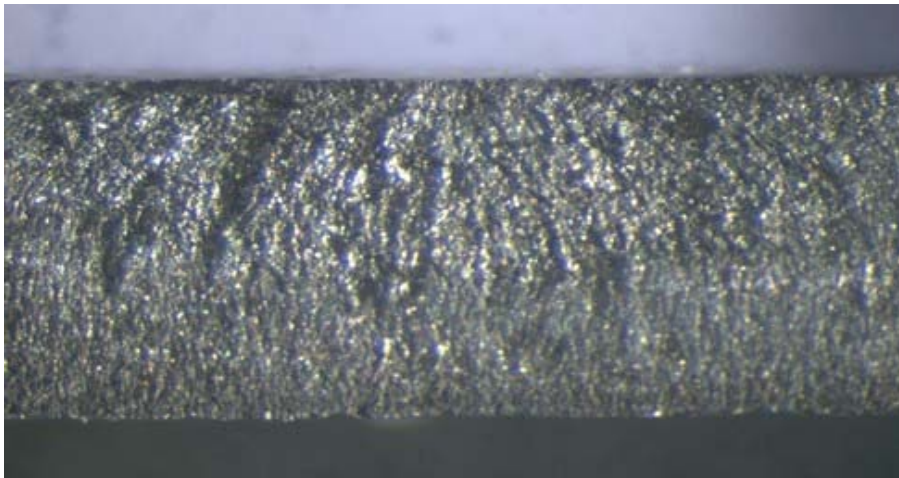


Figure 39: Starting point of the crack in the electrochemically cleaned specimen during combined corrosion-fatigue.

In Figure 40, detailed images of the starting point of the crack and from the crack propagation to the edges of the specimen are presented.



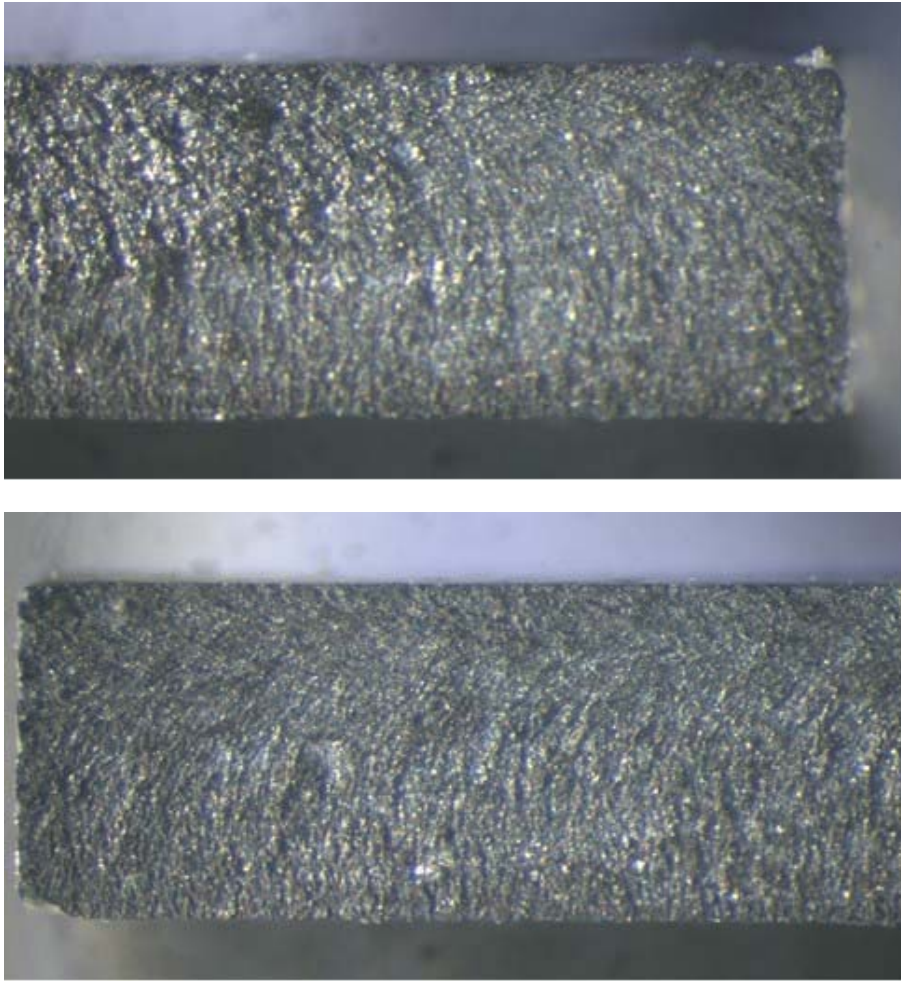


Figure 40: More detailed images of the crack starting point and propagation.

7.8 Fractographic analysis on 3rd combined corrosion and fatigue experiment on uncleaned specimen

The specimen tested under combined corrosion and fatigue without first being subjected to electrochemical cleaning is shown in Figure 41 in the condition before and after failure. The crack initiation happened at the outer surface where the maximum tensile stress appears. The two segments of the fractured specimen share the same picture, irrelevant of the potentiodynamic polarization that was applied in one of them. The open circuit potential remained throughout the experiment at values higher than in the case of the electrochemically cleaned sample, approaching to -230 mV. This can be explained by the presence of the passive layer and even during the crack propagation, part of it is corroded forming a new protective oxide layer before the next crack propagation happens. The most aggressive corrosion is observed in the last stage with the form of



surface pitting in the area where the sharp brittle rupture occurred. This area is where the higher stresses develop.



Figure 41: Outer surface of the uncleaned specimen before and after the combined corrosion and fatigue experiment.

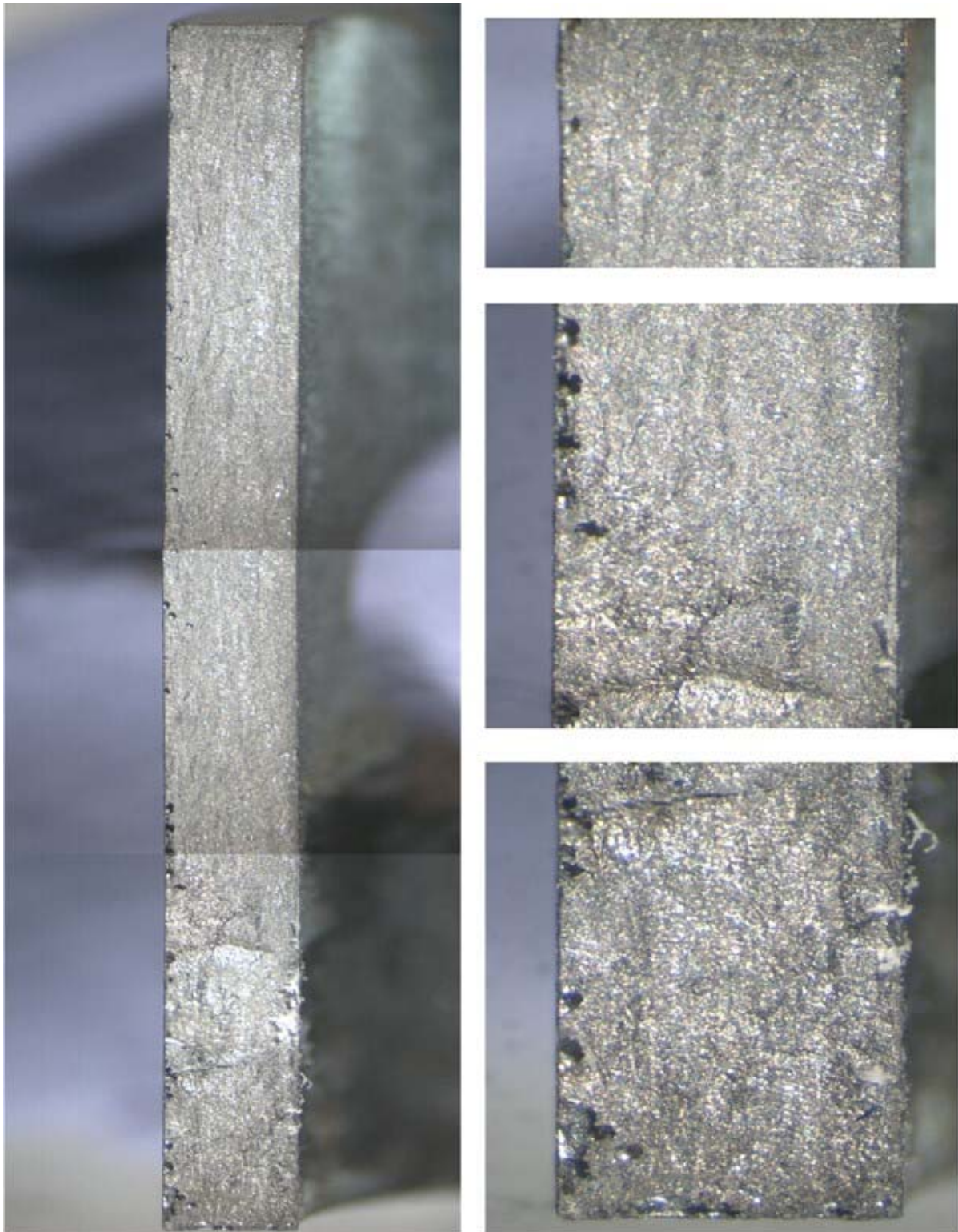


Figure 42: Fractured surface of the uncleaned specimen after the end of the potentiodynamic polarization.

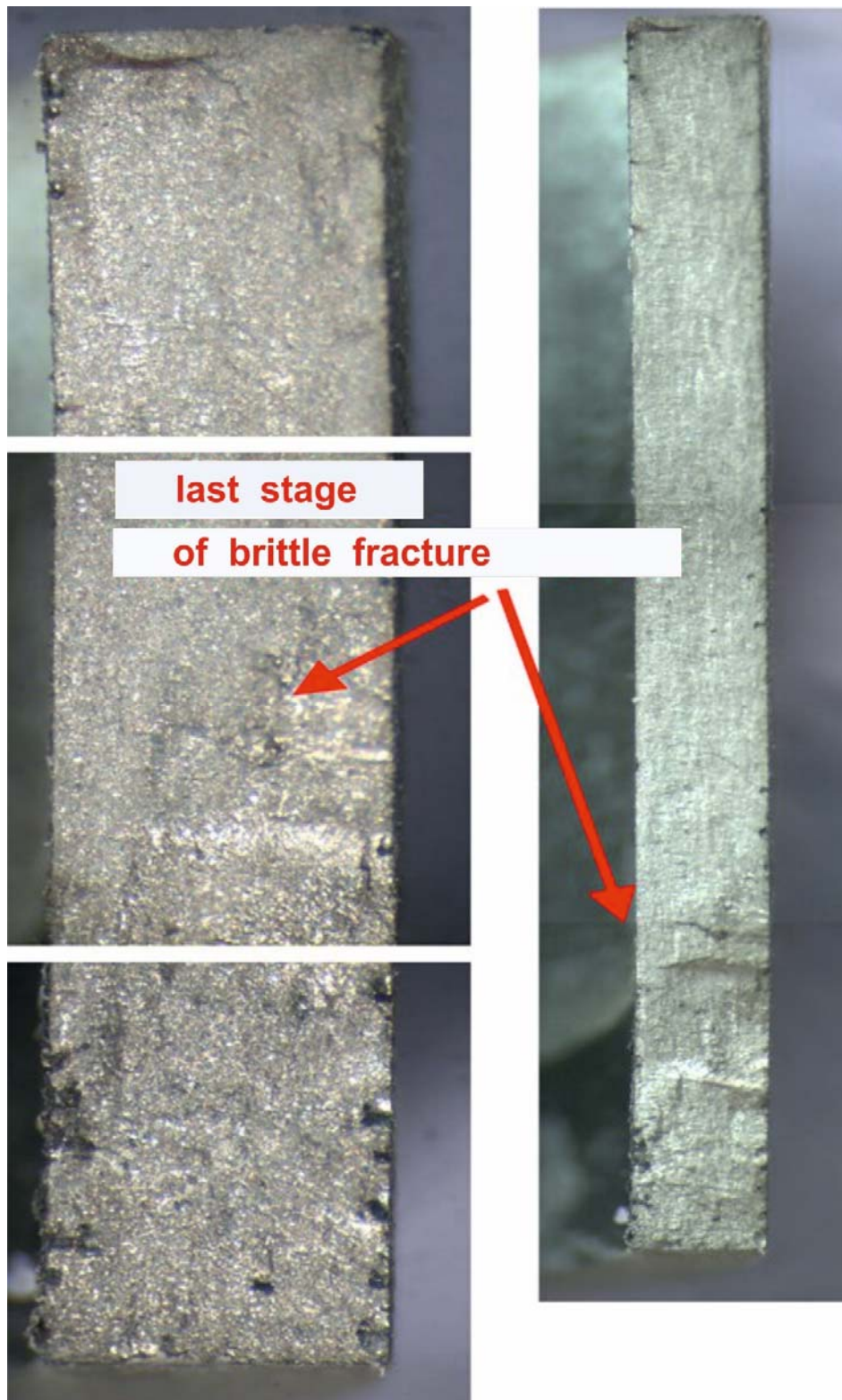


Figure 43: Fractures surface of the uncleaned specimen that which is not subjected to potentiodynamic polarization.



8. SUMMARY

Because of their geometric shape the c-ring type specimens develop a different stress depending on the angle of the surface being examined with respect to the reference axis (Figure 8). This stress was calculated based on an analytical method. By combining the analytical method and performing compression experiments and recording the magnitudes of force and displacement, the stresses and the modulus of elasticity were determined. Compression experiments were performed at ambient temperature where the material was in martensitic phase. After performing 10 loading-unloading cycles at successively increased force it was concluded that at 300 N and 600 N after the first loading, the specimen appears completely detwinned for this load, without the appearance of any hysteresis in the next cycles. Unlike to that trend, at the load of 150 N an additional loading-unloading cycle to complete detwinning was required. The modulus of elasticity during this 1st cycle at 150N was measured at 55GPa and after the detwinning at 300 N and 600 N the modulus of elasticity was increased, reaching the value of 63 GPa. Even if the specimen shows the behavior of detwinned material, for a given load value, this behavior is inverted when the load is increased and a detwinning stress develops in a new area of the specimen. In this fashion, the modulus of elasticity tends to drop towards 55 GPa. At the load of 600 N the specimen showed a fully elastic behaviour after the first loading cycle but as the fatigue experiment progressed the accumulation of imperfections mainly in the area of maximum stress led to hardening of the area and changing the stress field imposing also new areas to detwin. By performing experiments with temperature variation under constant displacement and recording the force, force-temperature curves were produced for various preload values from which equations were extracted to calculate the phase transformation temperatures according to the applied stress. The transformation temperature values of the specimen after heat treatment are higher than those resulting from DSC in the "As Received" specimen referring to the unloaded state and after having them stabilized. After forty cycles of phase transformation the sample was again subjected to compressive stress and again stress - displacement and modulus of elasticity - displacement curves were created. The results show that the modulus of elasticity remains stable but after three mechanical cycles the specimen still had a small hysteresis. This can be attributed first to the detwinning of the material during its cooling with simultaneous stress application, which generally limits the occurrence of twinning, but also to the accumulation of imperfections like dislocations, micro-cracks and other defects [6] that prevent the movement of the martensitic variants boundaries and as a result the remaining deformation decreases per cycle, retained for a larger number of cycles.

From the fatigue experiments it was observed that the specimen in austenitic phase performed at 260 C exhibits a longer life span than in martensitic phase (271.000 cycles versus 195.000 cycles, respectively). The specimens subjected to fatigue in a corrosive environment showed a shorter life span depending on the experimental details and duration of corrosion. The specimen in martensitic phase that was subjected to fatigue in NaCl solution without prior electrochemical cleaning, and without performing on it any OCP and EIS measurements, showed good fatigue life span (172.800 cycles) close to that of the specimen that was tested in a corrosion-free environment. The specimen



that has remained longer in the corrosive environment for the parallel execution of EIS and OCP showed a much shorter lifespan (118.000 cycles). Finally, the electrochemically cleaned specimen lost the protective oxide layer and probably exhibited degradation of its structure on the surface prior to corrosion-fatigue testing. This fact has led to the rapid appearance of the initial crack that propagated fast and led to a fatigue life of 65.000 cycles.

In the fractographic analysis, typical waveform striations were observed in all specimens, facing a change of orientation due to the transition from the region of the compressive stress at the inner surface to the tensile stress at the outer. In both the austenitic and martensitic states of the material (at 260°C and room temperature, respectively) the fracture features a brittle morphology. The failure mechanism in both martensitic and austenitic phase with the applied stress of 363 MPa is of mixed mode, with transgranular cracking being more dominant.

The specimens facing a collapse of the protective surface layer presented a strong anodic behavior, which in the electrochemically cleaned specimen led to a premature failure through an accelerated crack propagation.

The application of stress at 363 MPa, increased significantly the anodic behavior of the specimen (OCP goes from -200mV to -330mV for the uncleaned specimen). Judging from the OCP diagram, the moment when the critical crack appears becomes distinct (at about 30 minutes of testing, for the uncleaned specimen). Finally, the development of microcracks during fatigue elevates the stress levels and changes the anodic behavior locally, which leads to the appearance of pitting in these areas.



9. REFERENCES

- [1] R. Santamarta, R. Arróyave, J. Pons, A. Evirgen, I. Karaman, H.E. Karaca, R.D. Noebe, TEM study of structural and microstructural characteristics of a precipitate phase in Ni-rich Ni–Ti–Hf and Ni–Ti–Zr shape memory alloys, *Acta Materialia*, Volume 61, Issue 16, 2013, Pages 6191-6206
- [2] Parikshith K, Desai U, Monroe J, Lagoudas D, Karaman I, Bigelow G, Noebe R. Experimental investigation of simultaneous creep, plasticity and transformation of Ti50.5Pd30Ni19.5 high temperature shape memory alloy during cyclic actuation. *Materials Science and Engineering A* 2011; 530: 117-127.
- [3] Michailidis N, Stergioudi F, Maliaris G, Tsouknidas A. Influence of galvanization on the corrosion fatigue performance of high-strength steel. *Surface & Coatings Technology* 2014;259:456-464.
- [4] Bagci, C. (1993). Exact Elasticity Solutions for Stresses and Deflections in Curved Beams and Rings of Exponential and T-Sections. *Journal of Mechanical Design - J MECH DESIGN*. 115. 10.1115/1.2919198.
- [5] ASTM G38-01(2013), Standard Practice for Making and Using C-Ring Stress-Corrosion Test Specimens, ASTM International, West Conshohocken, PA, 2013, www.astm.org
- [6] O. Karakoc, C. Hayrettin, D. Canadinc, I. Karaman, Role of applied stress level on the actuation fatigue behavior of NiTiHf high temperature shape memory alloys, *Acta Materialia* (2018), doi: 10.1016/j.actamat.2018.04.021
- [7] D.C. Lagoudas, *Shape Memory Alloys Modeling and Engineering Applications*, Springer Science and Business Media, LLC, 2008
- [8] Allen Bagheria, Mohammad J. Mahtabia, Nima Shamsaei, Fatigue behavior and cyclic deformation of additive manufactured NiTi. *Journal of Materials Processing Tech.* 252 (2018) 440–453
- [9] W.D. Callister, *Materials Science and Engineering*, John Wiley & Sons, Inc., 7th Edition, 2007.
- [10] Sharma, Neeraj, Kamal K Jangra, and Tilak Raj. "Fabrication of NiTi Alloy: A Review." *Proceedings of the Institution of Mechanical Engineers, Part L: Journal of Materials: Design and Applications* 232, no. 3 (March 2018): 250–69. doi:10.1177/1464420715622494.
- [11] Meng, 祥龙 & Zheng, Yufeng & Wang, Zongyuan & Zhao, L.C. Shape memory properties of the Ti₃₆Ni₄₉Hf₁₅ high temperature shape memory alloy. *Materials Letters*. 45. (2000) 128-132. 10.1016/S0167-577X(00)00091-4.
- [12] H.X. Li, S.C. Mao, K.T. Zang, Y. Liu, Z.X. Guo, S.B. Wang, Y.F. Zhang, X.Q. Yin, An in situ TEM study of the size effect on the thermally induced martensitic transformation in nanoscale NiTi shape memory alloy, *Journal of Alloys and Compounds*, Volume 588, 2014, 337-342



10. PUBLICITY ACTIVITIES

In the following journal publications and conference presentations there was an acknowledgement of full or partial support by this grant.

10.1 Journal publications

Tsouknidas, A., Michailidis, N., Maliaris, G., Makkar, J., Th., B., Lagoudas, D., A numerical study of “functional fatigue” of closed-cell NiTi shape memory foams, (2019) *Mechanics of Materials*, 131, pp. 11-21.

A. Arvanitidis, A. Paschou, D. Kountouras, N. Michailidis, M. Mohajeri, H. Castaneda, A. Solomou, D. C. Lagoudas, Thermomechanical and corrosion fatigue of NiTiHf, *Materials Science and Engineering A*, Under preparation.

10.2 Presentations in International Conferences

N. Michailidis, F. Stergioudi, M. Pantazopoulos, K.-D. Bouzakis, G. Skordaris, P. Charalampous, T. Baxevanis, D. Lagoudas, Microstructural changes occurring in shape memory alloys after various manufacturing processes, *EUROMAT2017*, September 17-22, 2017, Thessaloniki, Greece.

A. Tsouknidas, N. Michailidis, B. Lester, T. Baxevanis, D.C. Lagoudas, G. Maliaris, Porosity-affected pseudoelasticity in NiTi shape memory foams, *52nd Annual Technical Meeting of the Society of Engineering Science (SES)*, Texas A&M University, October 26-28, 2015.

B. Lester, A. Tsouknidas, G. Maliaris, T. Baxevanis, D. Lagoudas, N. Michailidis, The effect of porosity on the pseudoelasticity of NiTi Shape Memory Foams, *4th International Conference of Engineering Against Failure (ICEAF IV)*, 24-26 June 2015, Skiathos, Greece, O16.1.

N. Michailidis, F. Stergioudi, D. Kountouras, H. Castaneda, T. Baxevanis, D. Lagoudas, Corrosion Fatigue of AA7075-T651 and NiTi-based Shape Memory Alloys, *54th Annual Meeting of the Society of Engineering Science (SES)/ASME-AMD Joint Conference*, July, 25-28 2017, Boston, MA.

M. Mohajeri, B. Haghgouyan, N. Mihailidis, H. Castaneda, D.C. Lagoudas, Corrosion of NiTi shape memory alloy: A hybrid numerical-experimental study on corrosion in detwinning regime, *EUROCORR 2018 | The Annual Congress of the European Federation of Corrosion | September 9–13, 2018 | Cracow, Poland*.

A. Arvanitidis, G. Maliaris, D.C. Lagoudas, N. Michailidis, In-situ Thermal Cycling and Fatigue of High Temperature Shape Memory Alloys, *Junior EUROMAT18*, 8-12 July, 2018, Budapest, Hungary.



N. Michailidis, A. Arvanitidis, A. Solomou, D. C. Lagoudas, Surface modification of Wire-EDMed NiTiHf after thermal actuation fatigue, CIRP General Assembly, 19-25 August 2018, Tokyo, Japan.

N. Michailidis, A. Arvanitidis, H. Castaneda, D. C. Lagoudas, In-situ Thermal Cycling, Corrosion and Fatigue of High Temperature Shape Memory Alloys (HTSMAs), CIRP STC-Surfaces, 21-23 February 2018, Paris, France.

N. Michailidis, A. Tsouknidas, G. Maliaris, T. Baxevanis, D. Lagoudas, Adjusting pseudoelasticity of NiTi shape memory foams by tailoring porosity CIRP STC-Surfaces, 17-19 February 2018, Paris, France.

N. Michailidis, A. Arvanitidis, F. Stergioudi, D. C. Lagoudas, The effect of manufacturing processes and surface treatment on the functional properties of AA7075-T6 and NiTiHf high temperature shape memory alloy, 8th EASN-CEAS International workshop on Manufacturing for growth and innovation, 4-7 September 2018, Glasgow, UK.

N. Michailidis, F. Stergioudi, A. Arvanitidis, H. Castaneda, D. C. Lagoudas, In-situ thermomechanical corrosion fatigue testing, TAMUQ Corrosion Workshop, March 1, 2018

Apostolos Arvanitidis, Alexios Paschou, Dimitrios Kountouras, Nikolaos Michailidis, Mahdi Mohajeri, Homero Castaneda, Alexandros Solomou, Dimitris C. Lagoudas, Thermomechanical and corrosion fatigue of NiTiHf: testing and modeling, EUROMAT2019, 1-5 September 2019, Stockholm, Sweden.



11. LIST OF FIGURES & DIAGRAMS

Table of figures

- Figure 1:** (a) Experimental set-up for testing corrosion-fatigue, employing C-ring samples [3], (b) sample dimensions. (page 4)
- Figure 2:** Experimental set-up developed for thermomechanical corrosion fatigue testing, employing C-ring samples. (page 5)
- Figure 3:** Software packages for guiding the experimental set-up. (page 6)
- Figure 4:** Experimental set-up for thermal fatigue tests at constant force through a pneumatic piston. (page 7)
- Figure 5:** Different control methods of the applied force. The first method in picture [A] uses a drive bolt with a positioning nut. The second method in picture [b] uses a pneumatic piston. (page 8)
- Figure 6:** Stress analysis on the c-ring. (page 9)
- Figure 7:** Setup for testing the compression behavior of the c-rings. (page 11)
- Figure 8:** Stress distribution on the c-ring surface. (page 16)
- Figure 9:** Container with two thermocouples for measure the temperature of the c-ring. (page 18)
- Figure 10:** Installation of a thermocouple to measure the temperature of the specimen. (page 19)
- Figure 11:** Scanning electron microscope (Jeol JSM – 6390LV) employed in the microstructure investigation. (page 30)
- Figure 12:** SEM image of the “as received” specimen, where the Martensitic structures can be observed in different orientations (variants). (page 30)
- Figure 13:** SEM image of the “heat-treated” specimen where the Martensitic structures can be observed in different orientations (variants). (page 31)
- Figure 14:** Sample with fatigue crack in martensitic phase after 195.000 cycles. The crack starts at the right-hand side of the specimen at the outer surface where the maximum tensile stress develops. (page 33)
- Figure 15:** Fractography (16x) of the specimen with fatigue at martensitic phase. The top image shows the end of the crack, the second image shows the middle and the bottom image the crack initiation site. (page 33)
- Figure 16:** Fractography (40x) of the fractured surface of the other c-ring segment, where the top image shows the end of the crack the second image the middle and the bottom image the crack initiation site. (page 34)
- Figure 17:** Scanning electron microscopy images of the NiTiHf sma c-ring fractured surface in the martensitic phase. (page 35)
- Figure 18:** Granular microstructure of the sample in the fractured region. (page 36)
- Figure 19:** Sample with fatigue crack in austenitic phase after 271.000 cycles. The crack starts at the left-hand side of the specimen at the outer surface where the maximum tensile stress develops. (page 37)
- Figure 20:** Fractured area of the specimen with fatigue at austenitic phase. The top image focuses on the area of the fatigue crack propagation. In the middle and bottom images, the change in morphology is observed due to brittle fracture. (page 38)



- Figure 21:** Fractured area of the specimen with fatigue at austenitic phase. Higher magnification images focusing on areas of interest. (page 39)
- Figure 22:** Scanning electron images of the NiTiHf c-ring fractured surface in the austenite phase. (page 40)
- Figure 23:** Microstructure of the material on the fractured surface. (page 41)
- Figure 24:** Corrosion – fatigue experiment in 3.5 wt % NaCl aqueous solution. (page 42)
- Figure 25:** Fractured surface of the specimen of the 1st combined corrosion and fatigue experiment. Right image: beginning of the crack. Left image: end of the crack. (page 44)
- Figure 26:** Fracture surface of the specimen of the 1st combined corrosion and fatigue experiment. (page 45)
- Figure 27:** Fractured area of the specimen at higher magnification. (page 46)
- Figure 28:** Change of the sample color after heat treatment (right) attributed to surface oxidation. (page 46)
- Figure 29:** Electrochemical cleaning of NiTiHf specimen. (page 47)
- Figure 30:** The specimen parent alloy which was revealed from electrochemical cleaning. (page 47)
- Figure 31:** Experimental setup for the investigation of the corrosion-fatigue. (page 50)
- Figure 32:** Electrical connection of the specimen and its holder in the fatigue device. (page 51)
- Figure 33:** Outer surface of the cleaned specimen before and after the corrosion-fatigue experiment. (page 56)
- Figure 34:** Fractured surface of the electrochemically cleaned specimen after the combined corrosion-fatigue and potentiodynamic polarization test. (page 57)
- Figure 35:** Crack start area where intense pitting corrosion can be observed in two directions. (page 58)
- Figure 36:** Surface of brittle fracture of electrochemically cleaned specimen, where pitting corrosion is evident. (page 58)
- Figure 37:** Area of extended surface corrosion of the electrochemically cleaned specimen. (page 59)
- Figure 38:** Fracture surface of electrochemically cleaned specimen after fatigue. (page 59)
- Figure 39:** Starting point of the crack in the electrochemically cleaned specimen during combined corrosion-fatigue. (page 60)
- Figure 40:** More detailed images of the crack starting point and propagation. (page 61)
- Figure 41:** Outer surface of the uncleaned specimen before and after the combined corrosion and fatigue experiment. (page 62)
- Figure 42:** Fractured surface of the uncleaned specimen after the end of the potentiodynamic polarization. (page 63)
- Figure 43:** Fractures surface of the uncleaned specimen that which is not subjected to potentiodynamic polarization. (page 64)

**Table of diagrams**

- Diagram 1:** Load - displacement curves in compression of sma c-ring at 150 N. (page 12)
- Diagram 2:** Load - displacement curves in compression of sma c-ring at 300 N. (page 12)
- Diagram 3:** Load - displacement curves in compression of sma c-ring at 600 N. (page 13)
- Diagram 4:** Stress - displacement curves of first and tenth cycle in various stresses at the martensitic phase in twinned and detwinned specimen. (page 14)
- Diagram 5:** Modulus of elasticity - displacement of first and tenth cycle in various stresses at the martensitic phase in twinned and detwinned specimen. (page 14)
- Diagram 6:** Stress - displacement curve for NiTiHf c-ring after 40 thermal cycles compared with that of no thermal cycling. (page 17)
- Diagram 7:** Modulus of elasticity - displacement curve for NiTiHf c-ring after 40 thermal cycles compared with that of no thermal cycling. (page 17)
- Diagram 8:** Temperature difference between the c-ring and the air during heating and cooling. (page 20)
- Diagram 9:** Temperatures of austenitic transformation start (A_s) during heating, at various force values. (page 21)
- Diagram 10:** Temperatures of martensitic transformation start (M_s) during cooling, at various load levels. (page 22)
- Diagram 11:** Temperatures of martensitic transformation finish (M_f) during cooling, at various load levels. (page 23)
- Diagram 12:** Temperatures of austenitic transformation finish (A_f) during heating, at various load levels. (page 24)
- Diagram 13:** Force vs. transformation temperature diagram. (page 25)
- Diagram 14:** Stress vs. transformation temperature diagram. (page 26)
- Diagram 15:** Phase transformation values from isobaric tension tests at different stress values and temperatures. The calculation equations are exported using the trendlines. (page 27)
- Diagram 16:** DSC of the "heat-treated" material. (page 28)
- Diagram 17:** DSC of the "as received" material, (page 29)
- Diagram 18:** Fatigue results of NiTiHf in martensitic and austenitic phase, as well as in various corrosion conditions. Loading frequency: 40Hz, loading amplitude: 0 N - 600N ($R=0$). (page 32)
- Diagram 19:** Observation of individual loading cycles of combined corrosion and fatigue experiment. (page 43)
- Diagram 20:** Potentiodynamic curve in the unloaded state for the cleaned specimen. (page 48)
- Diagram 21:** Detection of open circuit potential and combined corrosion and fatigue test of the cleaned specimen. (page 49)
- Diagram 22:** Waveform of loading cycles for the cleaned specimen until fracture. (page 52)
- Diagram 23:** Potentiodynamic curve in the unloaded state for the uncleaned specimen. (page 53)
- Diagram 24:** Detection of open circuit potential and combined corrosion and fatigue test of uncleaned specimen. (page 53)
- Diagram 25:** Electrochemical impedance spectroscopy for the uncleaned specimen in unload state during fatigue experiment. (page 54)
- Diagram 26:** Impedance comparison of the specimens after fracture. (page 55)